Mémoire présenté pour obtenir

l'Habilitation à Diriger des Recherches

de l'Université Pierre et Marie Curie (Paris VI)

par

Sébastien MICHELIN

Maître de conférences,
LadHyX – Ecole polytechnique

Fluid-solid interactions:

Locomotion, instabilities and energy transfers.

soutenu le 7 Juin 2013 devant le jury composé de

Matthias Heil	Examinateur	Professor, University of Manchester
Christophe Josserand	Examinateur	Directeur de Recherche, Institut Jean Le Rond d'Alembert
Patrice Le Gal	Rapporteur	Directeur de Recherche, Institut de Recherche sur les Phénomènes Hors Equilibre
Jacques Magnaudet	Rapporteur	Directeur de Recherche, Institut de Mécanique des Fluides de Toulouse
Timothy J. Pedley	Rapporteur	Professor, University of Cambridge

Contents

Introduction

This document proposes an overview and summary of my research since my PhD defense in 2009 and my arrival at LadHyX as an Assistant Professor in Mechanics in 2010.

My PhD work was dedicated to a reduced-order model for fluid-solid interactions in high-Re flows based on a particular vortex shedding representation, and to its applications to a large variety of problems ranging from the dynamics of falling cards to flapping flexible wings and flags. This was my first opportunity to consider problems of bio-inspired locomotion, studying for example the effect of flexibility on propulsive performance. This experience triggered my interest for this type of fluid-solid interaction problems and motivated me to focus on locomotion at both ends of the Re spectrum, significantly developing over the last four years an important research activity on locomotion in low-Re flows. In parallel, and continuing with my initial interest for high-Re fluid-solid instabilities, I developed a research activity at LadHyX on the applications of such instabilities to energy harvesting: such instabilities indeed enable the spontaneous and self-sustained motion of a solid under the effect of a steady flow. Studying their potential applications to energy harvesting (i.e. the production of electricity from this self-sustained solid motion) therefore represents a natural evolution of my activity from my previous research topics.

The present document therefore articulates around these two main axes: biolocomotion in low-Re flows and fluid-solid instabilities in high-Re flows. This diversity in the problems that I consider in my research results from and illustrates the progressive evolution of my scientific interests over the last five years. It also emphasizes the main scientific question that is at the core of my research, namely understanding how deformable solids move and interact with a surrounding flow and may passively or actively take advantage of it. The different topics covered in this manuscript show how diverse this interaction may be, depending on the flow regime (small-scale viscous flows vs. large scale inertial flows) and on the applications considered (active locomotion vs. passive energy harvesting).

In both cases, the interaction of the solid with the surrounding fluid leads to a local fluid-solid energy transfer through the work of the fluid forces on the solid, but the two types of problems considered here differ fundamentally on the direction of this energy transfer. In the locomotion problem, energy is transferred and lost to the fluid by the swimming organism, through the swimmer's deformation to which the fluid is resisting or reacting. In a fluid-solid instability problem, the net energy transfer is reversed: a fraction of the fluid kinetic energy is transferred to the solid body and leads to its spontaneous motion.

A brief outline of the main questions addressed in this manuscript is presented below. The last section of each chapter will be dedicated to some open questions that are either the focus of my ongoing research or that I would like to develop in the future.

Chapter 1 focuses on biolocomotion of micro-organisms in viscous flows and is organized around two main objectives: (i) characterizing the relationship between the energy cost of a particular swimming stroke and its performance either in terms of swimming or feeding for the cell, and (ii) studying and modeling of a particular type of micro-swimmers, namely reactive colloids, which use surface reactions to create a net swimming motion. The work presented in this chapter results from collaborations with Eric Lauga (UCSD)

and more recently with Denis Bartolo (ESPCI/ENS Lyon).

Chapter 2 presents a summary of my recent research on fluid-solid instabilities in inertial flows and their application to energy harvesting systems. It is dedicated to the following three main objectives: (i) understanding the two-way coupling between the fluid-solid system and the energy harvesting/dissipating device, (ii) modeling the coupled non-linear dynamics and (iii) assessing how much energy can be harvested using such systems. Part of the work presented in this chapter is the result of a collaboration with Emmanuel de Langre (LadHyX) and corresponds to the PhD work of Clément Grouthier (2010–2013) and the postdoctoral work of Kiran Singh (2010–2012). The last part of this chapter, which focuses on the piezoelectric flag, is an ongoing collaboration with Olivier Doaré (ENSTA ParisTech), and is also currently the focus of the PhD work of Yifan Xia at LadHyX.

The common approach to both types of problems is a combination of theoretical analysis and numerical simulations to study the nonlinear coupled dynamics of the fluid-solid system. Rather than using direct numerical simulations of the fluid flow for general systems, an effort is systematically made to simplify the system's geometry (e.g. a spherical model organism, a purely two-dimensional motion for the flapping plate,...) in order to simplify the fluid-solid dynamics and to focus on the main physical processes at stake in this problem (e.g. the impact of swimming on feeding, the role of the output circuit in a harvesting system). Such simplifications may originate, for example, from the symmetries of the geometry considered or from the small aspect ratio of the structure.

Both problems (locomotion and energy harvesting) are concerned with energy transfers between the fluid and solid systems, whether as a cost (the amount of work that must be done by an organism to swim) or as a product (the amount of energy that can be harvested using an instability). In each case, I will provide some insight on how to optimize the system or, equivalently, maximize its efficiency: in the locomotion problem, it will correspond to maximizing the biological performance (displacement or feeding) for a fixed energy cost; in the energy harvesting problem, it will correspond to maximizing the fraction of the kinetic energy flux in the oncoming flow that can be actually transferred to an output electrical loop.

Chapter 1

Self-propulsion in low-Re flows

1.1 Introduction

Although unnoticed to our eyes, micro-organisms are omnipresent in the world we live in, performing a large variety of biological functions (e.g. bacteria and spermatozoa in our own bodies, small protozoa and algae in the ocean). For many such organisms, locomotion is a critical function, whether to move toward regions with different chemical concentrations (e.g. chemotaxis of *E. Coli*), to escape aggressions (e.g. *Paramecium* escaping larger predators) or to enable reproduction (e.g. spermatozoa swimming toward the ovum). Like a swimmer in a pool performs his stroke and deforms his body to put the fluid around him in motion and create a forward displacement, such organisms rely on shape deformations (e.g. flagella or cilia beating) to produce their locomotion.

Although similar in appearance, both problems concerning swimmers are strikingly different because of the scales at which the motion takes place. In the world of Olympic swimmers whose typical size is of the order of 2 m with velocities of the order of a few $\mathrm{m.s}^{-1}$, the solid and fluid inertia play a major role. Viscous effects are limited to the immediate vicinity of a solid boundary in so-called boundary layers, but may play an essential role in generating vorticity. In the realm of bacteria and larger micro-organisms whose sizes range from 1 to 100 μm and velocities from 10 to 100 $\mu\mathrm{m.s}^{-1}$, inertia's role is only marginal, and flow forces are completely dominated by the effect of viscosity. This contrast is quantified by the Reynolds number, defined later on as $\mathrm{Re} = \rho_f U a/\eta_f$ with U and a the characteristic velocity and size of the organism and ρ_f and η_f the density and shear viscosity of the fluid. Re is a measure of the relative effect of inertia and viscosity on the flow, and while it can be as high as 10^5 for a human swimmer, its value is only 10^{-6}–10^{-3} for typical swimming micro-organisms.

Understanding how such organisms move in their environment is interesting from a fundamental biophysical point of view, but also because of the critical role these organisms have in their ecosystem, from the impact of phytoplankton on ocean mixing to the role of sperm cell mutations in reproductive disorders of larger organisms. From an engineering point of view, this swimming problem at the micro-scale is particularly interesting in biomimetic applications: understanding how to create devices that are able to swim at the micron or millimeter scale can be essential for future biomedical applications such as targeted drug delivery.

As for the Olympic swimmer, moving in a fluid has a cost for the swimming bacteria or micro-robots. While obviously not the only factor influencing the natural evolution of micro-organism species, energy efficiency (that is, how much an organism can do with a fixed amount of energy) can clearly give an organism a competitive advantage, and energy efficiency is a critical element in any man-made device in order to minimize either the fuel consumption or the applied forcing. Understanding the energetic implications of biolocomotion at these scales is therefore critical for such applications.

Motivated by such considerations, the focus of my research has been on a better understanding of funda-

mental techniques used by natural micro-organisms to move in their environment, and in particular on the relative advantages of different swimming strokes from an energetic point of view. A significant part of the research presented below is therefore dedicated to determining the optimal swimming strokes for different biological functions: displacement or nutrient absorption.

This chapter is organized as follows. Section 1.2 presents a brief overview of the swimming problem at low Re and of different classical approaches that can be used to solve it. In sections 1.3 and 1.4, a particular type of micro-organism is considered (ciliates) for which optimal strokes are determined either to maximize locomotion (Section 1.3) or feeding (Section 1.4). Section 1.5 offers some insight on a particular type of artificial swimmer, typically a reactive colloid particle, and presents some of the most recent results I have obtained on that topic. Finally, some conclusions and perspectives are presented in Section 1.6.

1.2 Swimming in viscous flows

1.2.1 A geometric problem

The locomotion problem can be formalized mathematically as determining the net motion (translation $\mathbf{U}$ and rotation $\mathbf{\Omega}$) of a swimming or flying organism Ω as a result of a prescribed deformation of its surface $\mathcal{S}$. This stroke is characterized, in the reference frame of the center of mass of the organism, by a deformation velocity $\tilde{\mathbf{u}}$ defined on $\mathcal{S}$. To solve this swimming problem, i.e. to determine $(\mathbf{U}, \mathbf{\Omega})$ as a function of $\tilde{\mathbf{u}}$, the response of the fluid to the solid motion must be determined either through the local modeling of the flow forces (e.g. slender body theory in both viscous and inertial flows) or by a direct computation of the flow generated around the organism.

One should point out that this formulation is only one possible approximation: in many instances, the organism's muscles or structure will prescribe surface stresses rather than displacements (Kanevsky *et al.*, 2010). In some other cases, as for an insect's wing or a bacterium's flagella, a forcing is prescribed by the organism only on part of its body (e.g. the wing tip or the flagellum's base), with the rest of the structure deforming passively.

The particular swimming problem considered here can then be formalized as follows assuming an incompressible Newtonian fluid.

(a) In the fluid, the velocity and pressure fields satisfy the Navier-Stokes equations:

$$\rho_f \frac{\mathrm{D}\mathbf{u}}{\mathrm{D}t} = -\nabla p + \eta_f \nabla^2 \mathbf{u}, \quad \nabla \cdot \mathbf{u} = 0, \tag{1.1}$$

where ρ_f and η_f are respectively the density and dynamic viscosity of the fluid.

(b) The conservation of linear and angular momentum for the solid body are written as

$$M\frac{\mathrm{d}\mathbf{U}}{\mathrm{d}t} = \int_{\mathcal{S}} \boldsymbol{\sigma}\cdot\mathbf{n}\,\mathrm{d}S + \mathbf{F}_{\text{ext}}, \qquad \frac{\mathrm{d}}{\mathrm{d}t}(\mathbf{J}\cdot\mathbf{\Omega}) = \int_{\mathcal{S}} (\mathbf{x}-\mathbf{x}_G)\times(\boldsymbol{\sigma}\cdot\mathbf{n})\,\mathrm{d}S + \mathbf{T}_{\text{ext}}, \tag{1.2}$$

where M and $\mathbf{J}$ are respectively the mass and moment of inertia tensor of the solid body (which may depend on time due to the body deformation), $\boldsymbol{\sigma} = -p\mathbf{1} + \eta_f(\nabla\mathbf{u} + \nabla\mathbf{u}^T)$ is the fluid stress tensor, and $\mathbf{n}$ is the normal vector pointing into the fluid domain. $\mathbf{F}_{\text{ext}}$ and $\mathbf{T}_{\text{ext}}$ correspond to the external body force and torque (e.g. gravity effects if the organism is not neutrally buoyant and homogeneous).

(c) The kinematic boundary condition imposes the adherence of the fluid to the solid boundary:

$$\mathbf{u} = \mathbf{U} + \mathbf{\Omega}\times(\mathbf{x}-\mathbf{x}_G) + \tilde{\mathbf{u}} = \mathbf{u}_S \quad \text{for } \mathbf{x}\in\mathcal{S}. \tag{1.3}$$

(d) Finally, at infinity the fluid is at rest

$$\mathbf{u} \to 0 \quad \text{for } \mathbf{x} \to \infty. \tag{1.4}$$

Equations (1.1)–(1.4) form a complete set of equations for the variables $(\mathbf{u}, p, \mathbf{U}, \boldsymbol{\Omega})$.

The motion of the fluid originates from the motion of the solid boundary: the characteristic velocity scale U is therefore determined by the stroke $\tilde{\mathbf{u}}$. In incompressible flows, the pressure acts as a Lagrange multiplier to ensure the fluid's incompressibility. Its typical scale is therefore that of the dominant term in Eq. (1.1). Choosing a, the typical size of the organism as the reference length scale, and a viscous scaling for the pressure, the Navier-Stokes equations Eq. (1.1) then take the following non-dimensional form

$$\mathrm{Re}\frac{\mathrm{D}\mathbf{u}}{\mathrm{D}t} = -\nabla p + \nabla^2\mathbf{u}, \quad \nabla\cdot\mathbf{u} = 0, \tag{1.5}$$

with the Reynolds number $\mathrm{Re} = \rho_f U a/\eta_f$ characterizing the relative importance of inertia and viscous effects in the flow. Ranging from $\mathrm{Re} \approx 10^{-5}$ for bacteria in water to $\mathrm{Re} \approx 10^5$ for large birds, the Reynolds number characterizes the locomotion regime: while fluid inertia and vortex shedding are dominant in the fluid forces for flying insects and swimming fish, the locomotion of micro-organisms is controlled by viscous forces and fluid inertia plays essentially no role. The Reynolds number also characterizes the distance d over which the organism would coast, should it stop performing its stroke (Lauga & Powers, 2009): when inertia dominates, $d/a \sim \rho_s/\rho_f = O(1)$ but in viscous flows, $d/a \sim \mathrm{Re}(\rho_s/\rho_f) \ll 1$: the organism stops moving as soon as it stops deforming. From a mechanical point of view, in Eq. (1.2), the left hand side (solid inertia) is negligible in comparison with the fluid forces so that these equations simplify into the no-force and no-torque condition (in the case considered here where $\mathbf{F}_{\text{ext}} = \mathbf{T}_{\text{ext}} = 0$):

$$\int_{\mathcal{S}} \boldsymbol{\sigma}\cdot\mathbf{n}\,\mathrm{d}S = 0, \qquad \int_{\mathcal{S}} (\mathbf{x}-\mathbf{x}_G)\times(\boldsymbol{\sigma}\cdot\mathbf{n})\,\mathrm{d}S = 0. \tag{1.6}$$

This illustrates the absence of history effect in the swimming problem for $\mathrm{Re} \ll 1$: the swimming motion $(\mathbf{U}, \boldsymbol{\Omega})$ at time t only depends on the deformation velocity $\tilde{\mathbf{u}}$ at this same instant and not on the deformation history. Also this dependence is linear, so that superposition principles may be used. Time now only comes into play through the modification of the problem's geometry if the body Ω is deformed. The swimming problem becomes a geometric problem: how to find the relationship between the surface velocity (or shape changes) and the swimming motion at each instant *independently*. This is illustrated by the instantaneous formal solution of this problem obtained by applying the reciprocal theorem to Stokes equations: for a swimmer of arbitrary shape $\mathcal{S}$ (which may be time-dependent), if $\hat{\boldsymbol{\sigma}}$ denotes the stress-field in the fluid generated by an arbitrary solid body motion $(\hat{\mathbf{U}}, \hat{\boldsymbol{\Omega}})$ of $\mathcal{S}$ and resulting in a force and torque $(\hat{\mathbf{F}}, \hat{\mathbf{L}})$ applied by the fluid on the rigid body, the translation and rotation velocities $\mathbf{U}$ and $\boldsymbol{\Omega}$ resulting from the deformation velocity $\tilde{\mathbf{u}}$ of $\mathcal{S}$ for a force-free and torque-free swimmer satisfies (Stone & Samuel, 1996):

$$\hat{\mathbf{F}}\cdot\mathbf{U} + \hat{\mathbf{L}}\cdot\boldsymbol{\Omega} = -\int_{\mathcal{S}} \mathbf{n}\cdot\hat{\boldsymbol{\sigma}}\cdot\tilde{\mathbf{u}}\,\mathrm{d}S. \tag{1.7}$$

The previous equation states that, at each instant independently, the swimming motion is obtained explicitly and linearly from $\tilde{\mathbf{u}}$ if the solution to the steady solid body motion problem is known. Note that for a swimmer with a time-varying shape, the solid body problem needs to be solved for each successive shape.

A direct consequence of the absence of history effects is that the trajectory of a swimming body in viscous flows only depends on the sequence of the surface displacements, not on how fast this sequence is performed. Also, if performing a particular sequence or stroke brings the organism from point A to point B, performing the opposite stroke (that is, the same sequence in reversed order) will bring the organism back to point A, leading to no net swimming motion. This is the essence of the well-known *scallop theorem* (Purcell, 1977)

and a major difference between the swimming problem in viscous and inertial flows: an organism performing a time-reciprocal stroke can not swim in Stokes flow.

To overcome this difficulty, micro-organisms and artificial micro-robots must use non reciprocal strokes and the main encountered strategy is based on wave propagation. Bacteria and sperm cells deform their flagella in the form of planar or helical wave patterns. Ciliates (e.g. *Paramecium*) break symmetry at two different levels: each individual cilium, a slender flapping appendage attached to the cell's surface, has an asymmetric beating pattern with distinct effective and recovery strokes; at the organism's level, coordination of neighboring cilia leads to the formation of so-called metachronal waves (Brennen & Winnet, 1977).

It is worth noting that this absence of history effects in the swimming problem at $\mathrm{Re} = 0$ is also observed in the opposite limit ($\mathrm{Re} = \infty$) for inviscid potential flows: to swim in that limit also requires performing non-reciprocal strokes, and a swimmer that stops deforming at $t = t_0$, stops instantaneously (Kanso *et al.*, 2005; Kanso & Marsden, 2005). This similarity is rather counter-intuitive given the fundamental difference of the swimming problem in inertial and viscous flows, but it stems from the similar mathematical nature of both problems: in both cases, the velocity field $\mathbf{u}$ can be derived from a solution of Laplace's equation (the velocity potential ϕ in potential flows or the pressure p in Stokes flows), forced instantaneously at the boundaries.

1.2.2 Fundamental singularities in Stokes flow

In the limit of no inertia, the Navier–Stokes equations simplify into Stokes' equations

$$\nabla^2 \mathbf{u} = \nabla p, \quad \nabla \cdot \mathbf{u} = 0, \tag{1.8}$$

and the pressure p satisfies Laplace's equation $\nabla^2 p = 0$. The Stokes flow problem is linear and can be solved using the superposition principle of fundamental solutions. Using the single-layer and double-layer potentials formalism, the Stokes flow problem outside the swimmer can be solved explicitly (Pozrikidis, 1997)

$$\mathbf{u}(\mathbf{x}) = -\frac{1}{8\pi\eta_f} \int_{\mathcal{S}} \mathbf{G}(\mathbf{x},\mathbf{s}) \cdot \mathbf{f}(\mathbf{s}) \, \mathrm{d}S(\mathbf{s}) - \frac{1}{8\pi} \int_{\mathcal{S}} [\mathbf{T}(\mathbf{x},\mathbf{s}) \cdot \tilde{\mathbf{u}}(\mathbf{s})] \cdot \mathbf{n}(\mathbf{s}) \, \mathrm{d}S(\mathbf{s}) \tag{1.9}$$

where $\mathbf{G}(\mathbf{x},\mathbf{s})$ is the Green's function corresponding to the flow field generated at $\mathbf{x} \in \Omega$ by a point force located at $\mathbf{s} \in \mathcal{S}$ and $\mathbf{T}(\mathbf{x},\mathbf{s})$ is the corresponding stress tensor. $\mathbf{f}$ is the imposed (but unknown) stress on the swimmer's boundary. The exact expressions for $\mathbf{G}$ and $\mathbf{T}$ depend on the geometry of the fluid domain and are respectively equal to $(r^2\mathbf{1} + \mathbf{rr})/r^3$ and $-6\mathbf{rrr}/r^5$ with $\mathbf{r} = \mathbf{x} - \mathbf{s}$ for the free flow case. This development is at the heart of the boundary integral methods for Stokes flow: from $\tilde{\mathbf{u}}$, and the analog to Eq. (1.9) for $\mathbf{x} \in \mathcal{S}$, the traction $\mathbf{f}$ at the boundary can be determined. From $\tilde{\mathbf{u}}$ and $\mathbf{f}$, the velocity at any point in Ω can be computed using Eq. (1.9).

Equation (1.9) illustrates that the general solution of the Stokes flow problem can be formulated as a superposition of fundamental singularities. The stokeslet $\mathbf{G}(\mathbf{x},\mathbf{x}_0)$ (flow field created by a point force), and its derivatives with respect to $\mathbf{x}_0$, represent fundamental singular solutions that can be superimposed to obtain the solution of the Stokes problem (Batchelor, 1970; Blake & Chwang, 1974).

For example, superimposing a stokeslet and a source dipole of carefully-chosen intensities describes the flow field around a sphere and leads to the classical Stokes drag formula $\mathbf{F} = -6\pi\eta_f a\mathbf{U}$. Using a continuous distribution of such singularities along a slender but finite rod, leads to the following relationship between the velocity $\mathbf{U}$ of the rod and the force $\mathbf{F}$ applied to it

$$\mathbf{F} = -[(\zeta_\parallel \mathbf{tt} + \zeta_\perp(\mathbf{1} - \mathbf{tt})] \cdot \mathbf{U}. \tag{1.10}$$

where $\mathbf{t}$ is the local tangential vector to the centerline of the structure and $\zeta_\parallel$ and $\zeta_\perp$ are the local drag coefficient in the tangential and normal directions, respectively. $\zeta_\parallel$ and $\zeta_\perp$ are generally not equal, and in the limit of a long, slender, and smooth rod $\zeta_\perp \approx 2\zeta_\parallel$.

These fundamental singularities also play an essential role in the description of the far-field flow associated with the presence of an active or passive solid boundary: the stokeslet, whose intensity is equal to the net force applied on the fluid by the solid boundary, is generally dominant in the far-field with a slow $(1/r)$ decay of the velocity field. Associating two Stokeslets of opposite intensities corresponds to a force dipole that can be decomposed into its symmetric (the stresslet) and anti-symmetric parts (a rotlet). The latter is a measure of the torque applied on the fluid by the particle, and for both cases, the velocity field decays as $1/r^2$. Higher-order singularities with faster spatial decays are then obtained through further differentiation and pairing of fundamental singularities (Batchelor, 1970; Blake & Chwang, 1974; Chwang & Wu, 1975). Although most convenient in the case of a particle in an unbounded fluid, fundamental singularities may also be used together with the method of images to model the swimming motion near a boundary (Blake & Chwang, 1974; Crowdy *et al.*, 2011; Spagnolie & Lauga, 2012) or for various shape swimmers (Chwang & Wu, 1975).

The superposition of fundamental singularities is at the core of two fundamental simplified theories to compute the flow forces on slender flexible appendages, which are omnipresent in the realm of micro-swimmers in the form of flagella and cilia. When the radius of the flagellum is much smaller than its typical wavelength, *Resistive Force Theory* identifies locally the filament to a fraction of a long straight rod and Eq. (1.10) is used locally to relate the force to the local flagellum velocity. *Slender body theory*, introduced by Hancock (1953) and Gray & Hancock (1955), builds on this approach by including far-field hydrodynamic interactions between distant parts of a curved flagellum.

1.2.3 An application to hydrodynamic interactions

For a torque-free and force-free swimmer (1.6), there is no Stokeslet nor rotlet and the far-field velocity is dominated by the stresslet contribution which emphasizes its importance in accounting for hydrodynamic interactions between multiple swimmers. Indeed, when considering two force-free and torque-free swimmers, the stresslet associated with the first swimmer will be the first flow perturbation that will be seen by the second swimmer and that will influence its trajectory. In suspensions, the stresslet is associated with the modification of the bulk stress by the presence of the swimmers (Batchelor, 1970). The pressure and velocity field associated with a stresslet $\mathbf{\Sigma}$ are given by

$$\mathbf{u} = -\frac{3}{8\pi\eta_f}\frac{(\mathbf{r}\cdot\mathbf{\Sigma}\cdot\mathbf{r})\mathbf{r}}{r^5}, \qquad p = -\frac{3}{4\pi}\frac{(\mathbf{r}\cdot\mathbf{\Sigma}\cdot\mathbf{r})}{r^5} \tag{1.11}$$

with $\mathbf{\Sigma}$, the stresslet intensity, a symmetric order-2 tensor and $\mathrm{tr}(\mathbf{\Sigma}) = 0$ when the volume of the solid particle does not change in time. Defining $\overline{\Sigma}$ as the eigenvalue with largest magnitude (positive or negative), two types of swimmers can be considered: (a) *pushers* when $\overline{\Sigma} < 0$ and (b) *pullers* when $\overline{\Sigma} > 0$. Pushers (resp. pullers) correspond to swimmers with the drag-generating center (e.g. head) located in front of (resp. behind) the thrust-generating element (e.g. flagellum). A typical example of pusher is a sperm cell while *Chlamydomonas*, a cellular organism actuating two flagella located in the front in a breast-stroke fashion, is a classical example of puller swimmer.

This is the essence of the work presented in Michelin & Lauga (2010*b*) on the far-field interaction of two particular swimmers that have circular trajectories when they are isolated. Using the leading-order hydrodynamical coupling between these two swimmers, we showed that hydrodynamic interactions can have a major role in the long-time collective dynamics of the two organisms. In particular, we showed that any relative equilibrium of the averaged swimming trajectories is unstable, and that only two long-time behaviors are possible: (i) an attraction of the swimmers (leading to a more complex short-range hydrodynamic coupling) or (ii) a repulsion leading to the two swimmers drifting away from each other (Figure 1.1, Michelin & Lauga, 2010*b*). The distinction between the different regimes can be identified in terms of the nature of the swimmers (pusher vs. puller) and their initial relative orientation (Figure 1.1).

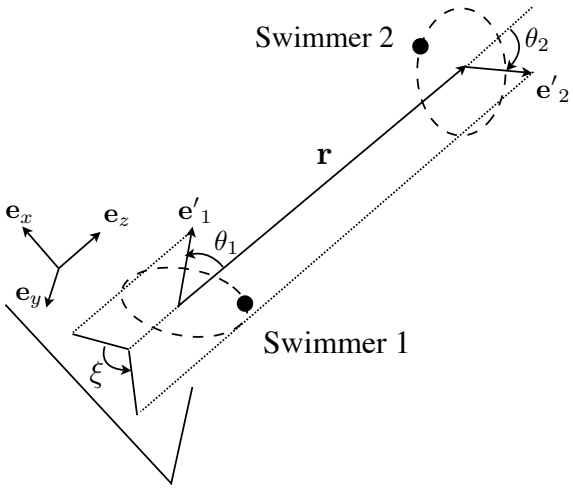

(a) Hydrodynamic interaction of two swimmers

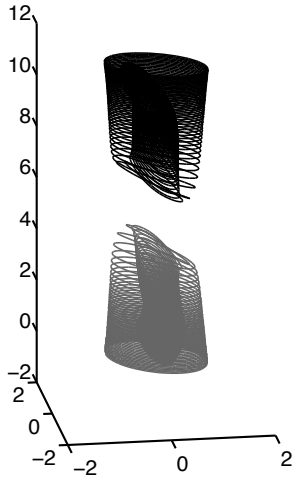

(b) Trajectories

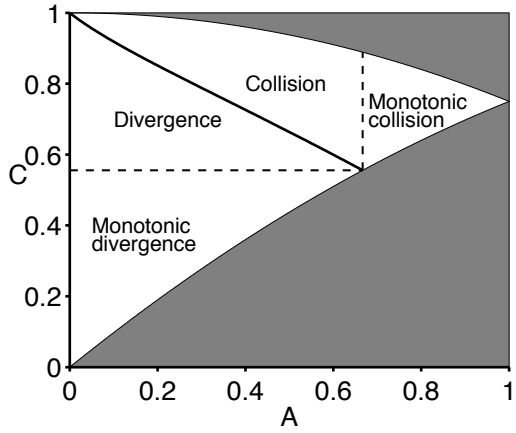

(c) Pushers ($\overline{\Sigma} < 0$)

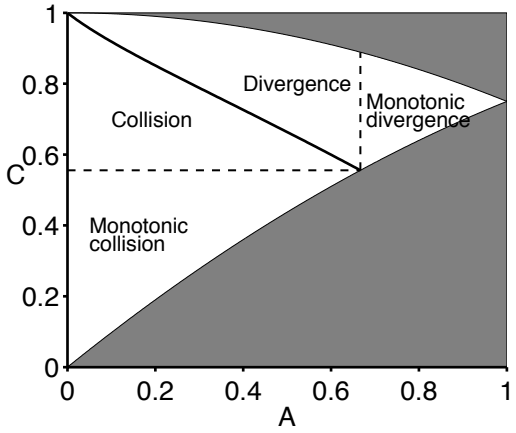

(d) Pullers ($\overline{\Sigma} > 0$)

Figure 1.1: (a) Long-time hydrodynamic interaction of two swimmers with intrinsic circular trajectories. (b) Example of trajectories of the interacting swimmers: an initial attraction is followed by a rapid switch in the plane of their trajectories to lead to a repulsive regime. (c,d) Bifurcation diagram of the long-time dynamics for pushers (c) and pullers (d). The coefficients A and C are conserved geometric quantities depending only on the relative orientation of the trajectories (as characterized by θ_1, θ_2 and ξ), and not on the initial relative distance (see Michelin & Lauga, 2010*b*, for more details).

1.2.4 A canonical micro-swimmer model: the squirmer

Although the Stokes equations (1.8) are linear, solving the swimming problem can quickly become intractable by hand for complex geometries. Beyond the direct numerical simulations of Stokes flow around a realistic geometry, two main strategies are generally followed: (i) using a local approximation for the flow forces or (ii) choosing simple enough geometries to simplify the Stokes flow problem.

A classical example of the former approach is illustrated by the resistive force and slender body theories, which were briefly presented above. One of the best examples of the latter is the so-called *squirmer*, a spherical model organism prescribing its surface velocity. The existence of an explicit solution to the Stokes flow problem around a sphere makes this model particularly attractive to study different effects and properties of low-Re locomotion for a simple geometry. In the remainder of this chapter, this model will be extensively used in the particular case of a stroke corresponding to purely tangential and axisymmetric displacements of the organism's boundary so that its shape remains spherical at all times (Lighthill, 1952; Blake, 1971). For a force-free and torque-free squirmer, the entire flow field, in the co-moving frame, can be obtained analytically by super imposing so-called squirming modes. In the streamfunction formulation,

$$\psi(r,\mu,t) = \sum_{n=1}^{\infty} \alpha_n(t)(1-\mu^2)L_n'(\mu)\Psi_n(r) \tag{1.12}$$

with

$$\Psi_1(r) = \frac{1}{2}\left(\frac{1}{r} - r^2\right) \qquad \text{and} \quad \Psi_n(r) = \frac{2n+1}{2n(n+1)}\left(\frac{1}{r^n} - \frac{1}{r^{n-2}}\right) \quad \text{for } n \geq 2, \tag{1.13}$$

where the squirming mode intensity $\alpha_n(t)$ are obtained by projection of the surface tangential velocity

$$\alpha_n(t) = \frac{1}{2}\int_{-1}^{1} \sqrt{1-\mu^2}u_\theta(r=1,\mu)L_n'(\mu)\mathrm{d}\mu \tag{1.14}$$

Here, $\mu = \cos\theta$ refers to spherical polar coordinates in a reference frame centered on the swimmer and $L_n(\mu)$ is the n-th Legendre polynomial. The velocity field is obtained from ψ as

$$\mathbf{u} = -\frac{1}{r^2}\frac{\partial\psi}{\partial\mu}\mathbf{e}_r - \frac{1}{r\sqrt{1-\mu^2}}\frac{\partial\psi}{\partial r}\mathbf{e}_\theta. \tag{1.15}$$

The squirming modes correspond to increasing orders of azimuthal dependence and, apart from the first mode, increasing orders of far-field decay of the velocity field (Figure 1.2). The first mode is the only one contributing to the swimming velocity of the organism so that $U(t) = \alpha_1(t)$, and it corresponds to a slip velocity oriented from front to back on the entire sphere: it is therefore often referred to as the swimming or "treadmill" mode. Note that this mode also corresponds to purely potential flow ($\boldsymbol{\omega} = 0$), even though we consider here viscous inertia-less flows. The second squirming mode is dominant in the far-field (in the labframe) and corresponds to the stresslet with a spatial decay of the velocity field in $1/r^2$. As mentioned previously, this quantity corresponds to the modification of the bulk stress by the swimming particle (Batchelor, 1970) and also characterizes the nature of the swimmer: swimmers with $\alpha_2 > 0$ are of puller type, while $\alpha_2 < 0$ corresponds to pushers.

Determining the intensity (possibly unsteady) of the squirming modes $\alpha_n(t)$ is therefore an essential step as it provides important information about the stroke $\tilde{\mathbf{u}}$ considered (e.g. swimming velocity, intensity and sign of the stresslet...). Later on, we will discuss the cost of the swimming motion. From a hydrodynamic point of view, it can be defined as the work done by the squirmer on the fluid:

$$\mathscr{P}(t) = -\int_{\mathcal{S}} \tilde{\mathbf{u}}\cdot(\boldsymbol{\sigma}\cdot\mathbf{n})\mathrm{d}S = \int_{\Omega}(\boldsymbol{\sigma}:\mathbf{d})\mathrm{d}V \tag{1.16}$$

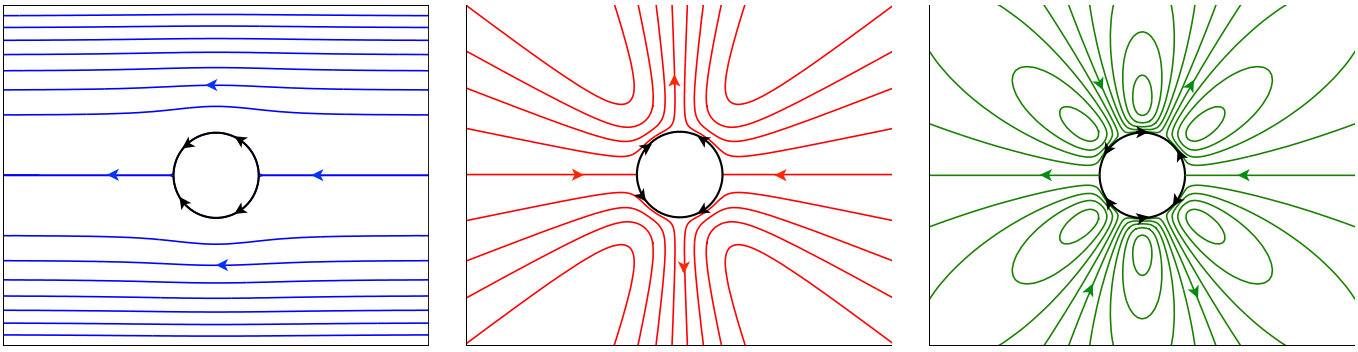

Figure 1.2: Streamlines of the first three squirming modes for unit intensity and a force-free and torque-free swimming particle. (Left) $n = 1$, "treadmill" or swimming mode, (Center) $n = 2$, Stresslet mode (note that $\alpha_2 = 1$ corresponds to a puller-type squirmer) and (Right) $n = 3$.

and is also equal to the total energy lost through viscous dissipation (in the equation above, $\mathbf{d}$ is the strain rate tensor). Using the squirming mode decomposition, Eq. (1.12)–(1.14), it can be computed in terms of the squirming mode amplitudes as

$$\mathscr{P}(t) = 12\pi\eta_f a \sum_{n=1}^{\infty} \gamma_n \alpha_n(t)^2, \quad \text{with } \gamma_1 = 1 \text{ and } \gamma_n = \frac{(2n+1)^2}{3n(n+1)} \quad \text{for } n \geq 2. \tag{1.17}$$

The squirmer model was extensively used in its steady ($\alpha_n(t) = \alpha_n$) and unsteady versions to study hydrodynamic interactions (Ishikawa *et al.*, 2006), mixing (Lin *et al.*, 2011), suspension rheology (Ishikawa *et al.*, 2007) and instabilities (Ishikawa & Pedley, 2007; Evans *et al.*, 2011). In this work, we use it to analyze optimal strokes for locomotion (Michelin & Lauga, 2010*a*) and feeding (Michelin & Lauga, 2011, 2013). Section 1.5 presents some of my recent work, based on the squirmer model, on the dynamics of active auto-phoretic particles, or chemical swimmers. The approach followed here considers exclusively tangential displacements of the surface (slip velocity) but the squirmer model can in fact be generalized to a larger variety of strokes associated with normal velocity at the interface. This normal velocity can be associated either with a jetting mechanism (Spagnolie & Lauga, 2010*a*) or with a displacement of the interface. In the latter case, the geometry is time-dependent and the squirmer's framework is only applicable through a perturbation analysis in the limit of small normal boundary displacements (Blake, 1971).

1.3 Optimal swimming strokes of model ciliates

To swim in low Re flows, *Paramecium* and other ciliates rely on the beating of many individual cilia distributed on their surface. Much shorter than the cell's body, they have similar diameter, beating frequency and internal structure to that of eukaryotic flagella. Both deform under a distributed actuation all along their length, resulting from the relative sliding of neighboring polymeric filament in microtubule doublets. As emphasized earlier, their mode of propulsion provide ciliates with two different means of breaking the time symmetry and produce a net forward motion: (i) through the asymmetric beating of each individual cilium and (ii) through the coordinated beating of neighboring cilia leading to the formation of so-called metachronal waves (Brennen & Winnet, 1977; Blake & Chwang, 1974). The origin of this synchronization is still debated, but several recent studies have suggested that hydrodynamic interactions between neighboring cilia might play an important role (Gueron *et al.*, 1997; Vilfan & Julicher, 2006; Lenz & Ryskin, 2006; Guirao & Joanny, 2007; Niedermayer *et al.*, 2008). Synchronization of cilia beating is also essential to many biological functions in the animal kingdom: metachronal waves of the cilia covering the lung epithelium produce a net mucus

flow that enables the evacuation of foreign particles out of the respiratory tract (Sleigh *et al.*, 1988), and the beating of cilia lining the oviduct are responsible for the egg transport (Halbert *et al.*, 1976). Several recent studies have suggested that cilia coordination in metachronal waves may reduce the collective energetic cost of beating (Gueron & Levit-Gurevich, 1999; Osterman & Vilfan, 2011).

In Michelin & Lauga (2010*a*), we consider this energy efficiency from a different perspective. Considering that the organism has access to a fixed amount of energy that it can dedicate to propulsion (determined, for example, by its metabolism), we search for the swimming stroke (i.e. the sequence of shape changes) that maximize the distance travelled. This question of optimality of a particular swimming pattern to a specific biological function is at the center of many recent studies on low-Re locomotion and generally takes two different forms, namely seeking optimal shapes or optimal gaits. In the former, the optimal morphology is considered (Vilfan, 2012) while the latter focuses on a particular organism and aims at determining the optimal sequence of body deformation that maximizes a particular biological performance function (Michelin & Lauga, 2010*a*, 2011, 2013; Tam & Hosoi, 2007, 2011*a*,*b*; Spagnolie & Lauga, 2010*b*; Eloy & Lauga, 2012; Osterman & Vilfan, 2011).

In this section and the following, we successively determine optimal swimming and feeding gaits. While the former maximize the distance travelled with a fixed amount of energy, the latter maximize the nutrient absorption under the same energetic constraint. To this end, we use the squirmer model presented in the previous section as a model for a ciliated cell. Computing the flow around a ciliate accurately is very complex and computationally expensive due to the number and deformable geometry of the flapping appendages. To address this problem, two different modeling approaches have been followed: (i) sublayer models and (ii) envelope models. The former explicitly considers the dynamics of the cilia layer either with a discrete representation of the cilia (Gueron & Liron, 1992, 1993) or with a continuum approach by modeling the cilia layer as a porous and deformable medium (Hussong *et al.*, 2011). Motivated by the relatively short length of the cilia with respect to the cell's body and by their dense coverage of the cell's surface, envelope models adopt a different approach, representing only the outer cilia layer (the cilia tips) through the deformation of a continuous surface (Brennen & Winnet, 1977; Blake & Sleigh, 1974). Optimizing the swimming stroke is therefore now equivalent to finding the optimal sequence of deformation of the envelope surface, a much simpler modeling route, well-suited for optimization computations.

1.3.1 The squirmer model as an envelope model: Lagrangian vs. Eulerian strokes

The presentation of the squirmer model in Section 1.2.4 voluntarily followed an Eulerian approach: the stroke is defined through a slip velocity field $\tilde{\mathbf{u}}(\mathbf{x},t)$ on the sphere corresponding to the instantaneous velocity of the material point located at position $\mathbf{x}$ at time t. The envelope model of a ciliate implicitly assumes that this spherical surface is a representation of the motion of the different cilia tips, which are material points connected through the cilium to a fixed basal attachment at the cell wall. Squirming strokes can therefore alternatively be described by the complete description of the cilia tips trajectories. For a dense distribution of the cilia, this can be done by defining a continuous field of trajectories $\mu = \xi(\mu_0,t)$ with μ_0 the average position, acting as a Lagrangian label of the trajectory. The Eulerian and Lagrangian formulations are related:

$$\forall(\mu_0,t), \quad \frac{\partial \xi}{\partial t} = -\frac{\sqrt{1-\mu^2}}{a} u_\theta(\mu = \xi(\mu_0,t),t). \tag{1.18}$$

The intensity of the squirming modes can therefore be defined indifferently from the slip velocity u_θ or the trajectory set ξ.

In the following, we are interested in the optimal periodic stroke. The definition of periodicity is however different in each framework: a periodic *Eulerian* stroke corresponds to a periodic slip velocity field ($\forall(\mu,t)$, $u_\theta(\mu,t) = u_\theta(\mu,t+T)$), while a periodic *Lagrangian* stroke corresponds to periodic Lagrangian trajectories ($\forall(\mu_0,t)$, $\xi(\mu_0,t) = \xi(\mu_0,t+T)$). Any periodic Lagrangian stroke is also a periodic Eulerian stroke,

but the reverse is in general not true. In particular, the pure treadmill swimmer ($\alpha_n(t) = \alpha_1\delta_{1n}$) is periodic in an Eulerian sense but corresponds to a non-periodic Lagrangian stroke: material points are continuously transported from one pole to the other.

1.3.2 Swimming efficiency

We use here the traditional definition of low-Re swimming efficiency, η,

$$\eta = \frac{\langle U \rangle \mathcal{T}^*}{\langle \mathscr{P} \rangle}, \tag{1.19}$$

where $\langle\cdot\rangle$ denotes the time-averaging operator over a swimming period, U is the swimming velocity and $\mathscr{P}$ is the energy cost of locomotion, defined here as the work of the squirmer's surface against the fluid. $\mathcal{T}^*$ is the force required to drag a rigid body of same shape as the swimmer at the same average velocity $\langle U \rangle$. Traditionally, referred to as an efficiency, η should more accurately be termed as a normalization of the energetic cost of locomotion since nothing imposes it to be less than 1. However, for most biological cells η is of the order of 1% (Lauga & Powers, 2009). Using Stokes's formula for the drag force on a rigid sphere as well as Eq. (1.17), the efficiency η is directly obtained in terms of the intensities of the squirming modes as

$$\eta = \frac{\langle \alpha_1 \rangle^2}{\sum_{n=1}^{\infty} \gamma_n \langle \alpha_n^2 \rangle}. \tag{1.20}$$

1.3.3 Optimal Eulerian (steady) stroke

In the Eulerian framework, finding the optimal swimming stroke is trivial as one may pick the functions $\alpha_n(t)$ without any constraint, therefore assigning all the energy to the swimming mode. Using the Cauchy–Schwartz inequality, it is immediate that $\eta \leq 1/2$ and that this upper bound can be achieved for the particular swimming stroke corresponding to a steady treadmill swimmer (Leshansky *et al.*, 2007):

$$\alpha_1(t) = \alpha_1 \quad \text{and} \quad \alpha_n(t) = 0 \quad \text{for } n \geq 2. \tag{1.21}$$

Note that this Eulerian optimal stroke is steady as the slip velocity does not depend on time.

1.3.4 Optimal Lagrangian stroke (periodic motion)

Finding the optimal stroke corresponding to a periodic motion of the surface (cilia tips) imposes following the Lagrangian point of view and describing the stroke through a set of trajectories $\xi(\mu_0, t)$. In the following, all quantities have been non-dimensionalized using the sphere's radius a, the stroke's frequency $\omega = 2\pi/T$ and the fluid viscosity η_f, so that the characteristic velocity is now ωa. For a given stroke $\xi(\mu_0, t)$, and using Eqs. (1.14), (1.18) and (1.19), one may compute the associated swimming efficiency $\eta[\xi]$. Considering a small perturbation $\delta\xi$ around a reference stroke ξ, and using the differential form of the above equations, the gradient $F[\xi](\mu_0, t)$ of the efficiency in the stroke space, defined as

$$\forall \delta\xi(\mu_0, t), \quad \delta\eta = \left\langle \int_{-1}^{1} F[\xi](\mu_0, t)\delta\xi(\mu_0, t)\mathrm{d}\mu_0 \right\rangle, \tag{1.22}$$

can be obtained analytically:

$$F[\xi](\mu_0, t) = \frac{2\eta}{\langle \alpha_1 \rangle} \frac{\partial^2 \xi}{\partial \mu_0 \partial t} - \frac{2\eta^2}{\langle \alpha_1 \rangle^2} \sum_{n=1}^{\infty} \gamma_n \left[\alpha_n L_n'(\xi) \frac{\partial^2 \xi}{\partial \mu_0 \partial t} + \frac{\partial}{\partial t} \left(\alpha_n L_n'(\xi) \frac{\partial \xi}{\partial \mu} \right) \right]. \tag{1.23}$$

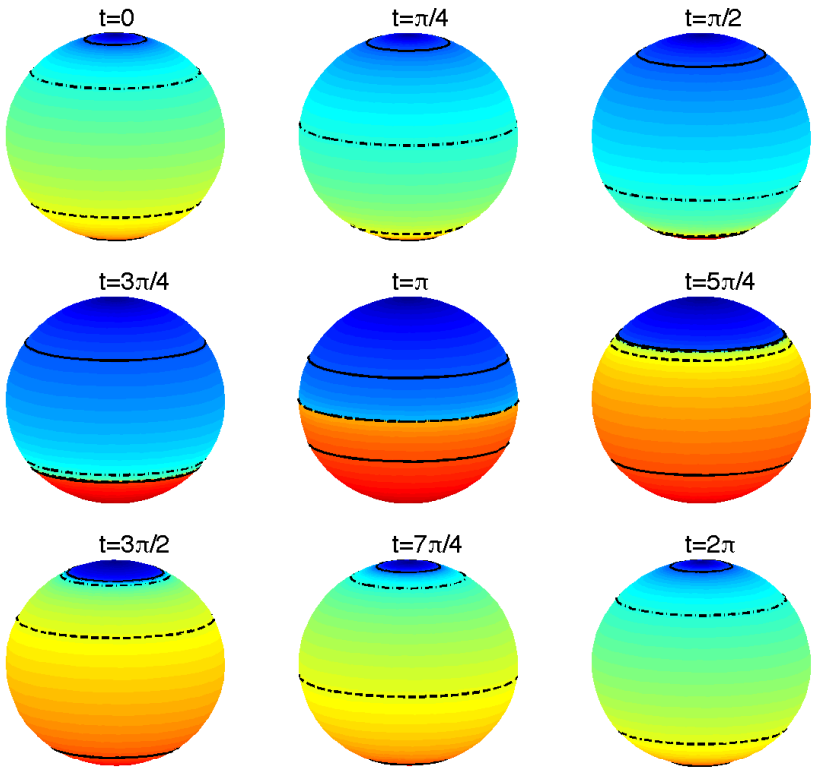

Figure 1.3: Snapshots of the displacement of the squirmer surface over a swimming period in the optimal unconstrained stroke $\Theta_{\max} \approx 53°$, $\langle U \rangle \approx 0.33$, $\eta \approx 22.2\%$. The surface color of each material point on the surface refers to the mean polar angle of that material point. Black lines following material points on the surface have also been added for clarity.

After projection of this gradient onto the subspace of acceptable strokes satisfying (i) the periodicity, (ii) the absence of displacement at the poles and (iii) the monotonicity in μ_0 for all time (guaranteeing that cilia do not cross and that Eulerian fields are single-valued), the resulting gradient $\tilde{F}$ can be used to optimize the efficiency η with respect to the swimming stroke ξ using a steepest-ascent algorithm. More details on the derivations above and the numerical techniques used can be found in Michelin & Lauga (2010*a*).

Starting the optimization algorithm from a variety of initial conditions, the calculation converges toward an optimal stroke whose kinematics is shown in Figure 1.3. This optimal stroke can be decomposed into two phases: (i) an effective stroke where the surface stretches from front to back (corresponding to cilia tips getting further away from each other) generating a large instantaneous velocity and (ii) a recovery stroke characterized by a return of the cilia tips to their original position in the form of a shock-like structure that minimizes its impact on the swimming velocity.

Although the motion of each individual material point remains highly symmetric (each point spends about 50% of a period traveling in one direction or the other), this stroke is characterized by a strong asymmetry at the organism level: at the equator, the slip velocity is oriented from front to back for more than 90% of the period. This symmetry-breaking results from a small phase shift in the periodic motion of neighboring cilia tips and is highly reminiscent of the metachronal waves observed in most ciliate species. The metachronal wave here is antiplectic (i.e. the direction of the wave is opposite to the direction of the effective stroke) which is purely a result of the envelope model formulation (Michelin & Lauga, 2010*a*).

The optimal stroke pictured in Fig. 1.3 is characterized by an efficiency that is much larger than what

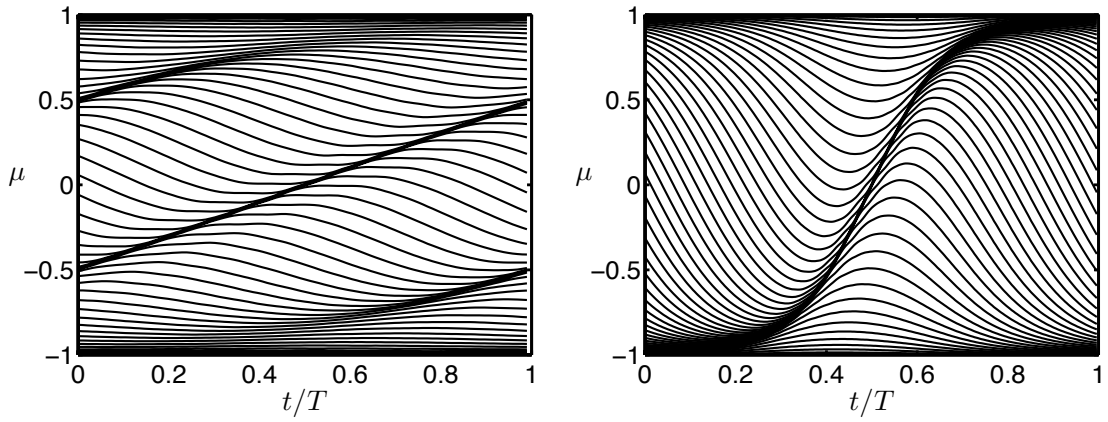

Figure 1.4: Trajectories of the optimal swimming strokes for $\Theta_{\max} \approx 11°$ ($\eta \approx 6\%$, left) and $\Theta_{\max} \approx 53°$ ($\eta \approx 22\%$, right). $\mu = 1$ (resp. $\mu = -1$) corresponds to the front (resp. back) of the squirmer.

is typically found for swimming micro-organisms, but also by a large amount of stretching of the squirmer's surface throughout the stroke. This stretching corresponds to a large excursion of cilia tips around their mean position, namely a maximum azimuthal amplitude greater than 50°. In a real ciliated microswimmer, the displacement of the cilia tip is constrained by the cilia length-to-cell size ratio. For *Paramecium*, this ratio is about 5% and corresponds to a maximum displacement angle of about 5°.

The optimization described above can be repeated with a penalization on the maximum cilia tip excursion to constrain our optimization to a subset of strokes with smaller amplitudes. The trajectories of the optimal stroke with $\Theta_{\max} = 11°$ are shown in Figure 1.4 and compared to that of the optimal swimmer in Figure 1.3. The same structure for the stroke is recovered with the decomposition (in space and time) of the stroke into an effective part (stretching) and a recovery part (shock). Moreover, a direct relationship between $\Theta_{\max}$ and η is also obtained (Figure 1.5).

This decomposition of the optimal strokes, regardless of their amplitude, suggests the following analysis: to be efficient instantaneously, the organism must dedicate as much of its energy as it can to mode 1 (swimming), and the existence of shock-like structures make the trajectories periodic while minimizing the resistive effect on the flow. An ansatz for the optimal stroke can therefore be designed by super imposing shock waves to the treadmill solution (Figure 1.6). Inside the shock, the velocity field is defined explicitly to ensure the periodicity of all trajectories. Such a stroke is described by three parameters: the swimming velocity, the shock velocity and the shock thickness. The result of the efficiency optimization over this reduced stroke space is shown in Figure 1.5 and shows very good agreement with the full optimization. Further, it extends the optimal curve beyond the swimmer of Figure 1.3 and shows that the upper bound efficiency of 50% can be reached asymptotically for $\Theta_{\max} \to 90°$. Because of its Lagrangian approach, the numerical optimization approach presented above is not able to capture such strokes as they become too singular.

Despite the simplicity of this model, our results identify the optimal swimming strokes of model ciliates as those breaking the time-symmetry through the cilia coordination into patterns similar to metachronal waves. The optimal efficiencies are consistent with those observed in nature for the correct range of amplitudes. This approach is however limited by its simplified framework: cilia being only described through the motion of their tip, this model accounts neither for the asymmetry in the two half-strokes of an individual cilium's motion nor for the energetic dissipation within the cilia layer. One consequence is for example that only anti-plectic metachronal waves can be obtained (Michelin & Lauga, 2010*a*). To be able to study such effects, a more elaborate (and computationnally expensive) model should be considered (see for example Osterman

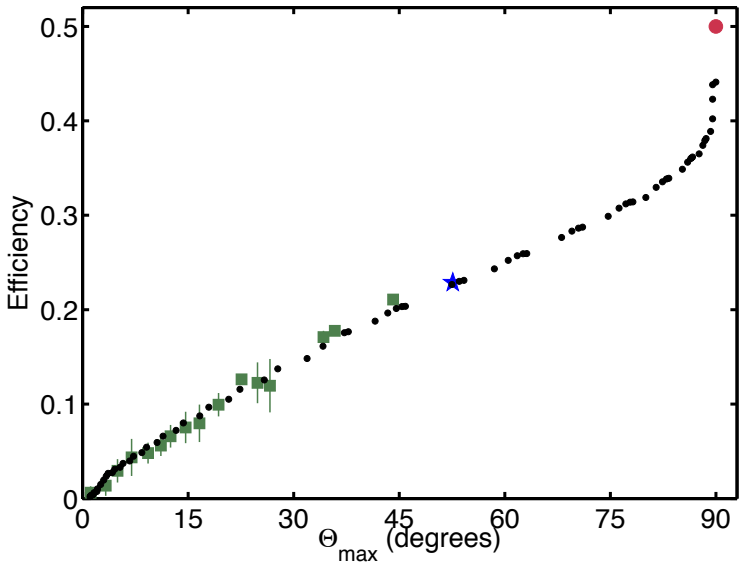

Figure 1.5: Swimming efficiency as a function of the maximum displacement angle of the cilia tips $\Theta_{\max}$: result of the numerical optimization (green squares), optimal strokes obtained from the ansatz (black dots). The blue star corresponds to the numerical optimal shown in Fig. 1.3 and the red circle corresponds to the Eulerian (steady) optimal stroke (treadmill swimmer).

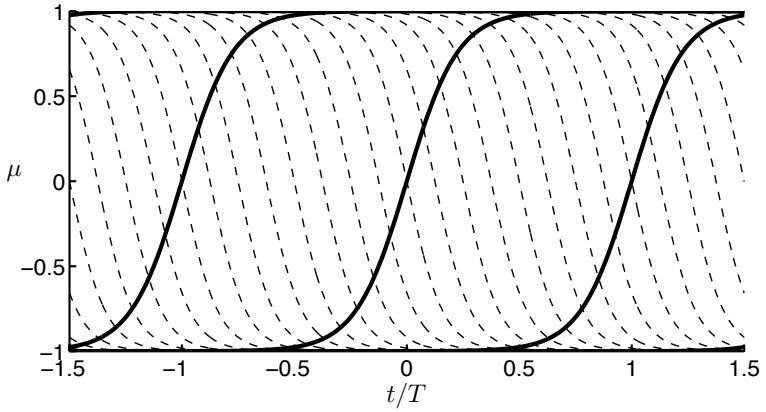

Figure 1.6: Construction of the analytical ansatz for the optimal swimming strokes. Dashed lines represent the treadmill solution (the Eulerian or steady optimal swimming stroke). The stroke is made periodic through the introduction of shock-like regions (thick solid) where the velocity field is constructed so as to make all trajectories periodic.

& Vilfan, 2011; Eloy & Lauga, 2012; Vilfan, 2012)

1.4 Impact of swimming on feeding and optimal feeding strokes

The metabolism of swimming micro-organisms heavily relies on exchanging a variety of chemical or organic species with their environment, from dissolved gases to larger proteins. The swimming stroke of an organism impacts its ability to "feed" on such passive tracers in two different ways: (i) the resulting motility enables the organism to sense and travel toward regions richer in nutrients, and (ii) the flow generated by the organism stirs nutrients and modifies local gradients, thereby altering diffusive fluxes and intake. This section focuses on the latter effect to quantify the impact of the swimming-induced flow on the feeding performance of different swimming strokes. Further, generalizing the approach of the previous section where strokes maximizing the distance travelled for a fixed energetic cost were sought, we consider and determine the optimal strokes maximizing the nutrient uptake instead.

Unlike the swimming problem, the feeding problem is characterized by two different and independent time-scales: (i) an advective time-scale intrisically linked to the imposed slip velocity $\tau_{\text{adv}} \sim a/U_S$ and (ii) a diffusive time-scale $\tau_{\text{diff}} \sim a^2/D$ with D the diffusivity of the nutrient considered. The Péclet number $\text{Pe} = \tau_{\text{diff}}/\tau_{adv}$ is a relative measure of the advective effects of the swimming stroke on the diffusive intake of nutrients and varies by several orders of magnitude depending on the problem considered, ranging from $\text{Pe} \approx 10^{-2}$ for a small bacteria feeding on dissolved oxygen molecules to $\text{Pe} \approx 10^3$ for *Paramecium* feeding on smaller bacteria.

1.4.1 The feeding problem

The squirmer model presented previously is extended here to study the advection-diffusion of a passive tracer around the cell. This effectively extends to arbitrary and unsteady strokes the work of Magar *et al.* (2003) and Magar & Pedley (2005). The Péclet number is defined as

$$\text{Pe} = \frac{1}{D}\sqrt{\frac{\mathscr{P}\, a}{12\pi\eta_f}}, \tag{1.24}$$

effectively constructing the reference velocity scale on the characteristic slip velocity. For simplicity, we consider here the case of a uniform far-field concentration C_∞ and consider that a chemical equilibrium is reached at the surface of the cell so that $C = C_b < C_\infty$. A more realistic but more complex treatment of the surface kinetics was proposed by Magar *et al.* (2003), including membrane resistance to nutrient absorption, diffusion of nutrients within the cell and finite-time kinetics of their consumption. Here, the rescaled nutrient concentration $c = (C_\infty - C)/(C_\infty - C_b)$ satisfies the following non-dimensional advection-diffusion problem

$$\frac{\text{Pe}}{\sqrt{\mathcal{P}}}\left[\frac{\partial c}{\partial t} + \mathbf{u}\cdot\nabla c\right] = \nabla^2 c, \quad c(r\to\infty) = 0, \quad c(r=1) = 1, \tag{1.25}$$

In Eq. (1.25), $\mathcal{P} = \sum \gamma_n \left\langle \alpha_n^2 \right\rangle$ is the non-dimensional energy cost of the swimming stroke, and $\mathbf{u}$ is the velocity field generated by the swimming stroke, Eq. (1.12). The average instantaneous nutrient uptake is

$$J(t) = -\frac{1}{4\pi}\int_{\mathcal{S}} \mathbf{n}\cdot\nabla c \,\mathrm{d}S. \tag{1.26}$$

In the diffusive limit, $\text{Pe} \ll 1$, feeding is only weakly impacted by the swimming stroke and is equivalent to that of a purely rigid sphere: the nutrient concentration is then isotropic ($c = 1/r$) and the nutrient uptake (in dimensional form) is time-independent $J(t) = 1$. Hence, $J(t)$ can be seen as a measure of the nutrient

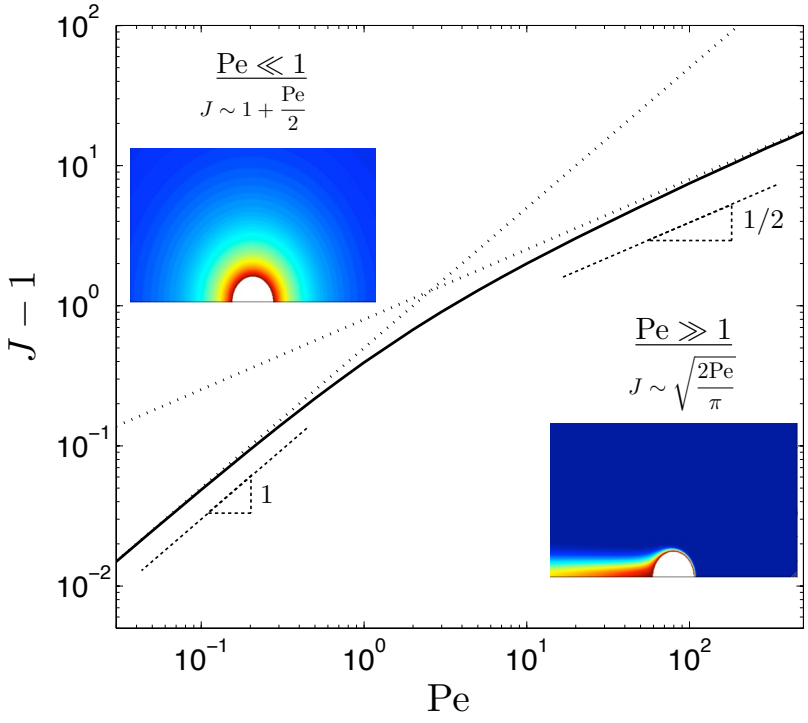

Figure 1.7: Effect of Pe on the nutrient flux J for the pure treadmill swimmer. Snapshots of the nutrient distribution in both limits $\mathrm{Pe} \ll 1$ and $\mathrm{Pe} \gg 1$ are shown for reference as well as asymptotic scalings.

flux relative to the purely diffusive regime. For a given periodic stroke (e.g. given $\alpha_n(t)$ or given surface trajectories), the nutrient concentration $c(\mathbf{r}, t)$ is computed numerically. The numerical details can be found in Michelin & Lauga (2011, 2013).

1.4.2 How does swimming impact feeding?

Considering the simplest (and most efficient) swimming stroke, a pure treadmill squirmer, Figure 1.7 shows that swimming enhances the feeding rate significantly. Two regimes can be identified corresponding to two different scalings of the net gain in nutrient uptake $\langle J \rangle - 1$. For $\mathrm{Pe} \ll 1$, diffusion dominates and the nutrient concentration around the squirmer is close to isotropic. Swimming however enables the organism to sweep regions of fresher nutrient content with an effective cross-section $R_{\mathrm{eff}} \sim a$ that does not depend on the swimming velocity; hence, the nutrient uptake increases linearly with Pe. The physical picture is remarkably different for $\mathrm{Pe} \gg 1$: advection of the nutrient dominates except in a thin boundary layer of thickness $\delta \sim a/\sqrt{\mathrm{Pe}}$ near the swimmer's boundary. As a result, $\langle J \rangle$ only scales as $\mathrm{Pe}^{1/2}$ corresponding to a velocity-dependent effective cross-section $R_{\mathrm{eff}} \sim \delta$. For steady and arbitrary Eulerian strokes, the variations of J in both limits were obtained using asymptotic analysis in Michelin & Lauga (2011) (see also Magar *et al.*, 2003).

More insight on the impact of swimming on feeding for a general unsteady stroke can be gained from asymptotic analysis in the limit of $\mathrm{Pe} \ll 1$: for all strokes, the leading order correction to the average feeding rate $\langle J \rangle$ scales linearly with Pe and only depends on the average swimming velocity. The leading order correction to the fluctuations $J'(t) = J(t) - \langle J \rangle$ is found to scale as $\mathrm{Pe}^{3/2}$. The remarkable result is that, corrections at this order (both mean and fluctuations), only depend on the swimming velocity $U(t)$, and not on any higher order squirming mode. This has an immediate consequence: strokes creating an instantaneous

motion of the organism but no net displacement over a period (e.g. reciprocal strokes for which $U(t) \neq 0$ and $\langle U \rangle = 0$) show a greater feeding performance over strokes where the organism stirs the fluid while holding a stationary position ($U(t) = 0$). Furthermore, these results also show that, at small Pe, the optimal feeding strokes are simply the optimal swimming strokes of Section 1.3.

To confirm these results, numerical simulations of the nutrient concentrations were performed for a large variety of swimming strokes. Figure 1.8 shows the evolution of this distribution in time as well as that of the feeding rate for three typical strokes of decreasing swimming efficiency. Stroke A corresponds to the optimal swimming stroke of Figure 1.3. Strokes B and C correspond to harmonic displacements of individual cilia tips and differ on the cilia synchronization: Stroke C corresponds to synchroneous beating (reciprocal) and Stroke B to a weak metachronal wave. For strokes A and B, the average swimming motion allows the squirmer to create a sharper concentration gradient at the front that greatly enhances the nutrient uptake, while the nutrient distribution remains relatively isotropic for Stroke C. Figure 1.9 decomposes the variations of $J(t)$ for the three strokes in terms of a mean feeding rate, a fluctuating feeding rate amplitude and the unitary fluctuations, and shows excellent agreement between the asymptotic predictions and the numerical results. Noticeably, for swimming strokes, the feeding rate appears to have a phase delay with respect to the velocity field. The asymptotic analysis prediction (a phase shift of $\pi/4$) appears consistent with the observations (even at $\mathrm{Pe} = O(10)$ for the most efficient strokes), and can be interpreted as the formation time of the concentration gradients when the cell accelerates.

These results emphasize the critical impact of the swimming velocity (mean and fluctuations) on the feeding ability of the cell, regardless of the value of Pe. This is illustrated in Figure 1.10 where the mean feeding rate is plotted against $\mathrm{Pe} \times U$: the collapse of most data points on a single curve (precisely that of the purely swimming squirmer) indicates that the swimming velocity U determines at leading order the average nutrient uptake. The other components of the strokes (e.g. stirring, ...) only become significant when U is small (corresponding to data points located above the main trend). This therefore suggests a close link between optimal swimming and optimal feeding, a conjecture that is confirmed in Figure 1.10 where the feeding performance of the squirmer appears directly correlated to its swimming efficiency: the most efficient feeding stroke seems to be the pure treadmill ($\eta = 50\%$). In fact, Michelin & Lauga (2011) proved analytically that the optimal steady feeding stroke slightly differs from the pure treadmill but that this difference is so small (less than 10^{-3}) that it is neither noticeable nor physically relevant.

1.4.3 Optimal feeding strokes are optimal swimming strokes

These results suggest that the optimal feeding and optimal swimming strokes are essentially identical. To confirm this numerically using direct optimization, an adjoint-based framework was developed to compute the gradient of the feeding rate with respect to the feeding stroke. The details of this method are omitted here for clarity and can be found in Michelin & Lauga (2011, 2013). Solving for the adjoint field g that satisfies the adjoint advection-diffusion problem

$$\frac{\mathrm{Pe}}{\sqrt{\mathcal{P}}}\left(\frac{\partial g}{\partial t} + \mathbf{u}\cdot\nabla g\right) = -\nabla^2 g, \quad g(r\to\infty) = 0, \quad g(r=1) = 1, \tag{1.27}$$

it is possible to compute explicitly the gradient in the stroke space of the average nutrient uptake, and to project it on the subspace of swimming strokes of fixed energy cost $\mathcal{P}$. Following the same approach as in Section 1.3, we (i) perform an optimization of the stroke to maximize the feeding rate for a fixed amount of energy dedicated to locomotion and (ii) introduce a penalization to restrict the optimization to Lagrangian strokes with a limited displacement of the cilia tips. The results of this optimization confirm our conjecture: the optimal feeding stroke is essentially the same as the optimal swimming stroke, regardless of the type of strokes considered (Eulerian stroke, Lagrangian stroke, Lagrangian stroke with limited amplitude) and regardless of the relative importance of advection and diffusion (measured by Pe).

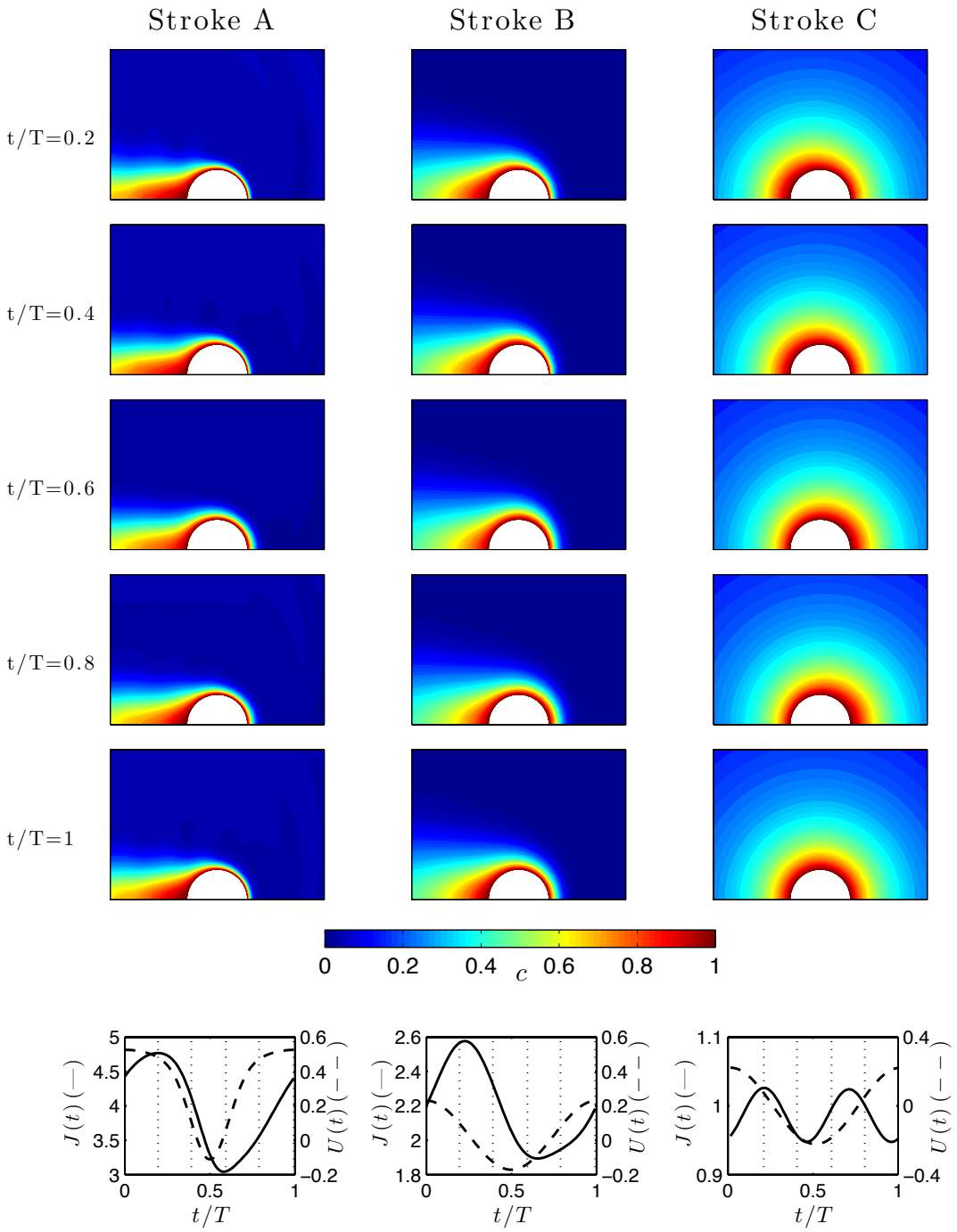

Figure 1.8: (Top) Nutrient concentration around the organism at Pe = 30 for stroke A (left), stroke B (center) and stroke C (right). (Bottom) Evolution in time of the feeding rate (solid) and swimming velocity (dashed) for strokes A, B and C (left to right); the dotted lines indicate the time corresponding to each of the five snapshots above.

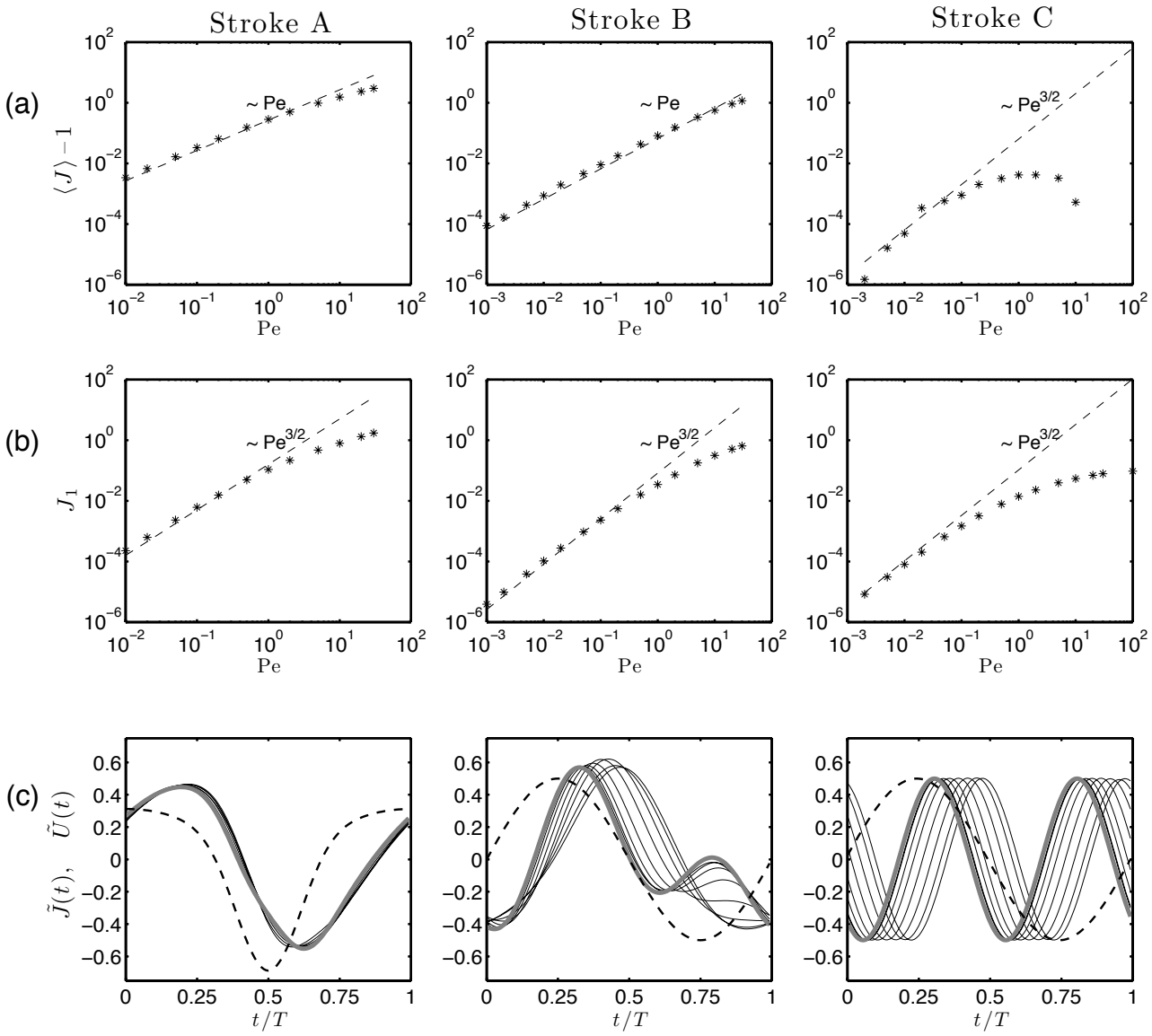

Figure 1.9: Dependence on Pe of (a) the mean feeding rate, $\langle J \rangle$, (b) the peak-to-peak amplitude of the feeding rate fluctuations J_1 and (c) the rescaled (unit) feeding rate (solid) and velocity (dashed) fluctuations in time. In (a) and (b), the asymptotic prediction is shown as a dashed line. In (c), the asymptotic prediction for the feeding rate fluctuations is shown as a thick grey line. All results are plotted for stroke A (left), stroke B (center) and stroke C (right).

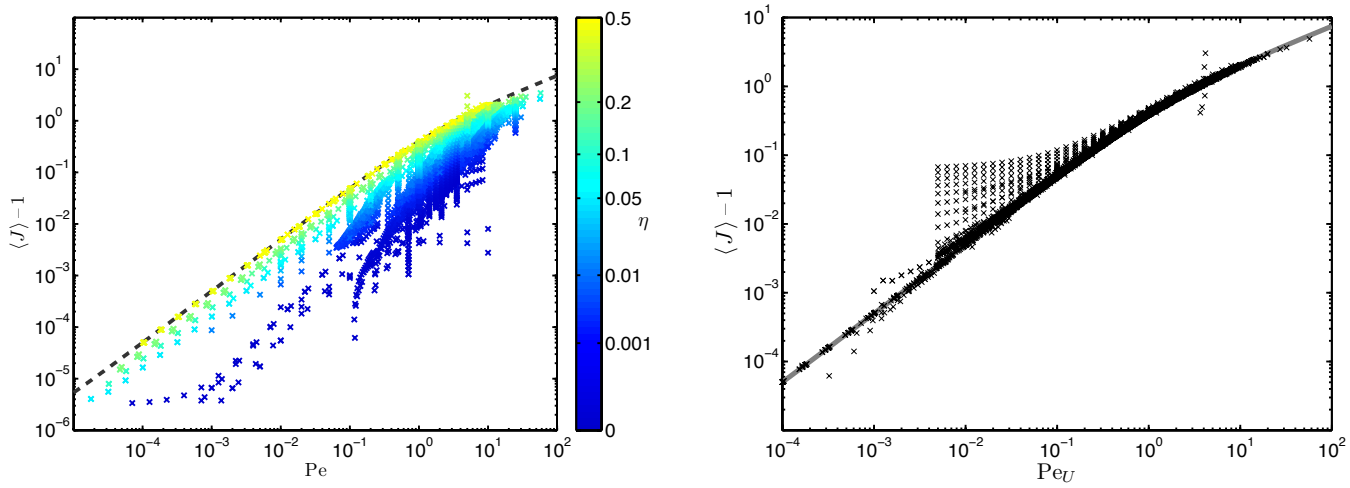

Figure 1.10: (Left) Mean feeding rate as a function of Pe. (Right) Mean feeding rate as a function of $\mathrm{Pe}_U = \mathrm{Pe}\,U$. Both figures include the results of about 8500 different swimming strokes. On the left, the symbol color shows the stroke efficiency η.

1.4.4 Conclusions

This apparently simple result, which stems from the intimate link between nutrient uptake and swimming velocity, was clearly not obvious *a priori*: as shown in Figure 1.7, the feeding performance of a given stroke, and therefore also the optimal nutrient uptake that an organism can achieve, does depend critically on Pe. What is shown here is that the way to achieve this optimal uptake, namely the optimal swimming stroke, does not depend on Pe, a result that has significant consequences from a biological point of view. First of all, a particular organism does not have to choose between two biological functions (feeding and swimming) if it tries to minimize its energy consumption. Also, for an organism that relies on multiple chemical species that might have quite different diffusivity properties (and therefore associated Pe), the stroke maximizing the nutrient uptake is independent of the chemical species.

1.5 Swimming with no deformation or actuation: autophoretic swimmers

The surging interest over recent years to study the mechanisms at the source of micro-organisms motility in viscous flows corresponds to a search for a better understanding of these mechanisms (and their modification in mutant cells), but also to an engineering challenge of designing artificial micro-swimmers or self-propelled micro-robots. In that regard, swimming micro-organisms represent a source of inspiration for biomimetic designs. Applications for such robots may be found particularly in the domain of biomedical engineering, for example in targeted drug delivery. The challenges to reach such a goal are enormous, even just to achieve the self-propulsion of a micro-robot that can realistically be microfabricated, and so far, no genuinely self-propelled micro-robot has been successfully manufactured. Instead, biomimetic propellers actuated through an external magnetic forcing currently represent a very active area for research and development (Dreyfus *et al.*, 2005; Ghosh & Fischer, 2009; Gao *et al.*, 2010; Tierno *et al.*, 2010; Pak *et al.*, 2011; Coq *et al.*, 2011, to cite only a few), although the basic need for an external field to create the deformation or chiral motion leading to propulsion is an intrinsic limitation of such devices in many engineering applications.

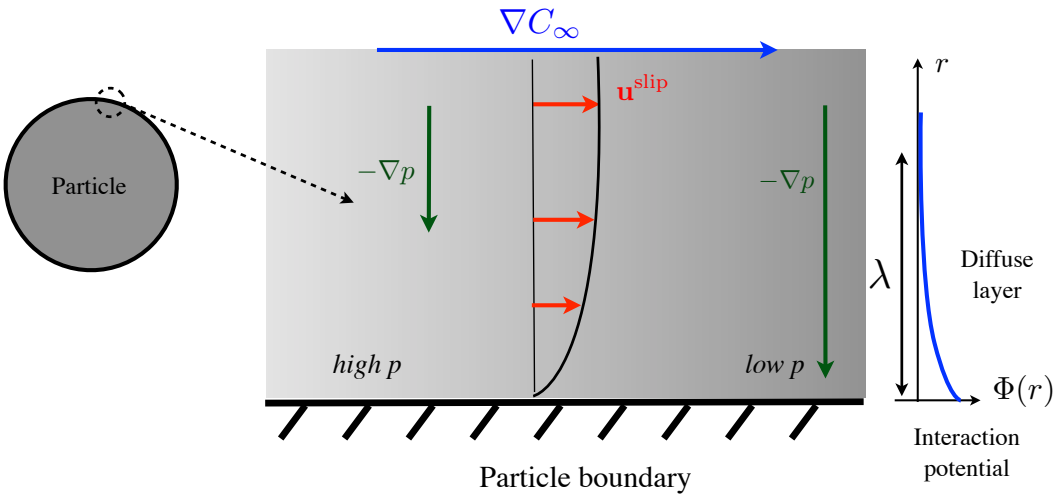

Figure 1.11: Diffusiophoretic effect. Near the particle's surface, the interaction forces $-\nabla\Phi$ (here repulsive) between the solute and the surface create a strong normal pressure gradient. When a concentration gradient is present in the far-field, a longitudinal pressure gradient develops near the surface and creates a net slip velocity outside the diffuse layer of thickness λ.

1.5.1 Surface interactions and mobility

An alternative approach consists in designing autonomous self-propelled particles able to effectively generate slip velocities near their surface, achieving locomotion through a route rather similar to the model squirmer described at length in the previous sections. The origin of this slip velocity lies in the short range interactions of solute species in the fluid phase with the particle's boundary (Figure 1.11). Solute concentration gradients along the surface create local imbalances in the osmotic pressure field at the origin of a net slip velocity outside a diffuse layer. The thickness of this layer, λ, is determined by the typical range of the interaction forces and is therefore very small in comparison with any geometric characteristic of the particle. This mechanism, known as diffusiophoresis, is responsible for the net motion of colloid particles in externally imposed solute gradients, and shares many similarities with other mechanisms such as electrophoresis (response to an electric potential gradient) or thermophoresis (response to a temperature gradient) (see the very complete review of such processes by Anderson, 1989). Later on, I will focus exclusively on the diffusiophoresis framework, keeping in mind that many tools or conclusions may be applicable to these other phenomena. In the case of diffusiophoresis of a rigid particle, the slip velocity is obtained as (Anderson, 1989)

$$\tilde{\mathbf{u}} = \mathcal{M}(\mathbf{1} - \mathbf{nn}) \cdot \nabla C, \quad \mathcal{M} = -\frac{kT\lambda^2}{\eta_f} \int_0^\infty y \left(\mathrm{e}^{-\Phi(y)/kT} - 1 \right) \mathrm{d}y \tag{1.28}$$

with C the concentration of the solute around the particle and $\Phi(d/\lambda)$ the interaction potential of the solute at a distance d from the colloid's surface. $\mathcal{M}$ is the mobility of the colloid and is positive (resp. negative) in the case of repulsive (resp. attractive) solute-surface interactions.

1.5.2 Self-propulsion of anistropic autophoretic particles

If classical diffusiophoresis relies on the existence of an external forcing and therefore suffers from the intrinsic limitations presented earlier for magnetically-driven artificial swimmers, this mechanism offers an interesting route to self-propulsion when the particle is able to modify the local solute concentration through

emission or absorption of solute particles, for example through reaction catalysis at the surface (Paxton *et al.*, 2004; Kline *et al.*, 2005; Howse *et al.*, 2007; Ebbens & Howse, 2010; Zhao & Pumera, 2012). In these studies, Janus colloid particles or patterned rods are considered with asymmetric surface chemical properties: typically one half catalyzes a chemical reaction (e.g. the dissociation of hydrogen peroxide) and the other half is chemically inert. Through chemical reactions at their surface, such colloids generate an anisotropic flux of solute in or out of the fluid domain, leading to a solute concentration gradient along their boundary. This results in an asymmetric slip velocity, Eq. (1.28), and self-propulsion of the particle, Eq. (1.7).

As for real micro-organisms, such artificial fuel-based micro-swimmers need to break symmetry to swim and this is achieved here through the anisotropic chemical treatment of their surface. The problem has received a considerable amount of interest in recent years both experimentally and theoretically, following in particular the establishment of a simple and generic model for this autophoretic system (Golestanian *et al.*, 2005, 2007). This model follows a continuum approach, describing the solute dynamics through its concentration $C(\mathbf{x}, t)$ around the colloid. The activity of the colloid particle (i.e. the absorption or release of solute imposed by the chemical properties of the surface) is $\mathscr{A}(\mathbf{x})$ on the boundary, with the convention that $\mathscr{A} > 0$ corresponds to a solute emission. Initially, described only in the purely diffusive case (the flow generated by the phoretic slip velocity has no impact on the concentration distribution), it can be extended to include the full advection diffusion dynamics of the solute (see for example Sabass & Seifert, 2012*a*,*b*). This framework couples the Stokes equations for the fluid

$$\eta_f \nabla^2 \mathbf{u} = \nabla p, \quad \nabla \cdot \mathbf{u} = 0, \tag{1.29}$$

to the advection diffusion for the solute concentration

$$\frac{\partial C}{\partial t} + \mathbf{u} \cdot \nabla C = D \nabla^2 C, \tag{1.30}$$

through the following boundary conditions on the surface of the particle:

$$-D\mathbf{n} \cdot \nabla C = \mathscr{A}(\mathbf{r}), \qquad \mathbf{u}(\mathbf{x}) = \mathcal{M}(\mathbf{1} - \mathbf{nn}) \cdot \nabla C \qquad \text{for } \mathbf{x} \in \mathcal{S} \tag{1.31}$$

where for simplicity the mobility $\mathcal{M}$ is assumed uniform here. In the far-field, $\mathbf{u} \to -\mathbf{U}$ and $C \to C_\infty$ with $\mathbf{U}$ the unknown "swimming" velocity that is determined through the no-force requirement on the particle. In the following, unless specified otherwise, we focus mostly on the steady state (assuming such a state exists) so that $\partial/\partial t = 0$.

Within this formalism (fixed solute flux at the boundary), the sign of $\mathcal{M}$ only matters in comparison with that of $\mathscr{A}$, and the far-field concentration of the solute does not play any role. Note, that this latter property wouldn't hold if the surface chemistry was represented as an absorption reaction $S \to \emptyset$ of the solute characterized by a constant of reaction $k(\mathbf{r})$ non-uniform on the surface; in that case, $\mathscr{A} = -k(\mathbf{r})C$ (see for example Córdova-Figueroa & Brady, 2008; Brady, 2010) and the activity of the particle depends on the far-field concentration of the solute.

In the present framework, the characteristic solute concentration is prescribed by the activity $[C] = \frac{\mathcal{A}a}{D}$, where $\mathcal{A}$ is the typical scale of the activity (e.g. mean value or peak value) and the typical velocity scale is $[U] = |\mathcal{M}|[C]/a = |\mathcal{M}\mathcal{A}|/D$. Note that this velocity scale does not depend on the size of the particle a. From this velocity scale, a measure of the importance of advective effects is the Péclet number Pe:

$$\mathrm{Pe} = \frac{|\mathcal{M}\mathcal{A}|a}{D^2}. \tag{1.32}$$

The sign of $\mathcal{M}\mathcal{A}$ characterizes the type of particles (emitting vs. absorbing) and their interaction with the solute (repulsive vs. attractive). Pe is the only non-dimensional parameter of the problem and can be seen

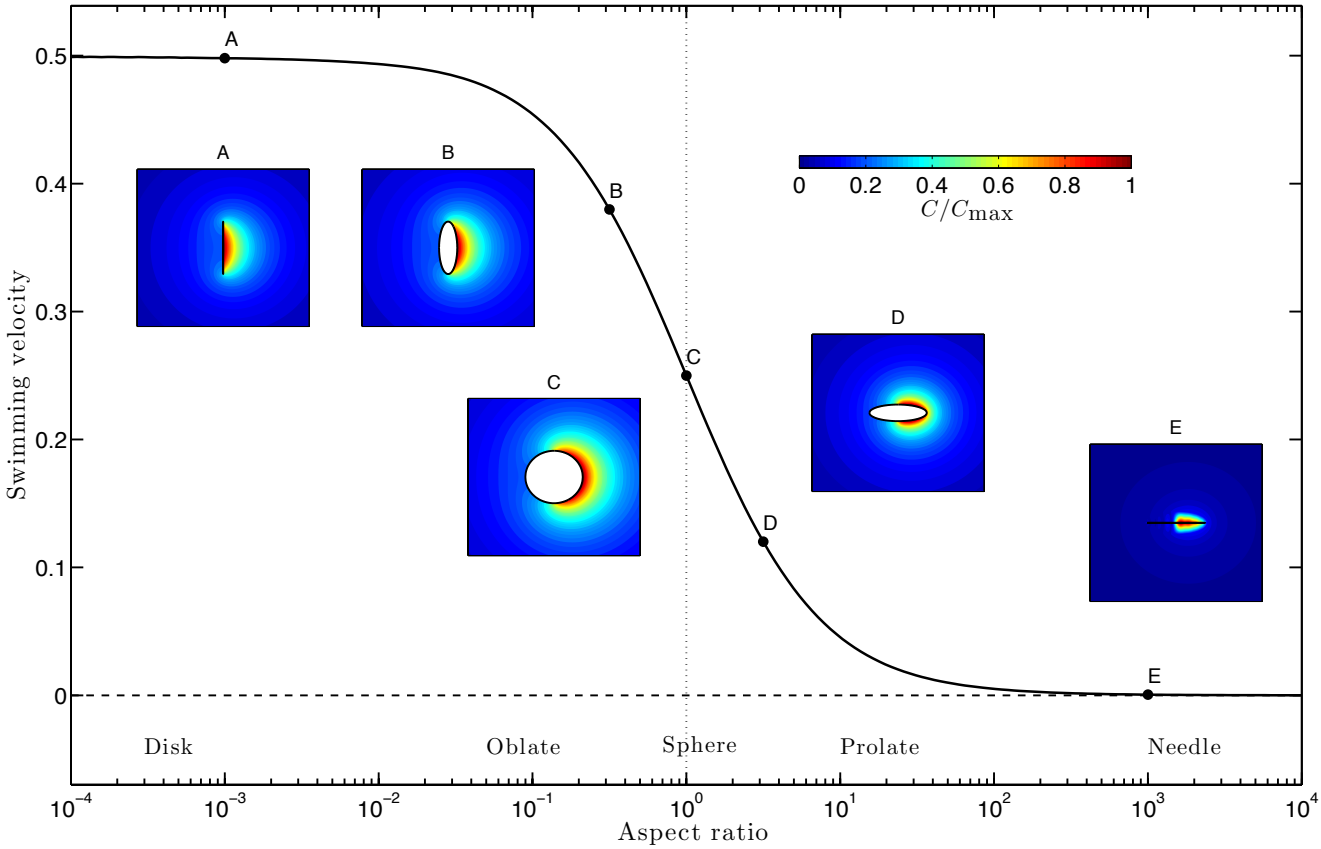

Figure 1.12: Evolution of the swimming velocity with the aspect ratio of an ellipsoidal colloid in the case of an attracting ($\mathcal{M} < 0$) particle emitting solute ($\mathcal{A} > 0$). The solute distribution is also represented for sample cases and the swimming velocity is oriented to the right.

as a measure of the particle's radius. For small particles, diffusive effects will be dominant while advection is likely to become important for larger particles.

For simplicity, a particularly simple geometry is considered here, namely a sphere of radius a and the formalism presented in the previous sections is used to (i) find the solution for the velocity field in terms of the slip velocity Eq. (1.14), and (ii) solve for the solute concentration around the colloid particle. The reciprocal theorem Eq. (1.7) and definition for the slip velocity Eq. (1.28) provide the swimming velocity, in non-dimensional form, in terms of the first azimuthal moment of the solute distribution:

$$U = -M \int_{-1}^{1} \mu \, C(r = 1, \mu) \mathrm{d}\mu. \tag{1.33}$$

where $M = \mathrm{sign}(\mathcal{M}) = \pm 1$. For a Janus colloid ($\mathscr{A}(\mathbf{x}) = \mathcal{A}$ if $\mu > 0$ and $\mathscr{A} = 0$ otherwise) and in the limit of $\mathrm{Pe} = 0$, the modification of the solute distribution $C(\mathbf{r}) - C_\infty$ can be obtained explicitly, and the non-dimensional velocity is computed exactly as $U = -MA/4$ (with $A = \mathcal{A}/|\mathcal{A}|$). This result can be easily extended to a coverage of the particle that is not hemispheric (see for example Golestanian *et al.*, 2007). For a hemispheric split, the stresslet associated with the generated velocity field (related to α_2 and the second moment of the surface solute concentration) is necessarily zero.

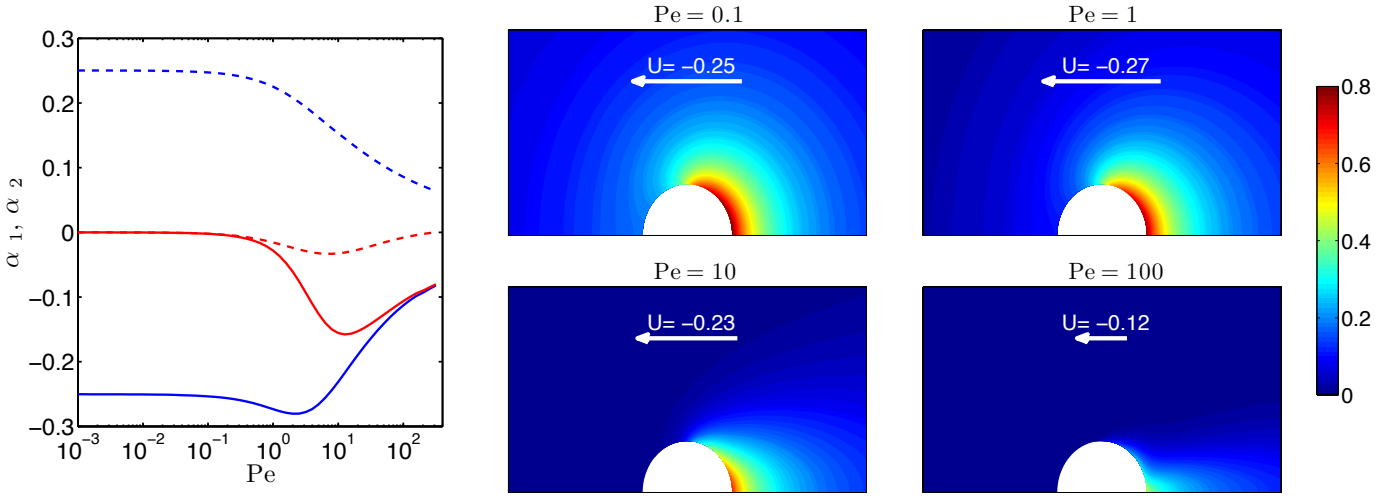

Figure 1.13: (Left) Evolution with Pe of the swimming velocity ($U = \alpha_1$, blue) and stresslet ($\Sigma = 10\pi\alpha_2/3$, red) for a Janus colloid and $AM > 0$ (solid) or $AM < 0$ (dashed). (Right) Solute distribution around the particle for increasing Pe and $AM > 0$.

With a bit more algebra, it is possible to generalize this approach to an ellipsoid Janus and to obtain the swimming velocity and solute distribution for different aspect ratios (Figure 1.12): the limit case of a disk, with one inert side and one catalytic side, is seen to swim twice as fast as the sphere while a needle-shaped particle does not asymptotically swim: the concentration gradients and slip velocity are only non-negligible in the central region that has infinitesimal perimeter (see also Popescu *et al.*, 2010).

When $\mathrm{Pe} \neq 0$, the solute advection modifies the local gradients and the slip velocity. The phoretic problem, Eqs. (1.29)–(1.31), must now be solved numerically through an extension of the methods used in Sections 1.3 and 1.4. Figure 1.13 shows the evolution with Pe of the swimming velocity and stresslet of a Janus swimmer. When $\mathrm{Pe} \ll 1$, one recovers the analytical diffusive solution (finite velocity and no stresslet). When Pe increases, two cases can be found for the velocity depending on the sign of MA: either a monotonic decrease to zero or an initial increase, leading to an optimal Pe (or radius) for maximum swimming velocity. For larger Pe, the velocity scales as $\mathrm{Pe}^{-1/3}$. This result is consistent with Brady (2010) and Jülicher & Prost (2009) and can be interpreted as follows. For large Pe, advection becomes dominant and a boundary layer forms around the particle as in the feeding problem presented in section 1.4. The radial solute gradient remains $O(1)$ (it is fixed by the activity) so the boundary layer thickness and the characteristic surface concentration follow the same scaling, Pe^a, and the definition of the slip velocity imposes that the slip velocity also behaves like Pe^a The boundary layer thickness is determined by a balance of the tangential advection and normal diffusion and leads to $(U, C, \delta) = O(\mathrm{Pe}^{-1/3})$, a result consistent with the numerical simulations. For anisotropic colloids, the swimming velocity is therefore reduced for large particles.

It is interesting to note that for intermediate Pe the colloid creates a non-zero stresslet that is always negative (regardless of the sign of M and A): this flow corresponds to a pusher swimmer similar to that of flagellated bacteria. Preliminary results show that this property holds for a larger class of anti-symmetric surface property distributions.

1.5.3 Self-propulsion of isotropic autophoretic particles

The asymmetry of Janus colloids chemical properties ensure their swimming motion as they explicitly break the right/left symmetry at their surface's property level. Given the small size of such colloids, high-

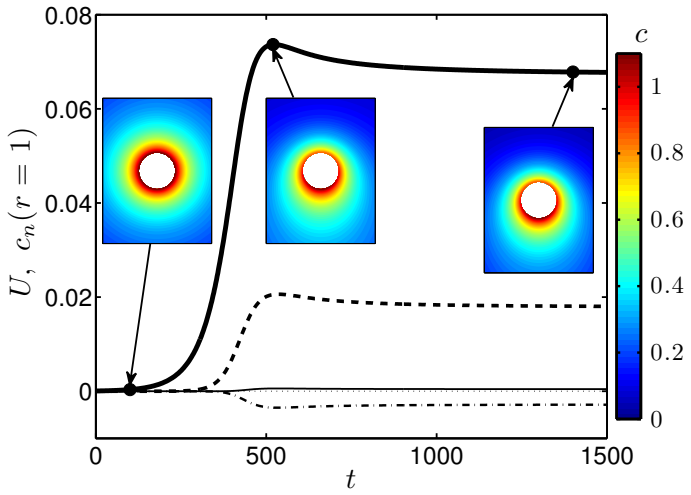

Figure 1.14: Evolution in time of the swimming velocity and next three moments of the solute surface concentration for $\mathrm{Pe} = 6$. Here the problem is started from rest with a nearly isotropic distribution of solute.

throughput manufacturing of such particles is however difficult. Here, I present our recent results showing that such a chemical anisotropy is not necessary for locomotion. For an isotropic particle (with a uniform emission/absorption activity $\mathcal{A}$), the trivial non-swimming and isotropic solution ($C_0 = C_\infty + A/r$ and $U = 0$) is always a solution, at all Pe. This work shows that above a critical particle size (or Pe), a supercritical transition takes place at which symmetry-breaking occurs through the non-linear coupling of solute concentration and phoretic flows.

Indeed, when started from rest from the isotropic solution, a small anisotropic perturbation in the solute leads to an exponential increase of the swimming velocity when $\mathrm{Pe} \geq 4$ (Figure 1.14). When a finite amplitude is reached, saturation is achieved through the non-linear interplay of the different squirming modes and the system converges toward a new steady state that corresponds to a net swimming velocity and a polar distribution of the solute around the colloid.

These results are confirmed analytically by considering the linear stability of the isotropic solution. The non-dimensional growth rate σ of the unstable swimming mode is found implicitly in terms of Pe as (see Michelin *et al.*, 2013):

$$\mathrm{Pe}AM = \frac{12\sigma\mathrm{Pe} + 24\sqrt{\sigma\mathrm{Pe}} + 24}{\sigma^2\mathrm{Pe}^2 \displaystyle\int_{\sqrt{\sigma\mathrm{Pe}}}^{\infty} \left(\frac{\exp\left[\sqrt{\sigma\mathrm{Pe}} - t\right]}{t} \right) \mathrm{d}t + 6 + \sigma\mathrm{Pe} - (\sigma\mathrm{Pe})^{3/2} - 2\sqrt{\sigma\mathrm{Pe}}}. \tag{1.34}$$

The right-hand side of the previous equation is always greater than 4 for positive σ: this therefore confirms that an unstable solution exists, but only for $\mathrm{Pe} \geq 4$ and $AM > 0$. This latter constraint restricts the instability to two (out of four) configurations: to self-propel, isotropic colloids must release (resp. absorb) solute particles with repulsive (resp. attractive) interactions with the surface of the colloid. This linear analysis can be repeated for each of the squirming modes (or moment of the surface solute concentration), and a series of instabilities are identified for quantized Pe numbers: for $\mathrm{Pe} > \mathrm{Pe}_n = 4(n+1)$, the n-th squirming mode becomes unstable (for $n \geq 2$) (see Figure 1.15).

Using full non-linear numerical simulations, we are able to determine the new steady-state of the colloid and its swimming velocity, stresslet, etc... (Figure 1.15), confirming the supercritical nature of the instability at $\mathrm{Pe} = 4$. Note that the steady-state solution above $\mathrm{Pe} = 4$ includes components along each squirming

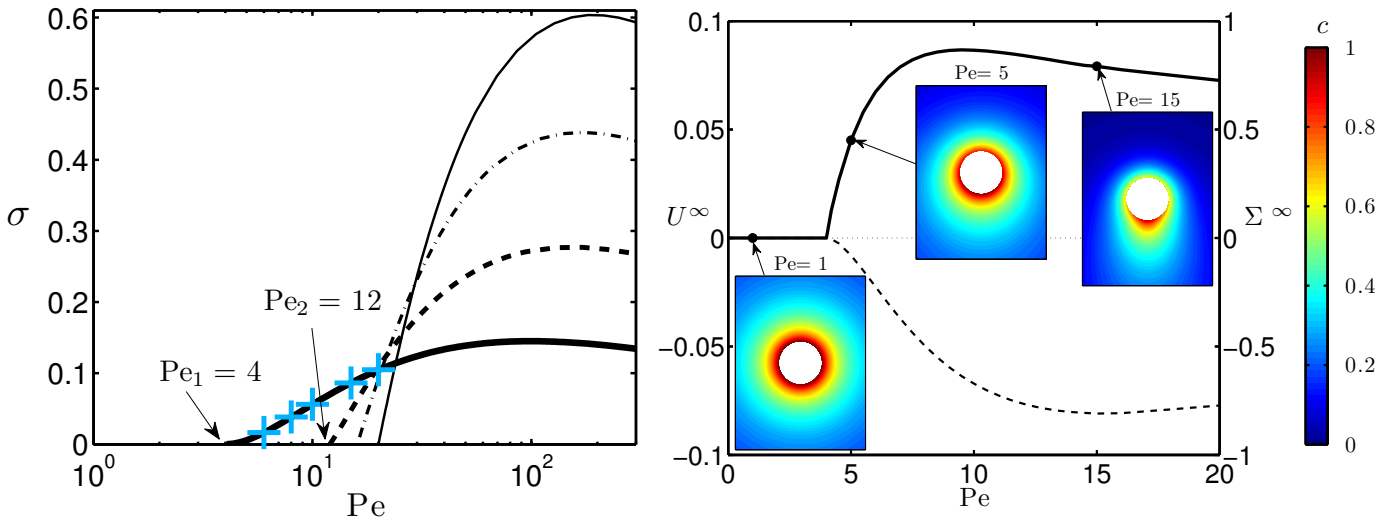

Figure 1.15: (Left) Evolution with Pe of the growthrate of the unstable swimming mode (thick solid) and higher order unstable squirming modes: $n = 2$ (dashed), $n = 3$ (dash-dotted) and $n = 4$ (thin solid). Quantized critical Péclet number are identified for each squirming mode: $\mathrm{Pe}_1 = 4$ and $\mathrm{Pe}_n = 4(n+1)$ for $n \geq 2$. Blue crosses show the results from non-linear simulations in time of the phoretic problem. (Right) Evolution with Pe of the swimming velocity and stresslet associated with the steady-state swimming solution. The solute distribution around the particle is represented for typical cases.

modes (despite them being stable for $\mathrm{Pe} \leq \mathrm{Pe}_n$): this emphasizes the nonlinear nature of the steady-state solution which couples all the azimuthal components of the velocity and solute concentration fields.

This establishes the possibility for spontaneous locomotion of isotropic auto-phoretic particles. For the type of surface treatment used experimentally for Janus colloids, the critical size is estimated to be about 100μm, but could be reduced by the use of a different solute with a smaller diffusivity. This mechanism is reminiscent of the instability of reactive non-Brownian droplets leading to their net locomotion (Thutupalli *et al.*, 2011; Yoshinaga *et al.*, 2012). In their experiment, a bromine water droplet is placed in an oil background phase containing a surfactant that can be brominated at the water-oil interface leading to a reduced surface tension; the resulting Marangoni stresses are then responsible for the tangential velocities and the propulsion. The similarity between those two problems suggests that they could be treated in a unified framework (see for example Anderson, 1989; Ruckenstein, 1981).

1.6 Ongoing work and perspectives

Auto-phoretic particles represent a particularly interesting problem, both from a fundamental point of view and from the perspective of possible applications. They represent a promising alternative to currently engineered micro-robots and do not rely on externally-applied fields. Such a fuel-based approach is particularly interesting if the chemical mechanism is relatively simple and relies on chemical species already present in the environment considered. From a fundamental perspective, we benefit from research carried out over the past decades on electrophoresis, diffusiophoresis and thermophoresis in the case of externally-imposed gradients, which provides a good fundamental understanding of the mechanisms involved. However, several questions remain open, which I would like to be able to address in the coming years:

– *What happens when the diffuse layer is not thin?*
Most studies consider only the case where the diffuse layer is so thin that all phoretic effects can be bundled into the formation of a slip velocity *at the solid's surface*. Understanding the validity of this assumption is essential, as well as determining the effect of first-order corrections on the dynamics of the colloid. Some recent studies have provided some elements in the pure diffusive limit (Pe $\to 0$, see Sabass & Seifert, 2012*a*; Sharifi-Mood *et al.*, 2013), and a particular attention should be given to the effect of Pe.

– *Swimming vs. pumping*
As illustrated by the omni-presence of cilia in a large variety of functions in our own organism, locomotion problems also have implications for pumping (e.g. mucus flows in our respiratory system generated by the flapping cilia). The results presented here suggest that non-linear advective effects can lead to a symmetry-breaking event and self-propulsion, and it is therefore natural to question the possibility to use such a transition as a pumping mechanism in artificial channels with chemically-reacting walls. If such a pumping mechanism can be designed, its efficiency should also be characterized.

– *How does a self-propelled auto-phoretic particle interact with an external gradient?*
Although this may be seen as a simple combination of both the classical phoretic and the autophoretic problems, it is essential to be able to understand the dynamics of a self-propelled particle in non-uniform solutions, and to understand the effect of boundaries and other particles on its dynamics: indeed, confinement or other colloids will modify the local gradients seen by the particle of interest. Beyond a fundamental interest, understanding and quantifying the effect of this local gradient is a first step toward the study of chemical and/or hydrodynamic interactions of such systems.

– *What are the collective dynamics of such particles?*
This is a direct continuation of the previous problem, and is probably one of the most important challenges in the field as such artificial swimmers are likely to be produced not as single individuals but as large, and maybe concentrated, populations. Understanding the collective dynamics is therefore important to identify possible organized states or transitions to chaotic motion, and to quantify the impact on macroscopic quantities such as mixing of the background solution. The results presented above suggested a very strong influence of the size of the particles (through Pe) on their propulsive properties, and it remains to be studied what consequences this may have on the properties of a suspension of such colloids.

– *What are the similarities and differences between such artificial swimmers and suspensions of real micro-organisms?*
This research on artificial micro-swimmers needs to be closely linked to existing and future research efforts to understand the individual and collective dynamics of real micro-organisms, and this parallel study will be one of the main axes of my research in the coming years. Swimming micro-organisms are influenced by a large number of environmental factors and are able to respond to them. From a mechanical point of view, this response can be either passive (e.g. gravitational torque induced on swimmer with non-uniform buoyancy leading them to swim upwards, see Pedley & Kessler, 1992) or active (e.g. modification of the run-and-tumble motion of *E. Coli* in response to a chemical species concentration to enable chemotaxis, see Berg, 2004). In comparison, the response of artificial micro-swimmers is likely to be purely passive (from a mechanical point of view) to ensure the simplicity of their design. An interesting question is therefore to characterize the behavior of such artificial swimmers in the light of known behaviors and properties of natural swimmers (e.g. bioconvection, see Pedley & Kessler, 1992).

Chapter 2

Fluid-solid instabilities and energy harvesting in high-Re flows

2.1 Introduction

The previous chapter focused on locomotion problems in low-Re flows where viscous effects dominate the fluid forces. In contrast, this chapter focuses on fluid-solid instabilities at high Re, where inertial and pressure forces dominate outside of thin boundary layers. These two chapters not only differ in the flow regime considered, but also through the type of fluid-solid interactions. Unlike locomotion, for which a forcing (mechanical or chemical) is applied by the solid system on the fluid, we focus here on situations where the solid motion develops spontaneously under the destabilizing effect of a steady flow forcing.

Hence, both problems (locomotion and instabilities) fundamentally differ in the direction of the energy flux: in the locomotion problem (for high or low Re), the solid system transfers energy to the fluid in order to propel itself, and the energy is dissipated through viscous effects or advected away in the wake of the organism. In this chapter, the energy transfer is reversed: the structure extracts from the steady incoming flow the energy necessary for its vibrations, which develop spontaneously under the effect of the fluid-solid instability. Hence, a fluid-solid instability can be seen as an "energy pump" or a mechanism that enables the solid to extract a fraction of the incoming flow's kinetic energy. In the permanent regime, an energy balance is established between locations or mechanisms that extract energy from the fluid to maintain the solid motion and those returning part of this energy to the fluid, for example in the form of a vortex wake. The net energy budget can either be neutral (if no dissipation is present in the structure) or directed toward the solid if any kind of structural damping or energy extraction mechanism is present. This is, in essence, the main idea and motivation of the work presented in this chapter: a fluid-solid instability, and the associated permanent flapping or vibrating regime, can be used as an energy extraction mechanism if one is able to include a device in the system to convert a fraction of the solid mechanical energy into electricity. Then the solid system only acts as a vector to transfer energy from the fluid to an electrical output circuit.

2.1.1 Fluid-solid instabilities: a new energy harvesting mechanism?

The limited availability and environmental impact of fossil fuels currently motivates a significant research effort about the development and diversification of renewable energy production technologies. Geophysical flows represent an attractive reservoir of energy present and accessible throughout the world, in the form of winds, river, oceanic and/or tidal currents. Most, if not all, operating devices producing electricity from a fluid flow rely on the horizontal-axis wind- and water-turbine concept: the lift forces on the turbine blades generate a net torque that is used to drive an electromagnetic generator. The energy density in such flows is

however rather low (the kinetic energy flux is typically of the order of 1–10kW/m^2) which makes it difficult to replace a conventional power-plant, unless very large systems are used, with a non-negligeable environmental impact. This limitation is intrinsic to the energy source (geophysical flows) and will therefore exist regardless of the extraction mechanism considered. A different approach consists in encouraging the development of small-scale power units that are ill-suited for a connection to a classic grid, but can be used to power isolated or mobile devices. Turbine technologies are quite inefficient at such reduced scales (in particular in terms of operating flow velocities), and a critical research and development challenge of the next ten years will be to design and develop new prototypes to harvest energy from fluid flows.

In that regard, and as emphasized above, fluid-solid instabilities are promising candidates: by promoting spontaneous and self-sustained solid motion, they can be used to passively extract fluid kinetic energy in the form of solid kinetic or deformation (e.g. elastic) energy that can be harvested using classical electromagnetic or piezoelectric systems. In recent years, several designs based on such fluid-solid couplings have been proposed (see a brief review of early prototypes in Westwood, 2004): to name only a few, the VIVACE design (Bernitsas *et al.*, 2008) is based on the Vortex-Induced Vibrations (VIV) of rigid cylinders in cross flow (Williamson & Govardhan, 2004) and the STINGRAY (or wind-mill) on the coupled-mode flutter of a rigid heaving and pitching airfoil (Zhu & Peng, 2009; Peng & Zhu, 2009; Zhu, 2012). The flapping of an elastic sheet in the unsteady wake of a rigid cylinder is at the core of the energy harvesting eel design, where electric power is obtained through the deformation of the thin piezoelectric sheet (Allen & Smits, 2001; Techet *et al.*, 2002): although not technically a fluid-solid instability (the flow upstream of the sheet is unsteady), this particular geometry has motivated a significant part of my research (Doaré & Michelin, 2011; Singh *et al.*, 2012*b*,*a*; Michelin & Doaré, 2012), as well as other authors' over the last five years (Tang & Païdoussis, 2009; Giacomello & Porfiri, 2011; Akcabay & Young, 2012), in particular because this system illustrated a way to convert deformation of a thin flapping sheet into electricity rather than relying exclusively on electromagnetic generators as for other prototypes.

This application of classical fluid-solid instabilities and coupling mechanisms to energy harvesting represents an original point of view on such problems: in the past, such instabilities have always been considered as a nuisance, if not a danger, for the integrity of the structure, since the resulting vibrations may generate fatigue and damage. Most of the existing research on these mechanisms is therefore motivated by the identification of the instability in order to avoid or control its development. VIV research was for instance largely motivated and supported by the need to control the vibrations of cables and risers exposed to oceanic currents in offshore applications (e.g. oil platforms). From that point of view, it is not surprising that the majority of the existing literature on such fluid-solid couplings focus on linear analysis: one is interested in minimizing the amplitude of the vibrations. Applying such concepts to energy harvesting is a new twist on these problems, as the vibrations are now seen as a benefit that should be enhanced, and large amplitude cycles are sought. This, in return, requires a thorough understanding of the nonlinear phenomena responsible for the saturation of the vibrations and the development of the permanent regime. This is clearly one of the main challenges of this research topic: while the fundamental mechanisms responsible for the motion of the solid body have been well-known for a long time, the non-linear dynamics of these systems and their sensitivity to operating conditions (e.g. flow velocity) or even to the energy extraction mechanism, remains in most instances to be understood. Aside from the fundamental interest of such understanding, it is also crucial to be able to assess properly the energy efficiency of such systems as well as to identify some possible optimization strategies.

This chapter is organized around two main geometries: (i) the Vortex-Induced Vibrations of a rigid cylinder or of a long flexible cable in cross flows and (ii) the flutter dynamics of a flexible slender body (e.g. a flag) in axial flows. While the formalism and models may differ significantly for these applications, several fundamental questions are common to both problems and are presented below in more detail.

2.1.2 Outline and transverse questions

Regardless of the geometry considered, the research presented in this chapter is motivated by the following transverse questions:

(a) What is the impact of the harvesting system on its dynamics and efficiency, and how can it be modeled?

(b) What is the operating range of the system and how may it be improved?

(c) What is the efficiency of the system and how may it be improved?

When designing an energy harvester, the main concern is to seek the maximum energy output, corresponding to a significant energy loss for the fluid-solid system, which is likely to modify its dynamics. Most existing research on the linear stability or the non-linear dynamics of the fluid-solid system is dedicated to purely non-dissipative configurations or weakly damped systems (e.g. to account for energy losses due to friction). In these cases, damping is either absent or a small parameter. Here, it is necessary to understand what happens when the extracted energy is not small. In model experiments or numerical studies, a related issue is therefore to include this effect in the fluid-solid dynamics. Because energy harvesting effectively amounts to a loss of energy from the solid, the crudest but most natural model is that of pure damping (Peng & Zhu, 2009; Tang & Païdoussis, 2009; Zhu & Peng, 2009). The advantage of this model is to propose a simple way to quantify how much energy can be harvested (or dissipated) in a particular fluid-solid system, while capturing the main physical process: the loss of energy by the solid structure.

Using this representation, it is then easier to grasp why it is essential to take into account the harvesting process in any model. In the small-damping limit, the fluid-solid dynamics is similar to the non-dissipative case, but the harvested (dissipated) energy is small. To achieve higher efficiency, damping should be increased and its effect will then impact the dynamics of the system. Intuitively, when damping is too large, the vibration amplitude is reduced and the system's efficiency is penalized: the fraction of the solid energy that is extracted is still high but the available solid energy is very limited. There exists therefore an optimal range of damping and to understand or capture the dynamics in that regime, the effect of damping on the fluid-solid system must be well-understood.

Damping and energy harvesting may influence the system in many ways other than just through its vibration amplitude. Damping may also modify the range of instability leading to energy harvesting: for large damping amplitudes, it is expected that the system will restabilize since the energy cost of motion is too high compared to the energy available through the instability. However, damping may also destabilize the system (Paidoussis, 2004; Doaré & Michelin, 2011), thereby increasing the operating range of the device. Also, when multiple vibration modes are possible, varying the damping intensity may lead to mode switches that will change the flapping shape of the structure, and its frequency and amplitude, thereby impacting the energy harvesting efficiency.

The linear framework is therefore essential to characterize *when the fluid-solid system can harvest energy*. This framework is however limited in its inability to characterize the long term behavior of the system and in particular the amplitude, shape and frequency of limit-cycle oscillations that develop when the growth of the instability saturates. It is therefore inefficient in determining the performance of the system and to be able to assess *how much energy can be harvested*, we will need to turn to a non-linear approach that is able to predict the saturation of the vibration and the limit-cycle dynamics.

How much energy can be harvested with such a system is clearly linked to its size, and more than the dimensional value of the harvested power, it is important to rely on non-dimensional analysis to establish scaling laws for the harvested power in terms of the system's size and operating conditions. One way to do this is through the non-dimensional harvested power (see for example Singh *et al.*, 2012*a*,*b*; Akcabay & Young, 2012):

$$\mathcal{P} = \frac{\langle \mathscr{P} \rangle}{\rho_f U_\infty^3 L^2} \tag{2.1}$$

where $\mathscr{P}(t)$ is the instantaneous power extraction, U_∞ the incoming flow velocity and L a typical dimension of the structure (e.g. the diameter of the cable, the length of the flag). Another possible measure of the system's performance is the fraction of the kinetic energy flux that is actually harvested:

$$\eta = \frac{\langle \mathscr{P} \rangle}{\frac{1}{2}\rho_f U_\infty^3 \mathscr{S}} \tag{2.2}$$

with $\mathscr{S}$ the typical cross-section occupied by the device in the flow. The main advantage of this formulation rather than the non-dimensionalization Eq. (2.1) is its similarity to the benchmark efficiency definition of a classical wind-turbine (a scaling of the harvested power by the kinetic energy flux through the turbine disk), thereby enabling comparisons between the performance of different devices. In particular, one may be interested in exploring the existence of an equivalent to the Betz limit for horizontal-axis turbines. Scaling the energy production by the cross-section occupied by the device in the flow is also relevant when trying to estimate the efficiency of multiple devices in parallel, although, as will be discussed later, this completely overlooks any hydrodynamic interactions between the neighboring devices. The main caveat of this formulation is however that it relies on a clear definition of $\mathscr{S}$ which is not always achievable or that may be disputable as it may involve the flapping amplitude of the device, itself a result of the problem.

Other formulations have also been proposed in the literature, including a scaling of the harvested energy by the peak kinetic energy of the solid (Dunnmon *et al.*, 2011) or the mean energy of the solid over a period (Doaré & Michelin, 2011; Akcabay & Young, 2012). Such formulations which amount to a conversion efficiency may be useful in a linear setting (Doaré & Michelin, 2011), as it does not depend on the flapping amplitude of the solid. But this choice of normalization is ill-suited when looking for the limit-cycle efficiency as the reference power scale does not correspond to an input power in permanent regime.

These considerations illustrate the difficulty of defining the harvesting efficiency in a clear and unique fashion. It also emphasizes how the numeric value of the efficiency is fundamentally linked to its definition and this number only has a meaning in a particular context and definition. In the following, the chosen definition differs slightly from one problem to the other, but will be clearly stated to avoid any confusion.

The rest of the chapter is organized as follows: Section 2.2 focuses on the Vortex-Induced Vibrations of rigid cylinders and tensioned cables and corresponds to the PhD of Clément Grouthier. Sections 2.3 and 2.4 focus on the flapping instability of flexible plates and cylinders in axial flows and their application to energy harvesting. Section 2.3 focuses more specifically on the fundamentals of the flag instability and the impact of damping on the nonlinear flapping, while Section 2.4 presents a full fluid-solid-electric model for which the electric power production is represented using piezoelectric patches positioned on the flag. Finally, the conclusions of this chapter as well as some perspectives and the presentation of ongoing work will be detailed in Section 2.5.

2.2 Vortex-Induced Vibrations and energy harvesting

2.2.1 Vortex-Induced Vibrations of rigid cylinders and cables

Vortex-Induced Vibrations (VIV) are a canonical example of fluid-solid couplings that has applications in a large variety of fundamental and applied problems. They may be responsible for the vibrations of heat-exchanger tubes in a nuclear reactor or the vibrations of anchor cables or risers in offshore oil rigs. Physically, VIV are intimately linked to the instability of the wake behind a bluff body. Above a critical Reynolds number ($\mathrm{Re} \approx 47$ for a fixed cylinder), the separated flow becomes globally unstable, leading to an unsteady and periodic vortex shedding behind the structure, the so-called Von-Karman vortex street, at a fixed frequency, the Strouhal frequency:

$$\Omega_f = 2\pi S_T \frac{U}{D} \tag{2.3}$$

with U and D the flow velocity and structure's diameter, respectively, and S_T the Strouhal number (Blevins, 1990). Such a flow results in unsteady and periodic flow forces on the obstacle, leading to its vibration. When the flow velocity, or Re, is further increased, the flow may become turbulent and the organized vortex street pattern be lost; the unsteadiness of the flow and fluid forces however remain, and are characterized by a dominant frequency that still follows the same Strouhal law, Eq. (2.3). The Strouhal number itself is a function of Re (Williamson & Brown, 1998). In the limit of high-Re, this dependence is rather weak, which justifies the general approach of considering it a constant $S_T \approx 0.2$.

The free or imposed vibration of an obstacle is also going to influence the vortex shedding mechanisms (see for example Bearman, 1984; Williamson & Roshko, 1988), and in particular, it may lead to a deviation of the shedding frequency from the Strouhal law when the forcing frequency is close to the natural frequency of the wake. This phenomenon, known as lock-in, is one of the most distinguishing features of the free vibrations of a bluff body under the influence of its oscillating wake: when the natural vibration frequency of the body and the natural frequency of the wake are far apart, shedding and vibrations occur at the same Strouhal frequency and the amplitudes of vibrations are only limited (the solid is forced at a frequency far from resonance). However, when those frequencies are close enough, the two-way coupling between vortex shedding and solid vibrations leads to a lock-in of the shedding frequency on the natural frequency of the body, leading to a significant increase of vibration amplitude, typically of the order of the diameter of the structure (Williamson & Govardhan, 2004).

When the bluff body is free to move in both the streamwise and cross-flow directions, vibrations can occur in both directions, and the streamwise forcing and motion then have a frequency of twice that of their cross-flow counterparts. In general, however, the amplitude of the cross-flow vibrations is dominant and in the following we will focus for simplicity only on cross-flow vibrations, keeping in mind that vibrations can and may also occur in the direction of the stream with smaller amplitudes.

In the presentation above, VIV were linked to the instability of the wake forcing the motion of the cylinder. An alternate point of view is also possible, in which VIV are considered as the result of a fluid-solid instability (Cossu & Morino, 2000; de Langre, 2006). In particular, the critical Re leading to an unsteady wake is reduced for a free cylinder in comparison with the classical fixed obstacle configuration (Cossu & Morino, 2000; Meliga & Chomaz, 2011). Following de Langre (2006), vortex-induced vibrations and lock-in can be interpreted as a coupled-mode flutter instability, where the linear coupling of a wake mode to a structure mode leads to the instability.

2.2.2 Modeling the non-linear coupled dynamics: the wake-oscillator model

Although weakly nonlinear analytical studies of the flow around the free moving cylinder have been proposed near the critical Re using asymptotic expansion (Meliga & Chomaz, 2011; Meliga *et al.*, 2011), such a regime is only valid in a narrow window at flow velocities that are far beyond the Reynolds number corresponding to practical situations which ranges from 10^4 to 10^6 from underwater cables to spars placed in typical oceanic currents. Most phenomenological properties of VIV have therefore been obtained experimentally or numerically (see Williamson & Govardhan, 2004, and references therein). Direct numerical simulations of the VIV phenomena are possible but computationally expensive, particularly in 3D settings (e.g. Newman & Karniadakis, 1997; Bourguet *et al.*, 2011).

For a rigid 2D cylinder in cross-flow motion, the dynamics can be represented by a simple forced oscillator

$$M\ddot{y} + r\dot{y} + hy = F_L(y(t), t) \tag{2.4}$$

where M is the mass of the cylinder, h the spring stiffness, r the damping intensity, and F_L the fluctuating lift. The different models for the fluctuating lift can be decomposed with an increasing level of complexity and physical completeness, into (i) forced system models, (ii) fluidelastic system models and (iii) coupled models (Paidoussis *et al.*, 2010). Type (i) includes a fluid forcing that does not depend on the solid motion

while types (ii) and (iii) introduce a coupling between the solid motion and the fluid forcing. In type (ii), this dependence is explicit (the fluid force is a direct function of the solid velocity and acceleration) while in type (iii), the solid motion acts as a forcing on the intrinsic dynamics of the wake and flow forces. A popular model of this type is the *wake-oscillator* approach: this idea, introduced more than 50 years ago, describes the unsteady intrinsic dynamics of the wake using an oscillator equation for the lift coefficient forced by the cylinder motion (Birkhoff & Zarentello, 1957; Bishop & Hassan, 1964; Hartlen & Curie, 1970). The advantage of this formulation is that most of the free parameters determining the oscillator's dynamics can be determined experimentally for a fixed cylinder and then applied to VIV by coupling this oscillator (typically a van der Pol or Rayleigh equation) to the solid's dynamics (see Parkinson, 1989, and references therein).

More recently, Facchinetti *et al.* (2004*a*) analyzed and determined the most appropriate form for the forcing of the cylinder motion on the wake-oscillator's dynamics and concluded that an inertia force coupling allowed the best reproduction of classical features of lock-in:

$$\ddot{q} + \epsilon\Omega_f(q^2 - 1)\dot{q} + \Omega_f^2 = \Omega_f^2 A\ddot{y} \tag{2.5}$$

with $q = 2C_L/C_{L_0}$ the reduced-lift coefficient (with C_{L_0} the lift coefficient observed on a fixed rigid cylinder), and A and ϵ two non-dimensional parameters that were fitted to match experimental observations. In this model, the fluid force F_L in Eq. (2.4) is decomposed into an added mass force, a stall force, and a lift force, the unsteady wake forcing being related only to the latter:

$$F_L(t) = -M_f\ddot{y} - \gamma\rho\Omega_f D^2 L\dot{y} + \frac{1}{2}\rho U^2 DLC_L(t) \tag{2.6}$$

with $M_f = \pi\rho D^2 L/4$ and γ the added mass and stall coefficient respectively, and L the length of the cylinder. The obvious advantage of this model resides in its simplicity while still retaining the main features of the unsteady wake and the coupled vibrations. It was later used to study vortex waves along cables (Facchinetti *et al.*, 2004*b*; Mathelin & de Langre, 2005; Violette *et al.*, 2010) and compared to direct numerical simulations and experiments (Violette *et al.*, 2007).

In the following, this model will be successively used to study the VIV of a rigid cylinder and of a tensioned cable from which energy is extracted through a damping system.

2.2.3 Energy harvesting by a rigid cylinder

The motion of the solid body resulting from VIV is significant, particularly at lock-in where it reaches the order of a diameter. Producing an electric current with a generator forced by this motion is at the core of the VIVACE design, initally proposed by Bernitsas *et al.* (2008), which has received growing attention in recent years (see also the work of Yoshitake *et al.*, 2004; Barrero-Gil *et al.*, 2012).

A simple damping model is used to represent the effect of energy harvesting on the system's dynamics and to quantify how much energy can be extracted from the VIV of a rigid cylinder (Figure 2.1a). In the following, we neglect any internal damping of the structure other than the energy harvesting process so that the total harvested power can be defined from Eq. (2.4) as $\langle r\dot{y}^2 \rangle$, and in non-dimensional form

$$\eta = \frac{\langle r\dot{y}^2 \rangle}{\frac{1}{2}\rho U^3 DL}. \tag{2.7}$$

In the following, we will refer to this quantity as the system's efficiency to follow the terminology in Bernitsas *et al.* (2008), although strictly speaking, the effective cross-section used is that of the fixed cylinder rather than that occupied by the moving system (see the discussion in Section 2.1.2). Figure 2.2 shows the evolution of this efficiency, in permanent regime, with the frequency ratio $\delta = \Omega_s/\Omega_f$ and damping

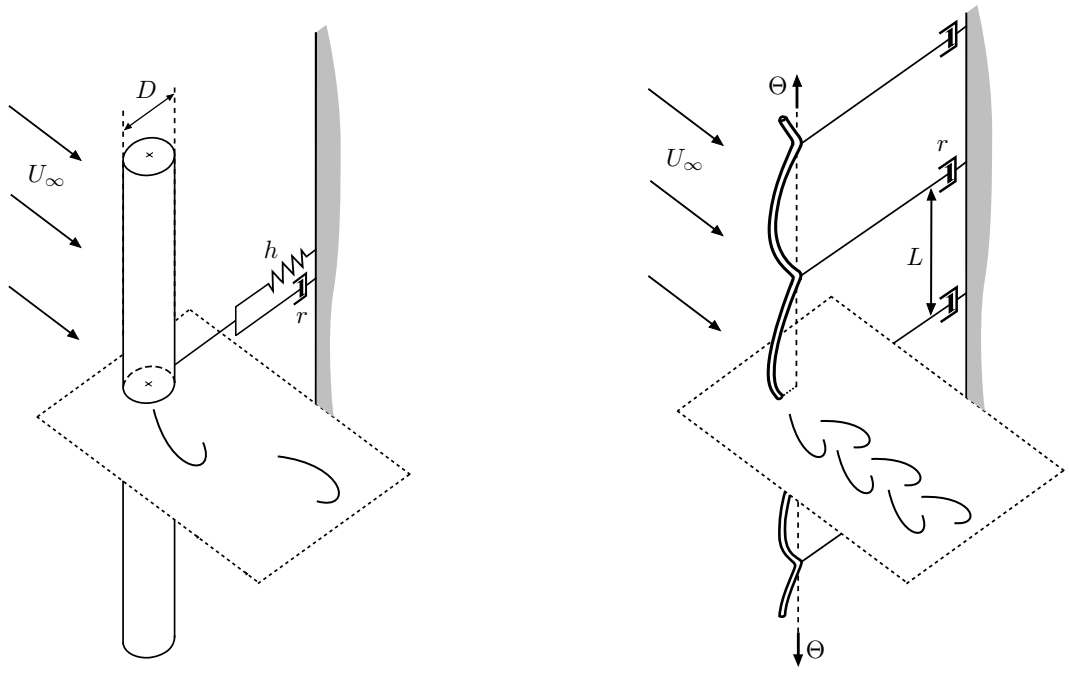

(a) Rigid cylinder (b) Tensioned cable

Figure 2.1: (a) Vortex-Induced vibrations of a rigid cylinder in a cross-flow harvesting energy through a displacement-based damping system. (b) Vortex-Induced Vibrations of a long tensioned cable with periodically-distributed energy harvesters.

coefficienty $\xi = r/\Omega_f(M + M_f)$, with Ω_f the Strouhal frequency and Ω_s the fundamental frequency of the immersed cylinder (linked to its stiffness). A clear optimal configuration is identified corresponding to a peak efficiency of 0.23 which is close to the efficiency reported by Bernitsas *et al.* (2008) on the VIVACE system.

For a fixed stiffness δ, the variations of η with damping follow the qualitative trend outlined in Section 2.1.2: at low damping values, the harvested energy is low as only a small fraction of the solid's mechanical energy is actually extracted, while the harvested energy is also limited at very large damping, because of the resulting reduction of the vibration amplitude by the damping effect. For each value of δ, there is therefore an optimal damping ξ_{opt} for which the harvested energy is maximum.

For a fixed damping intensity, there also exists an optimal stiffness $\delta \approx 1$ which corresponds to a lock-in of the wake and solid natural frequencies. The optimal value is in fact $\delta = 0.89$ which emphasizes once again that high amplitude oscillations can be reached over a range of velocity (or equivalently a range of stiffness) values around the perfect tuning of the two systems.

2.2.4 Periodic energy harvesting on a long cable

A rigid VIV system however presents some important limitations, the main one being that it is only applicable to rather short systems. Due to the weak density of energy in geophysical flows, it might be interesting to design a long system that is necessarily going to have some flexibility. While it is less critical for a rigid system since all points along the structure have the same displacement, the question of the positioning of the generator becomes essential in a long flexible structure. The underlying question is of course that of the transport of energy along the cable toward the generator where it can be converted.

The dynamics of a cable in VIV differ from that of a rigid cylinder mostly in the existence of a large

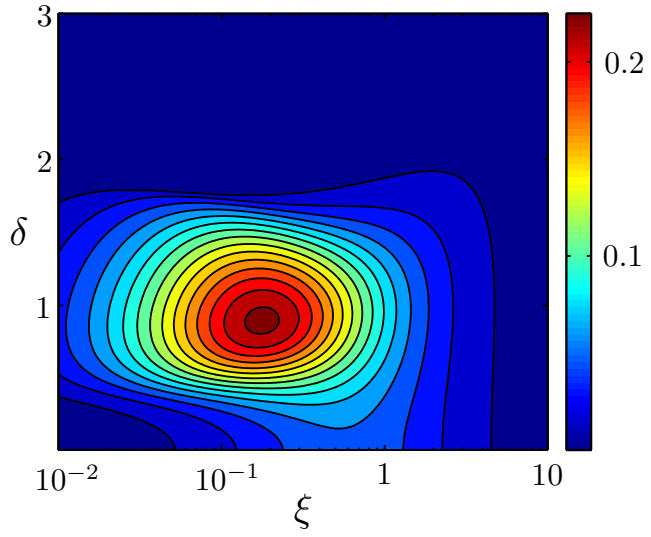

Figure 2.2: Energy harvested by a rigid cylinder in VIV (see Figure 2.1, left) as a function of the non-dimensional damping ξ and stiffness δ.

number of fundamental vibration modes for the structures, which may lock in to the shedding frequency over different ranges of velocity. Essentially, above a certain flow velocity the system is always at lock-in.

To get some physical insight on that problem, we present here some results on a model system: an infinite tensioned cable with periodically distributed energy harvesters (represented here as linear dashpots, dissipating the energy associated with the translation of particular points along the cable, Figure 2.1b). The rigid body dynamics, Eq. (2.4), is now replaced by the following cable equation

$$m\ddot{y} + \gamma\rho\Omega_f D^2\dot{y} - (\Theta y')' = \frac{1}{2}\rho U^2 D^2 C_L(t), \tag{2.8}$$

where primes denote differentiation along the vertical axis coordinate z. We neglect here any bending rigidity within the structure. The cable's tension drives the motion of each dashpot (located at $z_n = nL$), leading to the following boundary condition:

$$\Theta[y'(z_n^+) - y'(z_n^-)] = -r\dot{y}(z_n). \tag{2.9}$$

Two non-dimensional parameters characterize the system, namely the reduced damping $\xi = r/\Omega_f m$, with m the total lineic mass (solid and fluid added mass), and the reduced spacing $l = L\Omega_f\sqrt{m/\Theta}$. The latter essentially compares the generators' spacing to the typical wavelength of mechanical waves on the cable with frequency Ω_f.

The evolution of the efficiency η with ξ and l is shown in Figure 2.3. An optimal harvesting efficiency can again be identified around $\eta \approx 0.19$ which is of the same order, albeit slightly reduced, than the optimal efficiency of the rigid system. Its variations are however much more complex because of the existence of multiple modes for the cable dynamics. The presence of different lobes are indeed associated with different dominant linear modes. The left side of the diagram (low damping) is characterized by a low harvesting efficiency and corresponds to dominant even modes, leading to a weak forcing on the generator. On the right (high damping), regions of low efficiency associated with even modes alternate with efficient regimes associated with odd vibrations modes, corresponding to a strong forcing on the generator. Finally, the lower part of the diagram, where the optimal configuration lies, corresponds to a wavelength of the deformation greater than L: the deformation of the cable is weak and resembles that of a rigid cylinder.

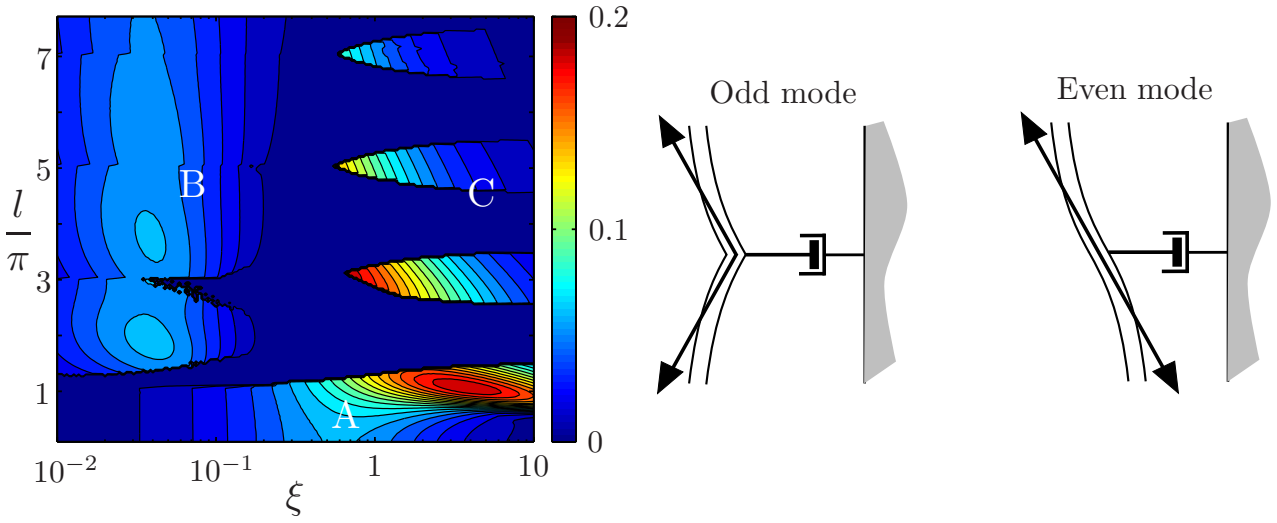

Figure 2.3: (Left) Energy harvested by a tensioned cable in VIV with periodically-distributed energy harvesters (see Figure 2.1, right), as a function of the non-dimensional damping ξ and wavelength l/π. Three regions of the parameter space can be identified depending on the cable dynamics (see text). (Right) Orientation of the tension forces exerted by the cable on the harvesting generator in odd and even modes of the cable.

From these observations, we conclude that (i) the flexible case presents a similar optimal efficiency to the rigid cylinder and (ii) that its efficiency is however much more sensitive to the intensity of damping and to the system's stiffness (here represented by l): this sensitivity illustrates the important impact of the energy harvesting system on the fluid-solid system's dynamics, here by selecting the vibration mode. Although optimal, the lowest order mode is not the only one producing energy, and in fact similar efficiency can be achieved (albeit in a narrow region) by the next odd mode. For higher-order odd modes however, Figure 2.3 illustrates that large spacing between the generators penalizes the efficiency of the system: only a bounded effective length of cable contributes to the energy harvested at the generators, the rest of the energy being dissipated by the fluid damping during its transport.

The present system has a fixed tension. An alternative would be to consider a drag-induced tension for which Θ is determined by the flow velocity (see Grouthier *et al.*, 2012). This could be achieved either through the deformation (extension) of the mean cable position in the streamwise direction due to the flow or through the drag exerted on a solid structure attached to the cable. This new approach does not modify the optimal efficiency of the system, however it strongly reduces its sensitivity to the flow velocity, in comparison with the fixed-tension cable or even the rigid cylinder (Figure 2.4). This passive control strategy for the system's tension is a first step in optimizing the robustness of the device to varying flow conditions.

The results presented above confirm the possibility to harvest energy from VIV of either rigid structures or long flexible cables. The latter configuration may be of particular interest for offshore applications (localization of the generator on a long system). These results however emphasize the existence of a maximum distance over which the energy can not be transported by the cable anymore which introduces a fundamental limit on a single-point harvesting configuration. To extend and confront these results to experiments, the last year of the PhD of Clément Grouthier is currently dedicated to experiments on hanging chains and tensioned strings with localized damping to represent the effect of the harvesting mechanism.

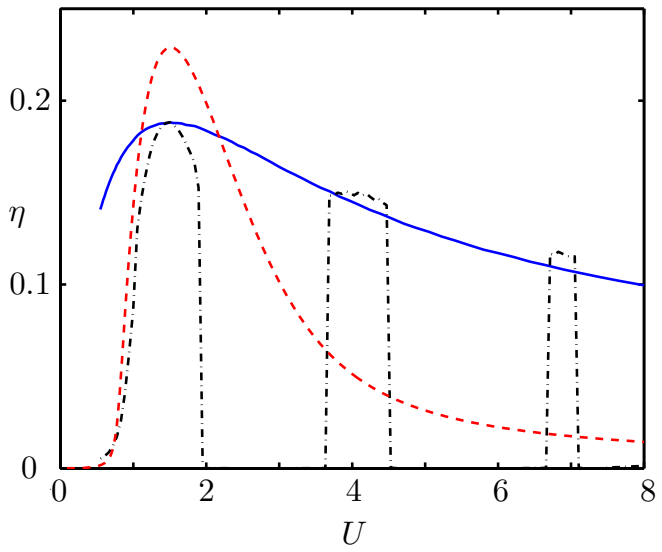

Figure 2.4: Comparison of the evolution of the energy harvesting efficiency with the flow velocity U for a rigid cylinder (dashed red), and cables with periodic harvesting and fixed tension (black) or drag-induced tension (blue). For the first two configurations, the rigidity and damping parameters are chosen so that the maximum efficiency is reached for the same velocity $\bar{U} = 1.5\text{m.s}^{-1}$. In the last case, the tension is induced by a drag on an effective surface A designed such that the tension in the system is equal to that of the fixed tension problem at $\bar{U}$.

2.3 The energy harvesting flag

This section and the following are dedicated to a fundamentally different type of fluid-solid instability, namely the flutter instability of a long flexible slender body in a steady axial flow. The theoretical understanding and numerical modeling of this instability in two-dimensional flow represent a significant part of my doctoral work (Michelin, 2009). Dedicated to the development of reduced-order inviscid models for fluid-solid interactions of flapping and falling bodies (Michelin & Llewellyn Smith, 2009*c*), it focused on several applications of the interaction of flapping flexible sheets with an incoming axial flow including the flapping flag instability itself (Michelin *et al.*, 2008; Michelin & Llewellyn Smith, 2009*a*, 2010) and flapping wing propulsion (Michelin & Llewellyn Smith, 2009*b*). Building on this experience, the research I have developed since arriving at LadHyX is dedicated to understanding the nonlinear processes and applications to the energy harvesting problem.

2.3.1 The flapping flag instability

The flapping of a flag in the wind, the flutter of paper sheets in high speed offset printers and the vibration of the soft palate responsible for snoring are all linked to the same fluid-solid instability, namely the flutter of a flexible slender body in an axial flow above a critical flow velocity. As illustrated above, this classical "flapping flag instability" finds applications in a wide variety of fundamental systems but also in important engineering (Watanabe *et al.*, 2002*a*,*b*) and biomedical applications (Huang, 1995; Balint & Lucey, 2005). The fundamental interest has been extended outside the classical fluid-solid communities by the work of Zhang *et al.* (2000) who performed two-dimensional experiments using a flapping filament in a soap film. Since then, many experimental studies (Lemaitre *et al.*, 2005; Shelley *et al.*, 2005; Jia *et al.*, 2007; Eloy *et al.*, 2008) have been performed to characterize the flapping dynamics in both the two-dimensional limit (a flag

with infinite span) or the slender body limit (long ribbons), and the reader is referred to Shelley & Zhang (2011) for a complete review of that problem.

The origin of the instability lies in the coupling of a plate's inertia to the destabilizing flow forces associated with the system's curvature and the stabilizing effect of the solid's bending rigidity. A critical flow velocity is generally identified above which the straight equilibrium position becomes unstable and flapping can develop in the form of traveling waves along the structure. When the flow velocity is increased further, non-periodic and chaotic flapping have been reported by some experimental (Abderrahmane *et al.*, 2012) and numerical studies (Connell & Yue, 2007; Michelin *et al.*, 2008). Linear stability analysis is a powerful tool that has been used extensively in this problem from the early work of Kornecki *et al.* (1976) to study the effect of confinement (Guo & Païdoussis, 2000; Doaré *et al.*, 2011), aspect ratio (Eloy *et al.*, 2007), or hydrodynamic interactions (Michelin & Llewellyn Smith, 2009*a*).

Nonlinear numerical simulations are difficult, given the large number of degrees of freedom for the motion of the flag and the strong coupling to the surrounding flow. One of the most complete two-dimensional studies can be found in the work of Connell & Yue (2007) which uses coupled fluid and solid solvers. Immersed boundary methods also provide a possible alternative (Zhu & Peskin, 2002; Zhu, 2007; Tian *et al.*, 2011), and with the development of computational capacity, three dimensional direct numerical simulations have been undertaken (Huang & Sung, 2010). Although, so far, the complexity of the flag deformation and vortex wake structures obtained in such computations make it difficult to analyze the fundamental effects of the spanwise deformation. Significant results were however obtained using simplified simulations based on potential flows, and a brief overview of such techniques will be given in Section 2.3.3.

Despite the large number of studies of this topic in the last decade, several important questions remain unanswered even in the two-dimensional problem, among which are the supercritical or subcritical nature of the transition and the behavior at high velocity. The former is intimately linked to the existence of a hysteresis cycle when varying the flow velocity around the instability threshold, which was reported in numerical (Connell & Yue, 2007; Alben & Shelley, 2008; Michelin *et al.*, 2008) and experimental studies (Zhang *et al.*, 2000; Shelley *et al.*, 2005; Eloy *et al.*, 2008). The recent work of Eloy *et al.* (2012) suggested that, experimentally, the subcritical nature of the transition could be due to or at least reinforced by the (small) initial spanwise bending that rigidifies and therefore stabilizes the sheet. Their weakly non-linear analyses also suggested that the nature of the transition may also be linked to the aspect ratio of the flag. The non-linear behavior of the flag, and in particular the possible transition at higher velocities to chaotic regimes, also remains to be fully characterized, despite the recent work by Abderrahmane *et al.* (2012).

Three non-dimensional parameters characterize the flag system:

$$M^* = \frac{\rho L H}{\rho_s}, \qquad U^* = U_\infty L \sqrt{\frac{\rho_s}{B}} \quad \text{and} \quad H^* = \frac{H}{L}. \tag{2.10}$$

In the previous equation, H and L are the width and length of the plate, ρ_s and B its inertia per unit length and its bending rigidity, and ρ and U_∞ denote the incoming flow density and velocity. M^* is the fluid-to-solid inertia ratio, H^* the aspect ratio of the structure and U^* is the ratio of the flow velocity to the phase speed of elastic waves on the structure. $H^* \ll 1$ (resp. $H^* \gg 1$) corresponds to the slender body (resp. two-dimensional) limit. Although we refer here to a flag, it is understood that the present results may also be applied to other cross-sections, in particular in the slender body limit to a slender cylinder of arbitrary cross-section. Of greatest interest to most studies of the instability itself is the critical velocity $U_c^*(M^*, H^*)$, which is defined as the smallest reduced velocity above which at least one mode of the structure becomes unstable (see for example Figure 2.11 in Section 2.4).

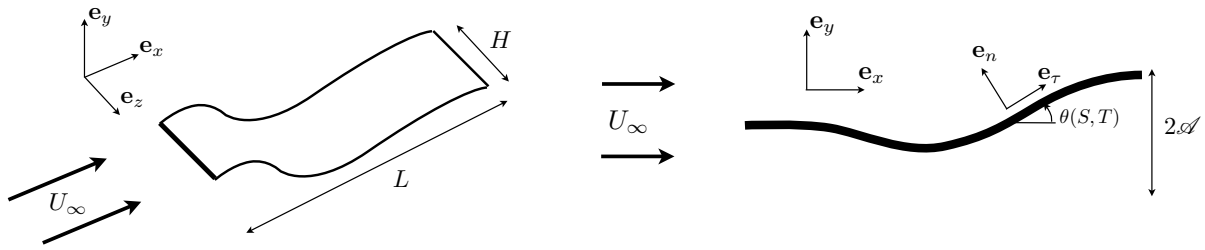

Figure 2.5: (Left) Flutter dynamics of a flag in an axial flow. The deformation of the flag along its span is neglected so that a two-dimensional kinematic description can be retained (right).

2.3.2 An energy harvesting flag?

As for VIV, the spontaneous and self-sustained flapping of a solid body in a steady flow is particularly interesting from an energy harvesting point of view. The energy extraction can be achieved following two different routes: (i) localized energy harvesting at the upstream attachment pole if the flag is free to rotate and (ii) distributed energy harvesting on the surface of the flag using, for example, piezoelectric materials, converting the flag's bending motion into electric charge transfers (see Section 2.4). The research work I have been carrying out at LadHyX in the last three years on this problem has been entirely dedicated to the latter option. However, the question of the relative efficiency of both strategies remains open, and will be part of my future research on this topic.

Two different representations of the deformation-based energy harvesting will be considered: pure damping (in this section) and an explicit description of the energy transfers between the fluid-solid system and an electric output through a piezoelectric element (Section 2.4). In all cases, the configuration considered is represented in Figure 2.5: a rectangular flag of span H and length L is placed in a horizontal flow U_∞.

To be able to determine the energy harvesting efficiency of the structure, the linear framework is insufficient as it does not provide any information on the saturated dynamics, in particular, in terms of the flapping amplitude $\mathscr{A}$. To obtain such information, the approach followed here is to use numerical simulations for the flapping flag dynamics using a simplified model for the fluid forces. The next section proposes a brief overview of two such models.

2.3.3 Modeling the fluid-solid problem

The nonlinear flapping dynamics of a thin flag in an axial flow is a complex fluid-solid interaction problem, and its direct numerical simulation is particularly expensive. Reduced-order representation of the flow forces therefore represent a promising tool to perform simplified simulations that still grasp the main physical ingredients of the problem while reducing the computational cost and complexity significantly for systematic and efficient energy harvesting performance assessment as well as optimization. Two examples of such reduced-order models are detailed below: (i) a two-dimensional inviscid flow representation and (ii) the Large Amplitude Elongated Body Theory. These two models only differ via their treatment of the flow forces, and they share the same formalism for the solid dynamics.

In both cases, a pure streamwise deformation of the flag is considered (twist and spanwise bending are neglected), and the flag is inextensible so that the geometry of the structure can be alternatively described by $\mathbf{x}(s,t)$, its position, or by $\theta(s,t)$, its local orientation with respect to the flow (Figure 2.5b). Assuming an

Euler–Bernoulli model for the flag, its equation of motion can be written in non-dimensional form:

$$\frac{\partial^2 \mathbf{x}}{\partial t^2} = \frac{\partial}{\partial s}\left[T\boldsymbol{\tau} - \frac{1}{U^{*2}}\frac{\partial^2 \theta}{\partial s^2}\mathbf{n}\right] + M^*\mathbf{f}, \qquad \frac{\partial \mathbf{x}}{\partial s} = \boldsymbol{\tau}. \tag{2.11}$$

In the previous equation, T is the (unknown and non-uniform) flag tension, $(\boldsymbol{\tau}, \mathbf{n})$ is the local curvilinear orthonormal basis and $\mathbf{f}$ is the fluid force.

An inviscid method for the two-dimensional limit ($H^* \gg 1$).

In the two-dimensional flow limit, a reduced-order model for $\mathbf{f}$ can be obtained noting that the flow is inviscid everywhere but within thin boundary layers on the surface of the flag, and that the wake of the flag is characterized by the separation of these boundary layers into free shear layers that roll up into wake vortices. A particular approach, at the center of my PhD work, is to consider that the flow is inviscid everywhere but for discrete singularities in the form of point (or line) vortices of position $\tilde{\mathbf{x}}_n$ and intensity $\Gamma_n(t)$. The last shed vortex has a time-varying intensity to account for the continuous shedding of vorticity into the free flow from the trailing edge and to guarantee the regularity of the flow at the flag's trailing edge (unsteady Kutta condition). Older vortices have a time-independent intensity, neglecting the diffusion of vorticity on the typical flapping time-scale of the flag. The equation of motion for the vortices must be modified from the classical Kirchhoff's law to guarantee the conservation of momentum in the fluid, leading to the modified equation of motion, known as the Brown–Michael equation

$$\frac{\mathrm{d}\tilde{\mathbf{x}}_n}{\mathrm{d}t} + \frac{(\tilde{\mathbf{x}}_n - \mathbf{x}_e)}{\Gamma_n}\frac{\mathrm{d}\Gamma_n}{\mathrm{d}t} = \tilde{\mathbf{u}}_n, \tag{2.12}$$

where $\mathbf{x}_e(t) = \mathbf{x}(s = 1)$ is the position of the trailing (shedding) edge of the flag, and $\tilde{\mathbf{u}}_n$ is the local flow velocity at the vortex position once the self-induced singularity has been removed). A shedding criterion must be chosen to determine when to release a new vortex and it was chosen to do so when the intensity Γ_n of the last vortex reaches a maximum in magnitude (thereby ensuring that a vortex can not unroll and that the fluid force is continuous). The inviscid fluid flow is completely determined by the position and velocity of the flag, and the position and intensity of the vortex singularities, and can then be used to compute the pressure forces applied to the flag. One then obtains an explicit formulation of the fluid-solid problem as a set of ODEs for the fluid coupled to the solid dynamics (Michelin & Llewellyn Smith, 2009*c*, 2010). In the case of a flexible flag, the inviscid flow around the deformable structure is computed by representing the solid as a bound vortex sheet whose intensity is such that the slip boundary condition is satisfied on either side (Michelin *et al.*, 2008; Michelin & Llewellyn Smith, 2009*b*). An alternative approach to this discretization of the wake consists in representing the wake as a continuous vortex sheet distribution (see Alben, 2009, for a complete presentation and references). Numerically, this formulation is a bit more complex as regularization and tapering must be used to ensure stability and convergence of the method (Alben, 2010).

The Large Amplitude Elongated Body Theory ($H^* \ll 1$)

In the opposite limit, the flow is not two-dimensional anymore as fluid can pass around the flag on its side and a different approach must be followed. When the typical wavelength of the flag is much larger than its typical spanwise dimension, the inviscid flow forces can be computed asymptotically in terms of the local velocity of the flag relative to the flow:

$$\mathbf{f}_{\text{react.}} = -\frac{\partial}{\partial t}(m_a u_n \mathbf{n}) + \frac{\partial}{\partial s}\left(m_a u_n u_\tau \mathbf{n} - \frac{1}{2}m_a u_n^2 \boldsymbol{\tau}\right) = -\left[\frac{\partial}{\partial t}(m_a u_n) + \frac{\partial}{\partial s}(m_a u_n u_\tau) - \frac{1}{2}m_a u_n^2 \frac{\partial \theta}{\partial s}\right]\mathbf{n}, \tag{2.13}$$

with $\mathbf{u} = u_\tau \boldsymbol{\tau} + u_n \mathbf{n} = \partial \mathbf{x}/\partial t - \mathbf{e}_x$. This reactive force is purely normal (it only includes inviscid pressure forces) and can be understood as follows. In the slender body limit, the flow is dominated by the normal displacement of the flag's cross section and an added fluid momentum $m_a u_n \mathbf{n}$ can be associated with each cross-section, with $m_a = \pi H^*/4$ in non-dimensional form. The first and second terms in Eq. (2.13) correspond to a balance of fluid and solid momenta and the last term is associated with the pressure forces. This reactive force was first introduced by Lighthill (1971) to study the fluid forces on swimming fish and its expression as an asymptotic expansion of the flow forces was recently validated by Candelier *et al.* (2011). It is valid for large displacements of the structure provided that the local curvature radius is large compared to the spanwise dimension, and Candelier *et al.* (2011) validated the predictions of this model with full RANS simulations in a similar problem.

This theory by definition neglects any flow separation on the sides of the flag and the associated dissipative effects. Although these effects are not critical when the kinematics of the body are imposed (as for the fish problem), this simplification becomes problematic when looking at freely flapping bodies, as it would lead to an important over-estimation of the flapping amplitude (see for example Singh *et al.*, 2012*b*). To correct this, a resistive force is empirically added as a form drag solely on the transverse motion of the flag following Taylor (1952) and Eloy *et al.* (2012):

$$\mathbf{f}_{\text{resist.}} = -\frac{1}{2} c_d |u_n| u_n \mathbf{n} \tag{2.14}$$

with c_d, the dimensionless drag coefficient of the cross-section. The combination of Eqs. (2.13)–(2.14) provides a completely local description of the flow forces. Although strictly speaking limited to the limit $H^* \ll 1$, Eloy *et al.* (2012) showed that its predictions for $H^* = 0.1$–0.5 remained consistent with experimental observations of a freely-flapping flag.

In the following, such simplified methods are applied to study the energy harvesting potential of a flapping flag. Because of its simpler framework, only results obtained with the slender body assumption will be presented, keeping in mind that many conclusions remain valid at least qualitatively.

2.3.4 Destabilization by damping

Energy harvesting essentially amounts to extracting energy from a mechanical system to transfer it to an electrical loop. From the mechanical system's point of view, energy is lost and that is the main motivation for representing energy harvesting as an additional damping. Whether this is done directly through an added structural damping or through the complete description of a piezoelectric system, it is essential to assess the effect of damping on the fluid-solid system in terms of stability and nonlinear behavior. The former approach, which is the focus of the present chapter, simply considers an added deformation-based structural damping as a representation for energy harvesting. In the next section, we are interested in the effect of the spatial distribution of this damping or energy harvesting so in general, we consider a Kelvin-Voigt type model with non-uniform intensity distribution, such that the equation of motion Eq. (2.11) becomes:

$$\frac{\partial^2 \mathbf{x}}{\partial t^2} = \frac{\partial}{\partial s}\left[T\boldsymbol{\tau} - \frac{1}{U^{*2}}\frac{\partial}{\partial s}\left(\frac{\partial \theta}{\partial s} + \xi(s)\frac{\partial^2 \theta}{\partial s \partial t}\right)\mathbf{n}\right] + M^* \mathbf{f}, \qquad \frac{\partial \mathbf{x}}{\partial s} = \boldsymbol{\tau}, \tag{2.15}$$

and the non-dimensional instantaneous harvested power is

$$\mathcal{P} = \frac{\langle \mathscr{P} \rangle}{\rho_f U_\infty^3 L H} = \frac{1}{M^* U^{*2}} \int_0^1 \xi(s) \left\langle \left(\frac{\partial^2 \theta}{\partial s \partial t}\right)^2 \right\rangle \mathrm{d}s. \tag{2.16}$$

Our physical intuition is that damping extracting energy from the system will tend to reduce any flapping amplitude or re-stabilize the state of rest of the fluid-solid system. This would correspond to an increase

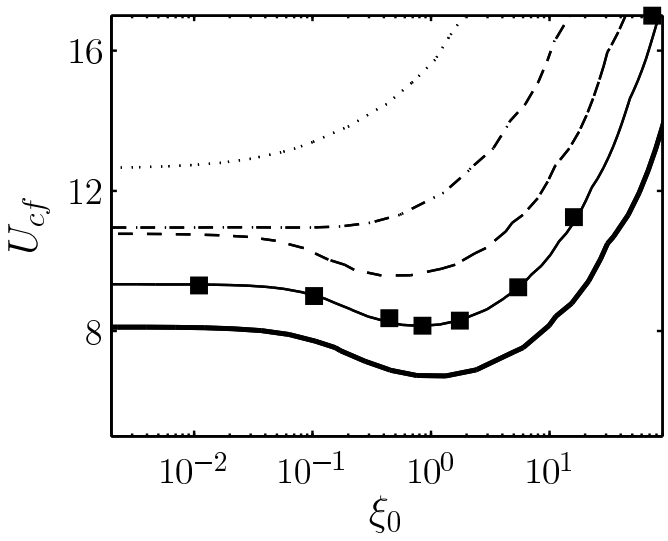

Figure 2.6: Evolution of the critical velocity above which flapping develops as a function of damping intensity ξ_0 for a uniform distribution of deformation-based damping (Kelvin-Voigt), and mass ratios $M^* = 2.5$ (dotted), $M^* = 5.1$ (dash-dotted), $M^* = 8.5$ (dashed), $M^* = 12.7$ (solid) and $M^* = 20$ (thick solid). Black squares corresponds to the critical flow velocity as computed using non-linear simulations.

of the critical velocity, and is indeed observed in the case of heavy flags (low M^*, Figure 2.6). However, a somewhat counter-intuitive *destabilization by damping* phenomenon is observed for larger M^* (or lighter flags) corresponding to a lower critical velocity U_c^* (Figure 2.6): in that case, the extraction of energy actually promotes the instability and increases the range of operability of the system.

This observation, although counter-intuitive, is a classical feature of such fluttering systems and has been developed at length by Paidoussis (1998, 2004) and more recently in the work of Doaré (2010). In a local stability analysis, it is associated with the presence of negative energy neutral waves (see Section 2.4 for more details). The possibility for destabilization stems from the fluid-solid system not being closed nor conservative but instead receiving an unconstrained amount of energy through the incoming flow. Classical stabilization arguments generally find their roots in conservative systems.

2.3.5 Optimal damping distribution

The deformation of the flag during its flapping motion, even in the periodic regime, is strongly non-uniform, with no curvature at the free end and no displacement at the leading edge. In the approach considered here, curvature changes result in energy extraction and in an attempt to harvest as much energy as possible, it seems reasonable to seek an optimal distribution that might focus on particular regions of the flag, for example in the regions of higher curvatures. On the other hand, the instability itself is directly linked to the presence of curvature along the flag, and the addition of too much damping in these regions may reduce this destabilization and penalize the efficiency of the system. This trade-off and the search for an optimal distribution of damping maximizing the extracted energy has been one of the main axes of my research in the last three years, in particular during the postdoctoral work of K. Singh at LadHyX under the supervision of E. de Langre and myself (Singh *et al.*, 2012*a*,*b*).

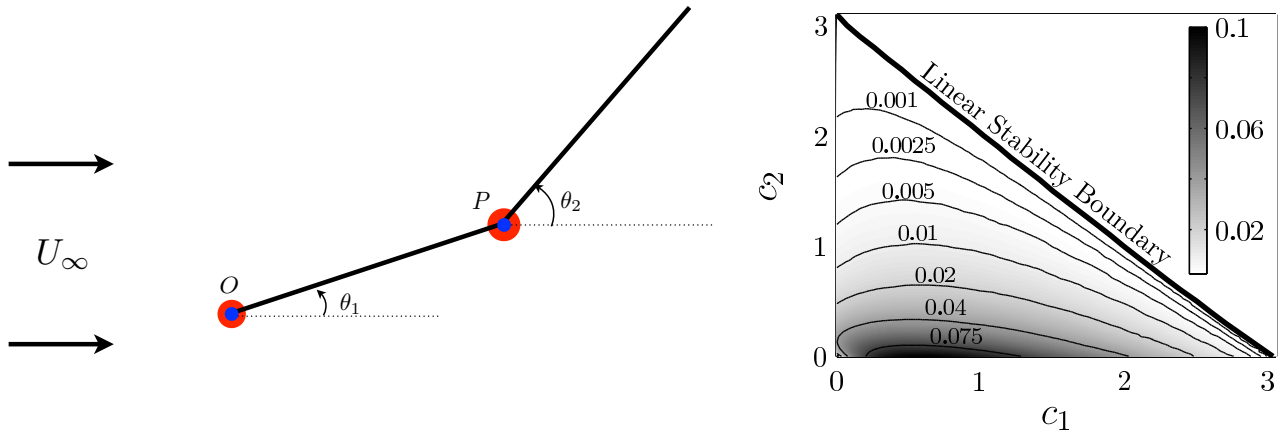

Figure 2.7: (Left) Reduced-order model of the energy harvesting flag: two rigid cylinders articulated at O and P where all the deformation occurs. Stiffness and damping are modeled at both articulations as rotational springs and dashpots. Damping is measured by the intensities c_1 (in O) and c_2 (in P) of the two dashpots. (Right) Evolution of the harvested power with the damping intensities.

A test problem: the bi-articulated system

To try to obtain some physical insight on that particular problem, a reduced-order system was first considered in the form of two articulated cylinders (note that the formulation could easily be generalized to two articulated rigid plates): bending rigidity and energy extraction are represented as singular distributions in the form of torsional springs and dashpots (Figure 2.7). The advantage of this formulation is that it retains the flutter-type dynamics of the continuously-deformable flag (two degrees of freedom are necessary to develop curvature) while restricting the space of possible damping distribution to two parameters. Intuition, which hints that harvesting energy at both locations would enable a greater output than a single damper, is once again misleading: indeed, it appears that the largest dissipated power is obtained when damping is exclusively placed at the fixed upstream edge (Figure 2.7). Adding damping at the moving articulation would provide more energy from this second damper but this would be counter-balanced and exceeded by a loss of energy from the first damper associated with a resulting reduced flapping amplitude. This illustrates the double role played by curvature in both the instability and the energy harvesting process. This also emphasizes the critical effect of damping on the system's dynamics.

Continuous system and optimal damping distribution

Moving on to the general system, we consider a slender body with a continuous deformation-based damping distribution as proposed in Eq. (2.15). We first focus on the simplest non-uniform case, namely a linear distribution of damping

$$\xi(s) = \xi_0 \left[1 + \xi_1 \left(s - \frac{1}{2} \right) \right]. \tag{2.17}$$

In the equation above, ξ_0 is the total amount of damping in the system while $0 \leq |\xi_1| \leq 2$ is a measure of its non-uniformity: $\xi_1 = 0$ corresponds to a uniform distribution and $\xi_1 = \pm 2$ corresponds to a vanishing damping at one end, with $\xi_1 \leq 0$ (resp. $\xi_1 \geq 0$) referring to decreasing (resp. increasing) damping in the streamwise direction. Figure 2.8(a) shows that regardless of the total damping intensity, the optimal configuration is always obtained when $\xi_1 = 2$ (which corresponds to no damping at the fixed end and maximum damping near the free end), and is associated to a 50% increase of the harvested power in comparison with

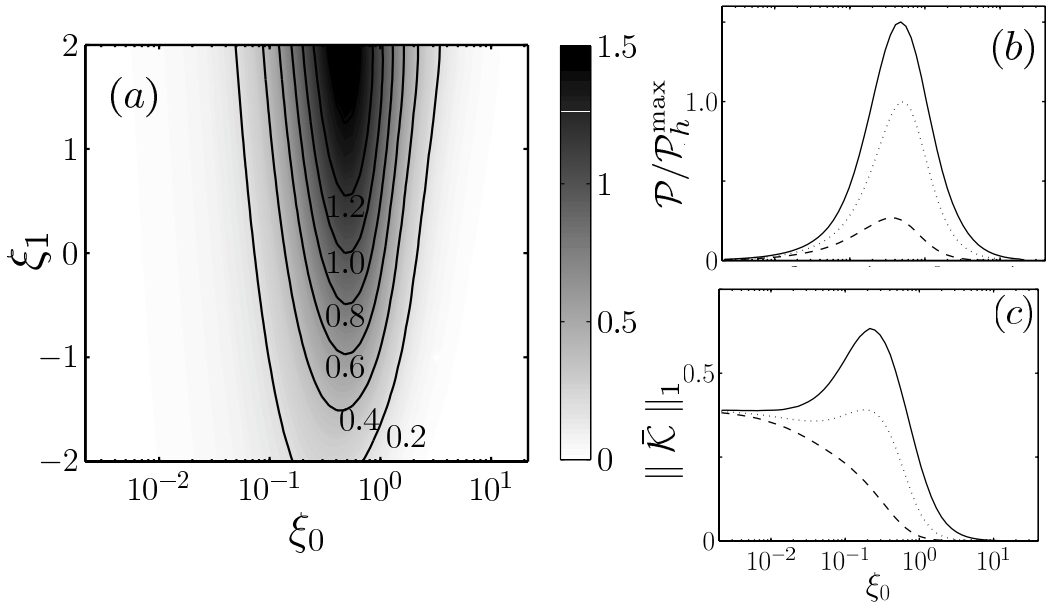

Figure 2.8: (a) Harvested power for a linear distribution of damping as a function of the total damping ξ_0 and slope of the damping distribution ξ_1. (b) Harvested power as a function of the total damping for the case of increasing ($\xi_1 = 2$, solid), constant ($\xi_1 = 0$, dotted) and decreasing ($\xi_1 = -2$, dashed) damping intensity. For both (a) and (b), the harvested power is normalized by the maximum power obtained using uniform damping. (c) Evolution of the r.m.s. of the normalized curvature change of the solid body (see Singh *et al.*, 2012*a*, for more details). All results were obtained for $H^* = 0.1$, $M^* = 12.7$ and $U^* = 13$.

the uniform case (Figure 2.8b). From Eq. (2.16), the non-dimensional harvested power $\mathcal{P}$ is intimately linked to the distribution of curvature characterized by $\mathcal{K}(s) = \left\langle (\partial^2\theta/\partial s \partial t)^2 \right\rangle$. Figure 2.8(c) shows that in the optimal configuration ($\xi_1 = 2$), an increase in the curvature change $||\mathcal{K}||_1$ is observed. Regardless of ξ_1, we also recover the rigidifying effect of a large damping on the structure: it prevents the deformation of the flag, thereby reducing drastically the harvested power and efficiency (Figure 2.8b).

Such lineic distribution is however not particularly adapted to a precise targeting of particular regions, for example the upstream part of the flag as suggested by the bi-articulated model. The analysis is then extended to a focused (Gaussian) distribution of damping

$$\xi(s) = \tilde{\xi}_0 \mathrm{e}^{-\alpha(s-s_0)^2}, \tag{2.18}$$

where s_0 is the distribution's center, $1/\sqrt{\alpha}$ is a measure of its peak width, and $\tilde{\xi}_0$ is defined such that the total damping in the system is equal to ξ_0. Large (resp. small) α therefore correspond to focused (resp. distributed) damping functions. It is observed that the intensity of the total damping significantly modifies the optimal distribution: for small damping, the distribution is a narrow peak centered on the region of maximum curvature (Figure 2.9). When damping is increased, the optimal distribution spreads over an increasing area of the flag and converges toward an optimal function that is close to the estimate obtained with the linear distribution. This can be understood as follows: for small ξ_0, the effect of the energy loss on the system is negligible, and the dynamics are not modified in comparison to the undamped case. The optimal distribution therefore consists in putting all of the damping in the region of maximal curvature change. With a larger damping intensity, the system reacts to the local energy extraction of a focused distribution by "avoiding" any curvature in that region leading to a *de facto* rigidification of the damped section. Therefore,

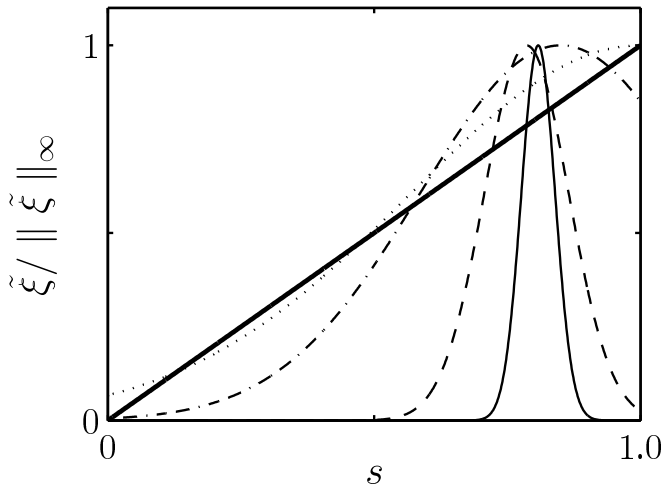

Figure 2.9: Evolution of the optimal distribution of damping for a Gaussian (peaked) damping function and increasing total damping ξ_0: $\xi_0 = 0.004$ (solid), $\xi_0 = 0.025$ (dashed), $\xi_0 = 0.25$ (dash-dotted) and $\xi_0 = 0.47$ (dotted). The optimal linear distribution is also shown for reference (thick solid). For all cases, the damping intensity was normalized by its maximum value.

for significant damping intensities, it is necessary to spread the energy extraction throughout the structure to prevent this avoidance mechanism.

From an energy harvesting point of view, the optimal distribution obtained for fundamentally different families of function $\xi(s)$ (linear and Gaussian) provide similar results, which suggests that this optimum, obtained on a reduced functional space, may be close to the global optimum, although a full optimization remains to be done. Also it is interesting to compare the apparently contradictary conclusions of the bi-articulated system and the continuous flag. In the former, optimal energy harvesting was achieved with a concentration of damping at the fixed leading edge, while the latter suggests placing more damping toward the downstream end. These two results are however not incompatible as both systems are in fact fundamentally different: in the bi-articulated system, the moving articulation is extremely sensitive to damping as it is the only moving point of curvature of the system and is therefore completely responsible for the existence of the instability. In the continuous system, it is not the case due to the larger number of degrees of freedom of the deformation.

Finally, we observe here an optimal non-dimensional harvested power of $\mathcal{P} \approx 0.0063$ which corresponds to an energy harvesting efficiency of 2.1% for this particular choice of (M^*, U^*, H^*). This value is significant albeit still quite low. This, and comparison with results obtained in the next section with different values of these parameters, suggests that beyond the optimization of the positioning of the harvesters, an optimization of the operating conditions (in particular the stiffness of the structure related to the operating flow velocity or the structure's aspect ratio) will be a critical step to increase the system's performance.

2.4 The piezoelectric flag: a coupled fluid-solid-electric problem

The simplicity of the model used to represent the energy harvesting mechanism in the previous section (a Kelvin–Voigt damping) allows for fast computations of the fluid-solid coupled dynamics and optimization of the spatial distribution of damping on the structure. However, this model only gives a partial description of the dynamical transfer of energy between the fluid-solid system and the output of the energy harvesting

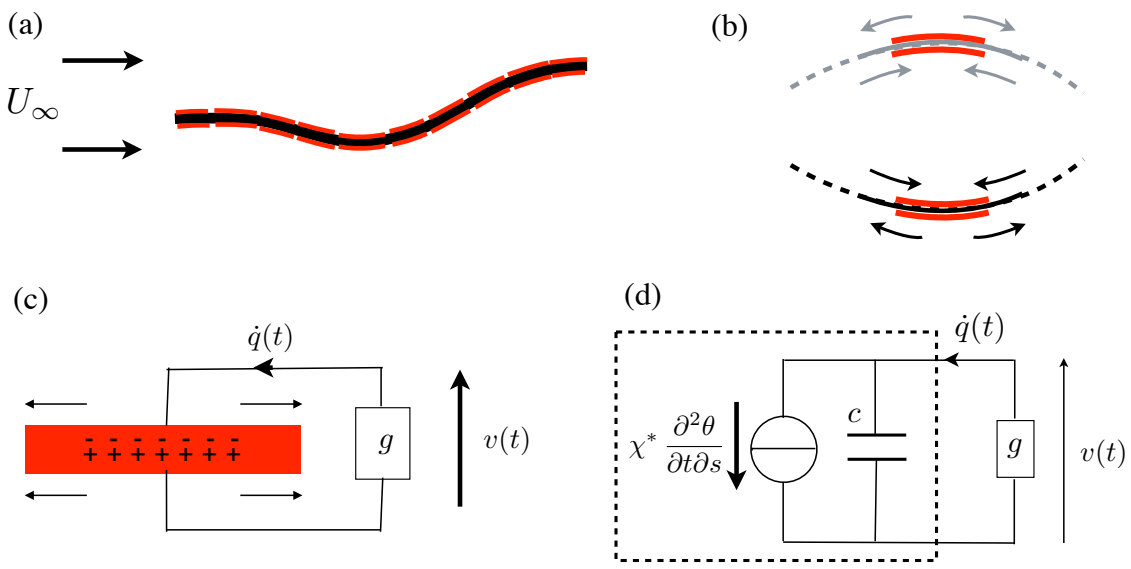

Figure 2.10: (a) Flutter of a flag in an axial flow. The flag is covered with piezoelectric patches on both sides (red). Periodic bending of the flag induces compression and stretching of the piezoelectric elements (b) resulting in a charge transfer at their electrodes that can be used to power an output circuit (c). (d) Electric equivalent of the piezoelectric patch pair characterized by a current generator and an internal capacitance.

device. In this section, we propose an explicit formulation and representation of the mechanism responsible for the energy conversion and present some results obtained for the simplest output circuit: a pure resistor.

2.4.1 A fully-coupled model

Whether made out of crystals, polymers, ceramics or composite materials, piezoelectric solids all share the ability to convert mechanical energy into electric energy (and vice-versa). This property stems from the arrangement of ions in their atomic structure, which leads to a modification of their polarization when they are strained. In the case of a thin piezoelectric element, this leads effectively to a net charge transfer to its electrodes that act as equipotentials on either side of the layer. The inverse effect, i.e. the mechanical response to an electric forcing, is due to the response of the polarization to the electric field resulting from a voltage applied at the electrodes. This electro-mechanical coupling and its preferential directions are determined during the fabrication process of the material.

The piezoelectric flag consists of piezoelectric thin patches attached to the flag's surface. The deformation of the flag during its flapping motion results in a stretching or compression of these elements located away from the center line of the flag (Figure 2.10). Here, the polarity of the material in the direction normal to the flag is coupled to the mechanical strain and stress in the tangential direction (3–1 coupling). Considering only pairs of piezoelectric patches, shunted through the flag, positioned symmetrically with respect to the flag's center line and of reversed polarity (so that the charge transfer induced by a stretching of the upper patch is equal to the charge transfer resulting from the compression of the lower patch), the macroscopic electric state of the patch-assembly is characterized by the charge transfer $Q(t)$ and voltage $V(t)$ between the electrodes. The direct and reverse piezoelectric effects can then be described as

$$Q = CV + \chi(\theta(s^+) - \theta(s^-)), \qquad \mathcal{M} = B\frac{\partial\theta}{\partial s} - \chi V(t)\mathbf{1}_{[s^-,s^+]}(s). \tag{2.19}$$

In the previous equation, s^- and s^+ refer to the upstream and downstream curvilinear position of the patch pair, $\mathbf{1}_A$ is the characteristic funtion of the interval A, and $\mathcal{M}$ is the total internal torque in the flag, including both the elastic torque and the effect of the piezoelectric patches. Finally, C and χ are the patches' capacitance and coupling coefficient, which depend on the material's properties, in particular its permittivity. Both electrodes are connected to an output circuit, and in the following we focus exclusively on a resistive circuit of conductance G so that Ohm's law provides an additional relationship between V and Q:

$$GV + \dot{Q} = 0. \tag{2.20}$$

In the following, we consider the limit where the flag is completely covered by piezoelectric patches of streamwise dimension much smaller than the typical wavelength so that a continuum description can be used for the electric state of the piezoelectric patches (Doaré & Michelin, 2011). Defining q, v, c and g as the charge, voltage, capacitance and conductance per unit length in the streamwise direction, the full non-dimensional equations for the fluid-solid-electric system can be obtained from Eq. (2.11), (2.19) and (2.20) as (Michelin & Doaré, 2012)

$$\frac{\partial^2 \mathbf{x}}{\partial t^2} = \frac{\partial}{\partial s}\left[T\boldsymbol{\tau} - \frac{\partial}{\partial s}\left(\frac{1}{U^{*2}}\frac{\partial \theta}{\partial s} \ -\frac{\alpha}{U^*}v\right)\mathbf{n}\right] + M^*\mathbf{f}, \qquad \frac{\partial \mathbf{x}}{\partial s} = \boldsymbol{\tau}, \tag{2.21}$$

$$q = v + \frac{\alpha}{U^*}\frac{\partial \theta}{\partial s}, \tag{2.22}$$

$$\beta\frac{\partial q}{\partial t} + v = 0. \tag{2.23}$$

In addition to Eq. (2.10), two non-dimensional parameters are identified:

$$\alpha = \frac{\chi}{\sqrt{Bc}} \qquad \beta = \frac{c\,U_\infty}{gL}, \tag{2.24}$$

which characterize the electric coupling and the tuning of the output circuit to the characteristic flapping frequency, respectively. Together with appropriate clamped-free boundary conditions, these equations coupled to the flow model (e.g. the LAEBT force approximation presented in Section 2.3.3) form a closed and well-posed system for the mechanical and electrical state of the system. The harvested power is that dissipated in the resistive elements and is computed as

$$\mathcal{P} = \frac{\langle \mathscr{P} \rangle}{\rho_f U_\infty^3 LH} = \frac{1}{\beta M^*}\left\langle \int_0^1 v^2 \mathrm{d}s \right\rangle. \tag{2.25}$$

The advantage of this model resides in its simplicity while still providing an explicit description of the energy transfer mechanism between the solid and electric systems. It can of course be modified to account for more complex output circuits. In the following, we focus on the effect of the coupling α and the tuning of the output circuit to the fluid-solid dynamics characterized by β.

2.4.2 Linear stability analysis

We first study the linear stability of the system in order to determine the operability conditions (i.e. where instabilities can develop). Focusing on small displacements of the flag, the system Eqs. (2.21)–(2.23) can be rewritten in terms of the vertical displacement $y(s,t)$ and charge transfer $q(s,t)$ as:

$$(1+m_a M^*)\frac{\partial^2 y}{\partial t^2} + 2m_a M^*\frac{\partial^2 y}{\partial t \partial s} + m_a M^*\frac{\partial^2 y}{\partial s^2} + \frac{1+\alpha^2}{U^{*2}}\frac{\partial^4 y}{\partial s^4} - \frac{\alpha}{U^*}\frac{\partial^2 q}{\partial s^2} = 0, \tag{2.26}$$

$$\beta\frac{\partial q}{\partial t} + q - \frac{\alpha}{U^*}\frac{\partial^2 y}{\partial s^2} = 0. \tag{2.27}$$

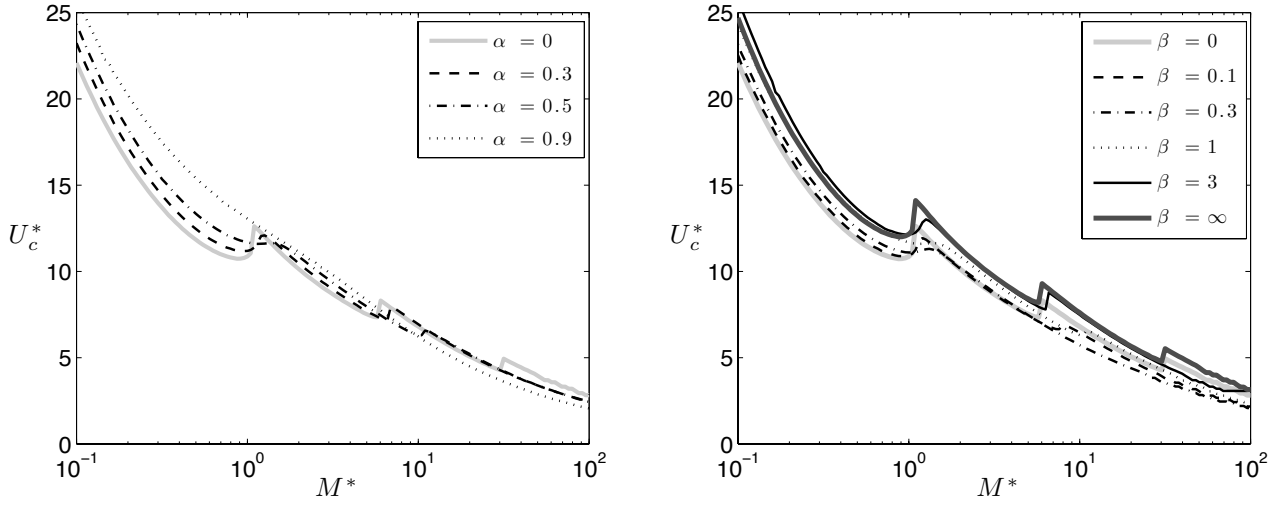

Figure 2.11: Critical flow velocity above which flapping develops, as obtained from a global stability analysis with (left) $\beta = 1$ and varying α, and (right) $\alpha = 0.5$ and varying β.

Classically, two different points of view can be adopted to analyze the stability of the system described by Eqs. (2.26)–(2.27): (i) a mode or *global* approach and (ii) a wave or *local* approach. The former focuses on a finite system with clamped-free boundary conditions, and considers solutions of the form $\mathrm{e}^{-\mathrm{i}\omega t}[Y(s), V(s)]$. The latter effectively focuses on an infinitely long system and considers solutions in the form of progressive waves $\mathrm{e}^{\mathrm{i}(ks-\omega t)}[\bar{V}, \bar{Y}]$. In a recent article (Doaré & Michelin, 2011), we proposed an in-depth analysis of the stability of the piezoelectric flag using both frameworks.

Global stability

In the case of a finite flag, Eqs. (2.26)–(2.27) are analyzed together with clamped-free boundary conditions. The critical velocity threshold U_c^* is defined as the maximum velocity above which at least one mode is unstable (i.e. $\mathrm{Im}(\omega) > 0$); its evolution with M^* is shown for different values of α and β on Figure 2.11. In comparison with the non-piezoelectric flag ($\alpha = 0$), the effect of the piezoelectric coupling can be characterized as (i) a stabilization of the system for heavy flags (small M^*) and (ii) a destabilization of the system for lighter flags (large M^*). This is consistent with the results of Section 2.3 on the effect of damping on the system's stability. This suggests that the destabilizing effect at large M^* is a general mechanism linked to the addition of damping to the system and not to the form of damping considered. Some elements regarding the generality of this destabilization mechanism are given below using the local stability framework.

Beyond the effect of the piezoelectric coupling, the stability of the system is also influenced by the characteristic time-scale of the electric system (equivalent here to an RC loop forced by the piezoelectric generator): for small β, the resistor effectively shunts the piezoelectric's electrodes ($v = 0$) and the behavior of the non-piezoelectric flag is recovered, while for large β, the resistor prevents any charge transfer ($q = 0$) and the piezoelectric patches simply contribute as an additional rigidity to the solid dynamics (Doaré & Michelin, 2011). In between these two regimes, a maximum destabilization of the system is observed for large M^*. The properties of the output circuit (here completely characterized by β) influence the efficiency of the energy transfer to the dissipative circuit and therefore will impact the effective damping properties of the electrical loop.

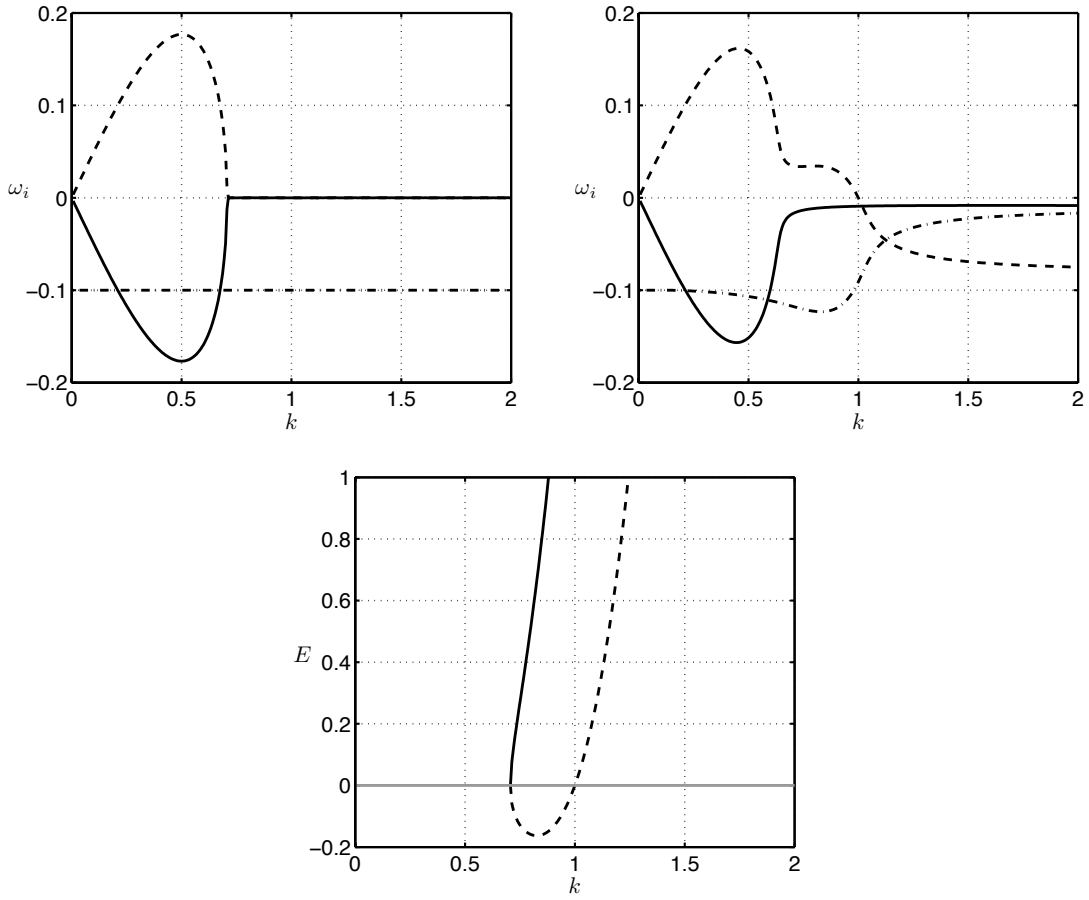

Figure 2.12: (Top-left) Growth rate of the three waves corresponding to a wave-number k for $\alpha = 0$ (no coupling). (Top-right) Growth rate of the three waves corresponding to a wave number k for $\alpha = 0.5$ and $\tilde{\beta} = 10$. (Bottom) Energy of the neutral waves in the uncoupled case $\alpha = 0$ as defined in Doaré & Michelin (2011). The grey continuous line shows the distinction between Positive Energy Waves (above) and Negative Energy Waves (below). In all cases, $m_a = 1$ and $\tilde{U}^* = 0.05$.

Local stability

Some insight on the destabilization by damping is gained from the local stability analysis, which focuses on the local behavior of an effectively infinitely long system. The non-dimensionalization of the system needs to be modified (the flag length is now irrelevant): $\rho_s/\rho H$ is chosen as a reference length scale (this particular choice effectively sets $M^* = 1$) and (U^*, β) are redefined accordingly as $(\tilde{U}^*, \tilde{\beta})$. For real wavenumbers k, unstable waves correspond to $\mathrm{Im}(\omega_i) > 0$ (temporal approach). Figure 2.12 shows the wave's growth rate for non-piezoelectric ($\alpha = 0$) and piezoelectric flags ($\alpha = 0.5$). In addition to the long waves (small k) that are always unstable, the piezoelectric coupling destabilizes an additional range of neutral waves.

This is an example of destabilization by damping of so called *Negative Energy Waves* (Benjamin, 1963; Cairns, 1979). Within this framework, originally presented by Cairns (1979) for inviscid parallel flow instabilities, the energy of a neutral wave is defined as the work necessary to create the wave from a state of rest, and can be directly obtained from the dispersion relation $\mathcal{D}(\omega, k)$ of the non-dissipative system as $E = \omega/4(\partial\mathcal{D}/\partial\omega)A^2$, with A the amplitude of the wave. Figure 2.12 shows that the neutral waves destabilized by the introduction of the piezoelectric coupling indeed correspond to those with negative energy. In

contrast with classical *Positive Energy Waves* that are stabilized by damping (e.g. surface gravity waves or elastic waves on a flexible sheet), the formation of *Negative Energy Waves* releases energy, and their sensitivity to damping is reversed. This peculiar type of waves is associated with the presence of an open flow which basically acts as an unlimited energy reservoir in this problem.

This confirms that the destabilization by damping observed in the piezoelectric coupling of a resistive element to the fluid-solid system or in the addition of a Kelvin-Voigt damping (Section 2.3) is a general mechanism that is intrinsically linked to the dynamics of the neutral waves in the non-dissipative flag. From an energy harvesting point of view, this destabilization by damping represents an increase of the operability range, as self-sustained oscillations of the system (and energy conversion) develop for lower velocities. It also illustrates one of the feedback mechanisms of the energy extraction on the dynamics of the harvesting system.

2.4.3 Non-linear dynamics and efficiency

The energy harvesting performance is characterized here by the efficiency of the piezoelectric system, namely the fraction of the flow kinetic energy (measured through the cross section occupied by the flapping flag) actually transferred to the useful load in the output circuit (here, the resistive element). This model is obviously oversimplified as it neglects any energy loss in the output circuit (i.e. all dissipated energy is considered "useful"), but it is nevertheless interesting as it extends the analysis of the previous section by providing a first measurement of the system's efficiency as a quantitative measure of how much energy can be dissipated in this system. Practically, the efficiency is computed as $\eta = \mathcal{P}/\mathcal{A}$ where $\mathcal{P}$ is defined in Eq. (2.25) and $\mathcal{A}$ is the non-dimensional mean flapping amplitude (Figure 2.5).

Non-linear dynamics and mode switching

The flapping amplitude increases continuously with U^* above the instability threshold (Figure 2.13), confirming the supercritical nature of the transition associated with the slender body approach and demonstrated by Eloy *et al.* (2012). This results in a continuous increase of the efficiency for fixed β, at least initially. When the flow velocity is further increased, sudden drops in the efficiency are observed and can be associated to mode switching events affecting in particular the flapping frequency of the system (Michelin & Doaré, 2012). This mode switch phenomenon is particularly present for large M^*, and significantly impacts the system's efficiency and its robustness, as peak efficiency is achieved just before mode switching occurs.

The effect of the output circuit

Figure 2.13 also emphasizes the effect of the output circuit on the harvesting performance: the efficiency becomes infinitesimal for small and large β. This result is not surprising since the electric system considered here is equivalent to an RC loop forced by the piezoelectric current generator (Figure 2.10): when $\beta\omega \ll 1$ (resp. $\beta\omega \gg 1$), the resistor effectively behaves as a short-circuit (resp. open loop) and the voltage (resp. current) in the resistor vanishes, preventing any energy harvesting.

The key and non-trivial element here is that the characteristics of the forcing, namely the flapping frequency and amplitude of the fluid-solid system (and therefore of the piezoelectric generator), are not imposed *a priori* but result instead from the nonlinear dynamics of the fluid-solid-electric system. Figure 2.14 confirms that maximum efficiency is obtained when the flapping frequency is close to the characteristic frequency of the output circuit ($\omega \approx 1/\beta$), but it also shows that the flapping frequency and amplitude are significantly modified by β.

This feedback of the electric output on the fluid-solid dynamics can be seen as a source of complexity in trying to understand or model the nonlinear coupled dynamics of the fluid-solid-electric system. But it also

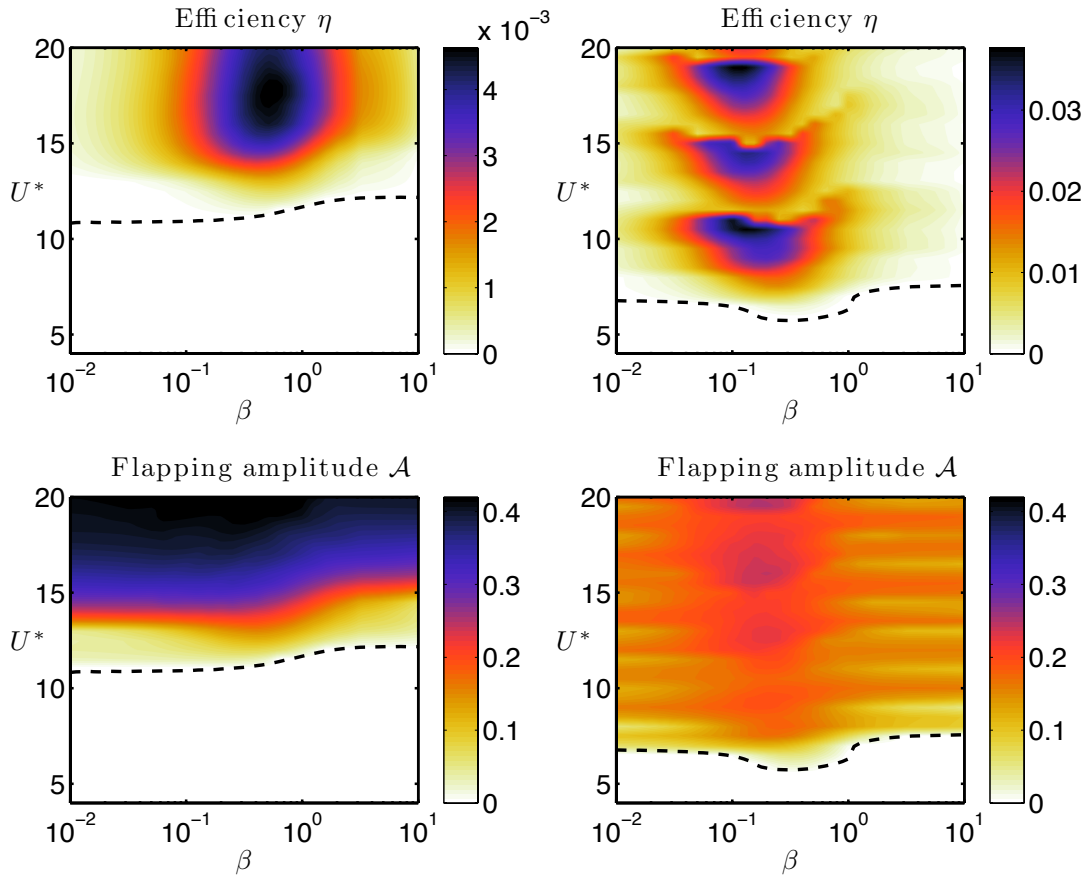

(a) $M^* = 1$ (b) $M^* = 10$

Figure 2.13: Evolution of the harvesting efficiency η (top) and flapping amplitude $\mathcal{A}$ (bottom) with the tuning parameter β and the non-dimensional velocity U^* for $M^* = 1$ (left) and $M^* = 10$ (right). The dashed line indicates the critical velocity below which the system is stable and no energy can be harvested.

represents an opportunity to passively or actively control the vibration of the system through the output circuit (e.g. to increase the system's efficiency or its robustness to fluctuations in the flow velocity).

Flag inertia and peak efficiency

Figure 2.13 also shows the importance of the flag's inertia in achieving high efficiencies: while peak efficiencies of a few percent are typically achieved for lighter flags ($M^* = 10$), heavier flags ($M^* = 1$) only lead to peak efficiencies equal to at most 0.5%. This is confirmed in Fig. 2.15 where the maximum efficiency (obtained for the optimal tuning ratio) is represented as a function of M^* and U^*. Significant harvesting efficiency is achieved ($\approx 12\%$ in the parameter range considered) for lighter flags, and this can be related to the peak conversion efficiency observed in our linear study (Doaré & Michelin, 2011): solid energy is transferred to the electric circuit in a greater proportion in the regions that have been destabilized by damping. In the present design, such high efficiency values are however associated with a greater sensitivity to the flow velocity (in particular through the mode switching event mentioned earlier).

This simplified model represents an original and preliminary attempt at representing the coupled dynamics

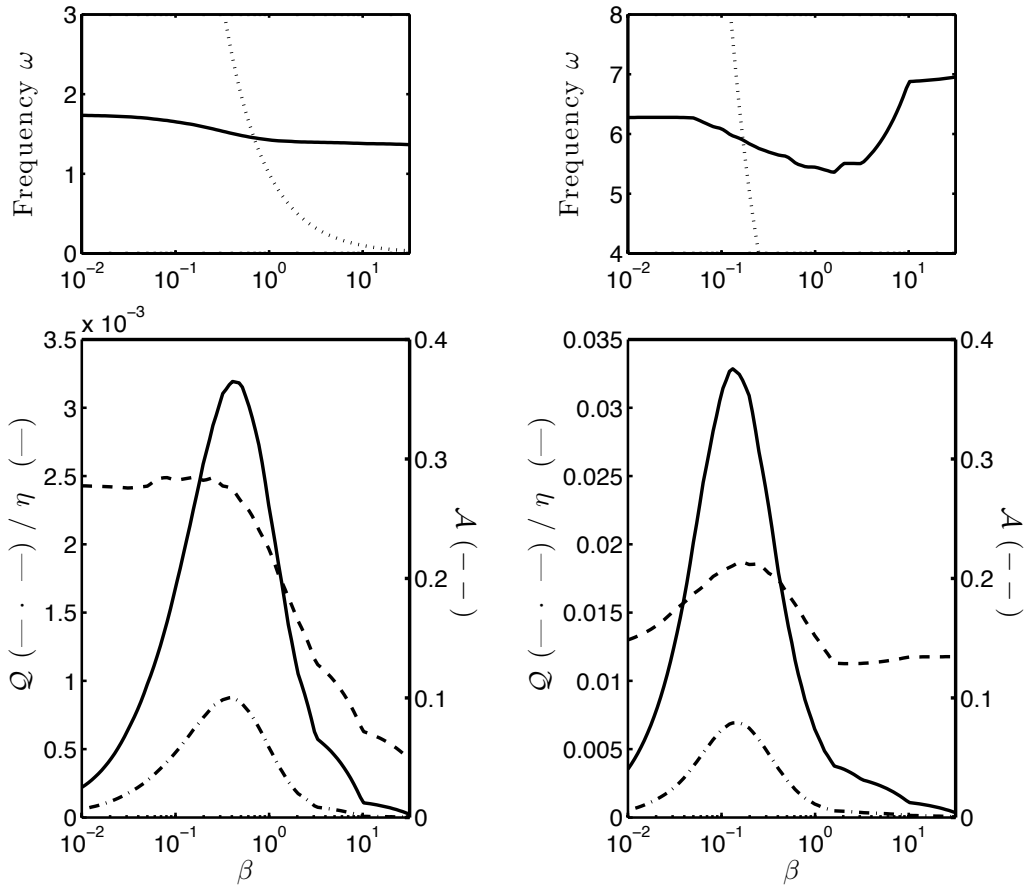

(a) $U^* = 14.5$, $M^* = 1$ (b) $U^* = 14.5$, $M^* = 10$

Figure 2.14: (Top) Flapping frequency (solid) and output circuit characteristic frequency ($1/\beta$, dashed) as a function of the tuning parameter β. (Bottom) Evolution of the harvested energy (solid), harvesting efficiency η and flapping amplitude $\mathcal{A}$ with the tuning parameter β. Results are shown for $M^* = 1$ (left) and $M^* = 10$ (right) as representative cases of heavy and light flags, respectively.

of the fluid, solid and electric systems, including the feedback effect of the energy harvester on the fluid-solid system dynamics. The importance of this feedback effect is obviously linked to and scales quadratically with the coupling coefficient α. This non-dimensional parameter depends on the geometry of the system (in particular the relative stiffnesses of the piezoelectric and non-piezoelectric layers), but it is also intrinsically limited by the material properties (in particular the permittivity and polarizability of the material). PZT materials available off the shelf today typically correspond to $\alpha \approx 0.3$. The results presented here therefore correspond to an upper bound of what may be achieved today with available materials, and illustrate the particular importance of materials research in designing piezoelectric elements of greater α.

Nonetheless, the efficiencies obtained for such energy harvesting flags (both in Sections 2.3 and 2.4), although lower than what may be obtained by turbine technology, are significant. The complex dynamics of the flag system, and its coupling to a more advanced and carefully-designed output circuit, are promising elements for its optimization.

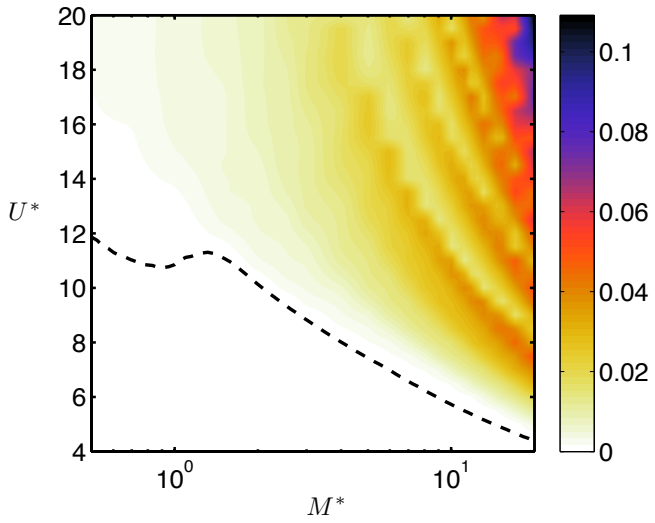

Figure 2.15: Evolution of the maximum efficiency $\eta_{\text{opt}} = \max_\beta(\eta)$ as a function of (M^*, U^*) for $H^* = 0.5$ and $\alpha = 0.5$. The dashed line represents the minimum of the velocity threshold over all possible values of β.

2.5 Ongoing work and perspectives

Understanding the nonlinear dynamics of classical fluid-solid systems coupled to dissipative elements has been and will remain at the center of my research in the coming years. It represents a significant development and scientific investment of LadHyX in the field of fluid-structure interactions and goes beyond the two main geometries that I have chosen to present here. In particular, the development of an experimental activity in that domain together with Pascal Hémon and Xavier Amandolese represents an important opportunity for developing this research topic in the coming years and encouraging collaborations within LadHyX and with other research teams.

My interest in the nonlinear dynamics of flexible solids in steady flows goes however beyond applications to energy harvesting, and in the coming years, I will dedicate a significant effort to extend this activity to biolocomotion at high Re, in particular for fish swimming. As emphasized in the introduction of this chapter, the locomotion and energy harvesting problems follow fundamentally opposite routes in terms of fluid-solid energy exchanges, for example. They do, however, share several important questions and challenges in particular regarding the understanding and modeling of hydrodynamic interactions. Hydrodynamic interactions for swimming fish is the focus of a future collaboration with PMMH (ESPCI, Paris) and IRPHE (Marseille) that has been formalized in the ANR project "NAGE" that was submitted in 2013.

Nevertheless, my activity in high-Re fluid-solid interactions will be predominantly focused on energy harvesting problems, in particular on the piezoelectric flag system during the ANR project "FLUTTENER". This Young Investigator grant (2013–2016) will enable me to develop a pluridisciplinary program in collaboration with Olivier Doaré (ENSTA ParisTech) and Dejan Vasic (ENS Cachan) focusing on the fluid-solid dynamics as well as the optimization of the output circuit using state-of-the-art power electronics systems.

Below are presented some important questions that I would like to address in the coming years on these topics:

– *What is the role of the output circuit in optimizing the energy harvesting performance?*

  The results of Section 2.4 focused exclusively on the simplest possible output circuit. They showed: (i) that the effect of a realistic representation of the energy harvesting system is not strictly equivalent to

structural damping and (ii) that the output circuit properties can significantly influence the fluid-solid dynamics and hence the fluid-solid-electric system efficiency. The first step will be to consider electric systems with intrinsic dynamics, starting with inductive circuits, which will provide the output loop with a fundamental frequency and resonant properties. This is the current focus of the PhD work of Yifan Xia, and preliminary results suggest that richer dynamics (including lock-in between the fluid-solid and electric frequencies) may be encountered leading to significant increases in the harvesting efficiency.

Optimization of the energy harvesting performance of an output circuit for prescribed mechanical forcing is a classical problem of power electronics for which performant tools have been developed, using for example active switching techniques (Guyomard *et al.*, 2005) that enable a drastic increase in the performance of the device in comparison with a purely passive resistor-type circuit. A main challenge of the FLUTTENER project will be to apply such state-of-the-art techniques to the piezoelectric flag system, assessing in particular the feedback effect of such active circuits on the fluid-solid dynamics.

– *The role of hydrodynamic interactions between flapping solids*

Flapping flags in tandem or in side-by-side positions do not flap independently but instead tend to synchronize either in-phase or out-of-phase (Zhang *et al.*, 2000; Zhu & Peskin, 2003; Michelin & Llewellyn Smith, 2009*a*; Schouveiler & Eloy, 2009). Beyond the simple synchronization, the flapping properties may also be impacted in particular the flapping amplitude (Michelin, 2009) and this may result in important dynamical effects (e.g. drag reduction, Ristroph & Zhang, 2008). In biological systems, hydrodynamic interactions are thought to offer some energetic advantage to fish swimming in schools.

These are illustrations of the effect of hydrodynamic interactions on the dynamics of neighboring freely or actively flapping solids. In the energy harvesting problem, a critical question is to understand the impact on the harvesting performance: is there any destructive interaction penalizing the efficiency of a farm of energy harvesters as for wind-turbines? Or is it possible to identify constructive interactions that may lead to an increase in the total harvested energy? In the swimming problem, I am interested in the impact on the energetic cost of swimming near a free or rigid surface, or in the vicinity of other individuals.

For both problems, understanding the coupling of the solid dynamics through the fluid motion will be essential. This research axis will combine experimental work on vibrating tubes (postdoctoral work of Gordon Taub to be started in Spring 2013) and theoretical/numerical analysis. In the flag problem, a generalization of Lighthill's theory to non-uniform incoming flow will be used.

– *Non-linear dynamics modeling*

In the energy harvesting flag problem, we so far focused on regions of the parameter space where the long-term flapping motion of the flag is strongly periodic. Several experimental and numerical studies have however shown that as the flow velocity is increased further, complex non-periodic or even chaotic regimes may develop (Michelin *et al.*, 2008; Abderrahmane *et al.*, 2012). Understanding these transitions and, in particular, being able to predict their occurence is essential for the robustness of the energy harvesting flag. For the flag problem, recent results suggest that such transitions may be linked to the nonlinear coupling of two or more unstable modes. During the NAGE project, I will investigate such transitions and mode-coupling effects with Christophe Eloy (IRPHE), using nonlinear simulations and weakly non-linear asymptotic analysis.

Conclusions

In the coming years, I will continue developing the two main research topics presented in this manuscript following various fundamental questions that I have detailed in the previous chapters. Among these, the role of hydrodynamic interactions in the collective dynamics of multiple swimming or energy harvesting systems will have a particularly important role, which I would like to emphasize in these concluding remarks.

In most of the problems that I have presented in this document, the dynamics of a single isolated system in an unbounded uniform flow were considered: the nutrient concentration around a single swimming cell, the solute distribution around an isolated phoretic microswimmer, the flapping dynamics and harvesting efficiency of a single energy harvesting flag or vibrating cable placed in an unbounded uniform flow... For simplicity, this approach purposely overlooked the influence of a confined environment or of neighboring systems in order to focus on the mechanisms of the single-system dynamics.

The main challenges associated with the problems presented here, are intimately linked to the dynamics of a single system (swimmer or energy harvester) *in its environment*, in particular to the presence of a boundary (rigid wall or free surface) or of other similar systems. Indeed, swimming micro-organisms are most often encountered in suspensions and stacking multiple energy harvesting devices in close proximity is a possible response to their limited individual efficiency. The ultimate goal is to gain some insight on the dynamics and efficiency of a large assembly of such individual systems (e.g. school of fish, energy harvesters farms). The formalism and tools that can be used to treat the interaction of two individuals are likely to differ fundamentally and practically from those that can realistically be implemented to study the collective dynamics of a large (and possibly dense) collection of such systems. However, the study of the two-body dynamics is an important step in order to identify fundamental interaction mechanisms on which reduced-order model can be built to describe a larger assembly.

In the isolated geometry considered in Chapter 1, the micro-swimmer or the phoretic particle has no preferential direction of motion. These dynamics will be modified passively or actively by the presence of a chemical solute gradient or of a non-uniform far-field flow, both of which are either externally-imposed or result from the presence of a second individual. Micro-organisms have the ability to respond actively or passively to a large variety of external forcing and gradients (e.g. gravity, temperature, shear, concentration of a chemical tracer). This response may profoundly alter their collective behavior when each organism is able to modify the environment of its neighbors (see for example Saintillan & Shelley, 2008; Ezhilan *et al.*, 2012). In the case of autophoretic particles, the purely passive coupling between the spontaneous motion of the particle and the chemical properties of its environment (e.g. local gradient of solute concentration, other chemically-active particles) should be characterized. This study should take three main steps: (i) the coupling of a single particle to a far-field gradient, (ii) the coupling of two particles and (iii) the collective dynamics of a suspension. Each stage will benefit from the results of the previous one in terms of modeling the interaction using a model that is physically accurate while still remaining amenable to simple numerical simulations.

Similarly, understanding the hydrodynamic interactions of multiple energy harvesters (e.g. vibrating

cylinders in cross flows, flapping piezoelectric flags) requires different stages: (i) considering the impact of a non-uniform flow on the vibration properties, (ii) explicitly studying the coupled motion of two systems and (iii) characterizing the general properties of a large assembly of harvesters. Because of the complexity of the high-Re flows around vibrating structures, using the results of stages (i) and (ii) to construct a simplified model for stage (iii) may not be the most appropriate route. A different approach to step (iii) is instead to consider directly the dynamics of a large and non regular assembly of vibrating structures to try to gain some insight on the link between the arrangements of the structures and their vibration properties. This will be the essence of the experimental work of Gordon Taub during his postdoc starting in May 2013. In parallel, a detailed and deterministic analysis of the behavior of a small number of structures (typically two) will provide some important insight on the type of couplings that may develop. Furthermore, in the case of piezoelectric flags for which the harvesting system is explicitly described, it will be possible to evaluate the impact of electrodynamic interactions when the different vibrating structures are coupled through their harvesting circuit.

Appendix A

Bibliography

Abderrahmane, H. A., Paidoussis, M. P., Fayed, M. & Ng, H. D. 2012 Nonlinear dynamics of silk and Mylar flags flapping in axial flows. *J. Wind Eng.* **107–108**, 225–236.

Akcabay, D. T. & Young, Y. L. 2012 Hydroelastic response and energy harvesting potential of flexible piezoelectric beams in viscous flow. *Phys. Fluids* **24**, 054106.

Alben, S. 2009 Simulating the dynamics of flexible bodies and vortex sheets. *J. Comp. Phys.* **228**, 2587–2603.

Alben, S. 2010 Regularizing a vortex sheet near a separation point. *J. Comp. Phys.* **229**, 5280–5298.

Alben, S. & Shelley, M. J. 2008 Flapping states of a flag in an inviscid fluid: bistability and the transition to chaos. *Phys. Rev. Lett.* **100**, 074301.

Allen, J. J. & Smits, A. J. 2001 Energy harvesting eel. *J. Fluids Struct.* **15**, 629–640.

Anderson, J. L. 1989 Colloid transport by interfacial forces. *Ann. Rev. Fluid Mech.* **21**, 61–99.

Balint, T. S. & Lucey, A. D. 2005 Instability of a cantilevered flexible plate in viscous channel flow. *J. Fluids Struct.* **20**, 893–912.

Barrero-Gil, Antonio, Pindado, Santiago & Avila, Sergio 2012 Extracting energy from vortex-induced vibrations: A parametric study. *Applied Mathematical Modelling* **36** (7), 3153 – 3160.

Batchelor, G. K. 1970 The stress system in a suspension of force-free particles. *J. Fluid Mech.* **41**, 545–570.

Bearman, P. W. 1984 Vortex shedding from oscillating bluff bodies. *Ann. Rev. Fluid Mech.* **16**, 195–222.

Benjamin, T. B. 1963 The threefold classification of unstable disturbances in flexible surfaces bounding inviscid flows. *Journal of Fluid Mechanics* **16** (3), 436–450.

Berg, H. C. 2004 *E. coli in motion*. New York: Springer.

Bernitsas, M. M., Raghavan, K., Ben-Simon, Y. & Garcia, E. M. H. 2008 VIVACE (Vortex Induced Vibration Aquatic Clean Energy: a new concept in generation of clean and renewable energy from fluid flow. *J. Offshore Mech. Arct. Eng.* **130**, 041101.

Birkhoff, G. & Zarentello, E. H. 1957 *Jets, Wakes and Cavities*. New York: Academic Press.

Bishop, R. E. D. & Hassan, A. Y. 1964 The lift and drag forces on a circular cylinder oscillating in a flowing fluid. *Proc. R. Soc. London A* **277**, 51–75.

Blake, J. R. 1971 A spherical envelope approach to ciliary propulsion. *J. Fluid Mech.* **46**, 199–208.

Blake, J. R. & Chwang, A. T. 1974 Fundamental singularities of viscous flow. Part 1. the image system in the vicinity of a stationary no-slip boundary. *J. Eng. Math.* **8**, 23–29.

Blake, J. R. & Sleigh, M. A. 1974 Mechanics of ciliary locomotion. *Biol. Rev.* **49**, 85–125.

Blevins, R. 1990 *Flow-induced vibration*, 2nd edn. New York: Van Nostrand Reinhold.

Bourguet, R., Karniadakis, G. E. & Triantafyllou, M. S. 2011 Vortex-induced vibrations of a long flexible cylinder in shear flow. *J. Fluid Mech.* **677**, 342–382.

Brady, J. F 2010 Particle motion driven by solute gradients with application to autonomous motion: continuum and colloidal perspectives. *J. Fluid Mech.* **667**, 216–259.

Brennen, C. & Winnet, H. 1977 Fluid mechanics of propulsion by cilia and flagella. *Ann. Rev. Fluid Mech.* **9**, 339–398.

Cairns, R. A. 1979 The role of negative energy waves in some instabilities of parallel flows. *Journal of Fluid Mechanics* **92**, 1–14.

Candelier, F., Boyer, F. & Leroyer, A. 2011 Three-dimensional extension of Lighthill's large-amplitude elongated-body theory of fish locomotion. *J. Fluid Mech.* **674**, 196–226.

Chwang, A.T. & Wu, T. 1975 Hydromechanics of low-Reynolds-number flow. Part 2. Singularity method for Stokes flows. *Journal of Fluid Mechanics* **67** (04), 787–815.

Connell, B. S. H. & Yue, D. K. P. 2007 Flapping dynamics of a flag in uniform stream. *J. Fluid Mech.* **581**, 33–67.

Coq, N., Bricard, A., Delapierre, F.-D., Malaquin, L., du Roure, O., Fermigier, M. & Bartolo, D. 2011 Collective beating of artificial microcilia. *Phys. Rev. Lett.* **107**, 014501.

Córdova-Figueroa, U. M. & Brady, J. F. 2008 Osmotic Propulsion: The Osmotic Motor. *Phys. Rev. Lett.* **100** (15), 158303.

Cossu, C. & Morino, L. 2000 On the instability of a spring-mounted circular cylinder in a viscous flow at low Reynolds numbers. *J. Fluids Struct.* **14**, 183–196.

Crowdy, D., Lee, S., Samson, O., Lauga, E. & Hosoi, A. E. 2011 A two-dimensional model of low-Reynolds number swimming beneath a free surface. *J. Fluid Mech.* **681**, 24–47.

Doaré, O. 2010 Dissipation effect on local and global stability of fluid-conveying pipes. *J. Sound Vib.* **329**, 72–83.

Doaré, O. & Michelin, S. 2011 Piezoelectric coupling in energy-harvesting fluttering flexible plates: linear stability analysis and conversion efficiency. *J. Fluids Struct.* **27**, 1357–1375.

Doaré, O., Sauzade, M. & Eloy, C. 2011 Flutter of an elastic plate in a channel flow: confinement and finite-size effects. *J. Fluids Struct.* **27**, 76–88.

Dreyfus, R., Baudry, J., Roper, M. L., Fermigier, M., Stone, H. A. & Bibette, J. 2005 Microscopic artificial swimmers. *Nature* **437**, 862–865.

Dunnmon, J. A., Stanton, S. C., Mann, B. P. & Dowell, E. H. 2011 Power extraction from aeroelastic limit cycle oscillations. *J. Fluids Struct.* **27**, 1182–1198.

Ebbens, S. J & Howse, J. R 2010 In pursuit of propulsion at the nanoscale. *Soft Matter* **6** (4), 726.

Eloy, C., Kofman, N. & Schouveiler, L. 2012 The origin of hysteresis in the flag instability. *J. Fluid Mech.* **691**, 583–593.

Eloy, C., Lagrange, R., Souilliez, C. & Schouveiler, L. 2008 Aeroelastic instability of a flexible plate in a uniform flow. *J. Fluid Mech.* **611**, 97–106.

Eloy, C. & Lauga, E. 2012 Kinematics of the most efficient cilium. *Phys. Rev. Lett.* **109**, 038101.

Eloy, C., Souilliez, C. & Schouveiler, L. 2007 Flutter of a rectangular plate. *J. Fluids Struct.* **23**, 904–919.

Evans, A. A., Ishikawa, T., Yamaguchi, T. & Lauga, E. 2011 Orientational order in concentrated suspensions of spherical microswimmers. *Phys. Fluids* **23**, 111702.

Ezhilan, B., Pahlavan, A. Alizadeh & Saintillan, D. 2012 Chaotic dynamics and oxygen transport in thin films of aerotactic bacteria. *Phys. Fluids* **24**, 091701.

Facchinetti, M. L., de Langre, E. & Biolley, F. 2004*a* Coupling of structure and wake oscillators in vortex-induced vibrations. *J. Fluids Struct.* **19**, 123–140.

Facchinetti, M. L., de Langre, E. & Biolley, F. 2004*b* Vortex-induced travelling waves along a cable. *Eur. J. Mech. B/Fluids* **23**, 199–208.

Gao, W., Sattayasamitsathit, S., Manesh, K. M., Weihs, D. & Wang, J. 2010 Magnetically powered flexible metal nanowire motors. *J. Am. Chem. Soc.* **132**, 14403.

Ghosh, A. & Fischer, P. 2009 Controlled propulsion of artificial magnetic nanostructured propellers. *Nano Lett.* **9**, 2243–2245.

Giacomello, A. & Porfiri, M. 2011 Underwater energy harvesting from a heavy flag hosting ionic polymer metal composites. *J. Appl. Phys.* **109**, 084903.

Golestanian, R., Liverpool, T. B. & Ajdari, A. 2005 Propulsion of a molecular machine by asymmetric distribution of reaction products. *Phys. Rev. Lett.* **94** (22), 220801.

Golestanian, R, Liverpool, T B & Ajdari, A 2007 Designing phoretic micro- and nano-swimmers. *New J. Phys.* **9**, 126.

Gray, J. & Hancock, G. J. 1955 The propulsion of sea-urchin spermatozoa. *J. Exp. Biol.* **32**, 802–814.

Grouthier, C., Michelin, S. & de Langre, E. 2012 Optimal energy harvesting by vortex-induced vibrations in cables. In *Proceedings of the 10th International Conference on Flow-Induced Vibrations (and Flow-Induced Noise) FIV 2012*. Dublin, Ireland.

Gueron, S. & Levit-Gurevich, K. 1999 Energetic considerations of ciliary beating and the advantage of metachronal coordination. *Proc. Natl. Ac. Sci.* **96**, 12240–5.

Gueron, S., Levit-Gurevich, K., Liron, N. & Blum, J. J. 1997 Cilia internal mechanism and metachronal coordination as a result of hydrodynamic coupling. *Proc. Natl. Ac. Sci* **94**, 6001–6006.

Gueron, S. & Liron, N. 1992 Ciliary motion modeling and dynamic multicilia interactions. *Biophys. J.* **63**, 1045–1058.

Gueron, S. & Liron, N. 1993 Simulations of three-dimensional ciliary beats and cilia interactions. *Biophys. J.* **65**, 499–507.

Guirao, B. & Joanny, J.-F. 2007 Spontaneous creation of macroscopic flow and metachronal waves in an array of cilia. *Biophys. J.* **92**, 1900–1917.

Guo, C. Q. & Païdoussis, M. P. 2000 Stability of rectangular plates with free side-edges in two-dimensional inviscid channel flow. *J. Appl. Mech.* **67**, 171–176.

Guyomard, D., Badel, A., Lefeuvre, E. & Richard, C. 2005 Towards energy harvesting using active materials and conversion improvement by nonlinear processing. *IEEE Trans. Ultrason. Ferroelectr. Freq. Control* **52**, 584–594.

Halbert, S. A., Tam, P. Y. & Blandau, R. J. 1976 Egg transport in the rabbit oviduct: the roles of cilia and muscle. *Science* **191**, 1052–1053.

Hancock, G. J. 1953 The self-propulsion of microscopic organisms through liquids. *Proc. R. Soc. Lond. A* **217**, 96–121.

Hartlen, R. T. & Curie, I. G. 1970 Lift-oscillator model of vortex-induced vibration. *J. Eng. Mech.* **EM5**, 577–591.

Howse, J. R., Jones, R. A. L., Ryan, A. J., Gough, T., Vafabakhsh, R. & Golestanian, R. 2007 Self-motile colloidal particles: From directed propulsion to random walk. *Phys. Rev. Lett.* **99** (4), 048102.

Huang, L. 1995 Flutter of cantilevered plates in axial flow. *J. Fluids Struct.* **9**, 127–147.

Huang, W.-X. & Sung, H. J. 2010 Three-dimensional simulation of a flapping flag in uniform flow. *J. Fluid Mech.* **653**, 301–336.

Hussong, J., Breugem, W.-P. & Westerweel, J. 2011 A continuum model for flow induced by metachronal coordination between beating cilia. *J. Fluid Mech.* **684**, 137–162.

Ishikawa, T. & Pedley, T. J. 2007 Diffusion of swimming model micro-organisms in a semi-dilute suspension. *J. Fluid Mech.* **588**, 437–462.

Ishikawa, T., Simmonds, M. P. & Pedley, T. J. 2006 Hydrodynamic interaction of two swimming model micro-organisms. *J. Fluid Mech.* **568**, 119–160.

Ishikawa, T., Simmonds, M. P. & Pedley, T. J. 2007 The rheology of a semi-dilute suspension of swimming model micro-organisms. *J. Fluid Mech.* **588**, 399–435.

Jia, L.-B., Li, F., Yin, X.-Z. & Yin, X.-Y. 2007 Coupling modes between two flapping filaments. *J. Fluid Mech.* **581**, 199–220.

Jülicher, F & Prost, J 2009 Generic theory of colloidal transport. *Eur. Phys. J. E* **29** (1), 27–36.

Kanevsky, A., Shelley, M. J. & Tornberg, A.-K. 2010 Modeling simple locomotors in Stokes flow. *J. Comp. Phys.* **229**, 958–977.

Kanso, E. & Marsden, J. E. 2005 Optimal motion of an articulated body in a perfect fluid. In *Proc. CDC*, , vol. 44, pp. 2511–2516.

Kanso, E., Marsden, J. E., Rowley, C. W. & Melli-Huber, J. 2005 Locomotion of articulated bodies in a perfect fluid. *J. Nonlin. Science* **15**, 255–289.

Kline, T. R., Paxton, W. F., Mallouk, T. E. & Sen, A. 2005 Catalytic nanomotors: Remote-controlled autonomous movement of striped metallic nanorods. *Angew. Chem. Int. Ed.* **44**, 744–746.

Kornecki, A., Dowell, E. H. & O'Brien, J. 1976 On the aeroelastic instability of two-dimensional panels in uniform incompressible flow. *J. Sound Vib.* **47**, 163–178.

de Langre, E. 2006 Frequency lock-in is caused by coupled-mode flutter. *J. Fluids Struct.* **22**, 783–791.

Lauga, E. & Powers, T. R. 2009 The hydrodynamics of swimming micro-organisms. *Rep. Prog. Phys.* **72**, 096601.

Lemaitre, C., Hémon, P. & de Langre, E. 2005 Instability of a long ribbon hanging in axial air flow. *J. Fluids Struct.* **20**, 913–925.

Lenz, P. & Ryskin, A. 2006 Collective effects in ciliary arrays. *Phys. Biol.* **3**, 285–294.

Leshansky, A. M., Kenneth, O., Gat, O. & Avron, J. E. 2007 A frictionless microswimmer. *New J. Phys.* **9**, 145.

Lighthill, M.J. 1971 Large-amplitude elongated-body theory of fish locomotion. *Proc. Roy. Soc. B* **179**, 125–138.

Lighthill, M. J. 1952 On the squirming motion of nearly spherical deformable bodies through liquids at very small Reynolds numbers. *Comm. Pure App. Math.* **5**, 109–118.

Lin, Z., Thiffeault, J.-L. & Childress, S. 2011 Stirring by squirmers. *J. Fluid Mech.* **669**, 167–177.

Magar, V., Goto, T. & Pedley, T. J. 2003 Nutrient uptake by a self-propelled steady squirmer. *Q. J. Appl. Maths* **56**, 65–91.

Magar, V. & Pedley, T. J. 2005 Average nutrient uptake by a self-propelled unsteady squirmer. *J. Fluid Mech.* **539**, 93–112.

Mathelin, L. & de Langre, E. 2005 Vortex-induced vibrations and waves under shear flow with a wake oscillator model. *Eur. J. Mech. B* **24**, 478–490.

Meliga, P. & Chomaz, J. M. 2011 An asymptotic expansion of the vortex-induced vibrations of a circular cylinder. *J. Fluid Mech.* **671**, 137–167.

Meliga, P., Chomaz, J. M. & Gallaire, F. 2011 Extracting energy from a flow: An asymptotic approach using vortex-induced vibrations and feedback control. *J. Fluids Struct.* **27**, 861–874.

Michelin, S. 2009 Falling, flapping, flying, swimming...: high-*Re* fluid-solid interactions with vortex shedding. PhD thesis, Univeristy of California, San Diego.

Michelin, S. & Doaré, O. 2012 Energy harvesting efficiency of piezoelectric flags in axial flows. *J. Fluid Mech.* **714**, 489–504.

Michelin, S. & Lauga, E. 2010*a* Efficiency optimization and symmetry-breaking in an envelope model for ciliary locomotion. *Phys. Fluids* **22**, 111901.

Michelin, S. & Lauga, E. 2010*b* The long-time dynamics of two hydrodynamically-coupled swimming cells. *Bull. Math. Biol.* **72**, 973–1005.

Michelin, S. & Lauga, E. 2011 Optimal feeding is optimal swimming for all Péclet numbers. *Phys. Fluids* **23** (10), 101901.

Michelin, S. & Lauga, E. 2013 Unsteady feeding and optimal strokes of model ciliates. *J. Fluid Mech.* **715**, 1–31.

Michelin, S., Lauga, E. & Bartolo, D. 2013 Spontaneous autophoretic motion of isotropic particles. (under review) preprint http://arxiv.org/abs/1211.6935.

Michelin, S. & Llewellyn Smith, S. G. 2009*a* Linear stability analysis of coupled parallel flexible plates in an axial flow. *J. Fluids Struct.* **25**, 1136–1157.

Michelin, S. & Llewellyn Smith, S. G. 2009*b* Resonance and propulsion performance of a heaving flexible wing. *Phys. Fluids* **21**, 071902.

Michelin, S. & Llewellyn Smith, S. G. 2009*c* An unsteady point vortex method for coupled fluid-solid problems. *Theor. Comp. Fluid Dyn.* **23**, 127–153.

Michelin, S. & Llewellyn Smith, S. G. 2010 Falling cards and flapping flags: understanding fluid-solid interactions using an unsteady point vortex model. *Theor. Comp. Fluid Dyn.* **24**, 195–200.

Michelin, S., Llewellyn Smith, S. G. & Glover, B. J. 2008 Vortex shedding model of a flapping flag. *J. Fluid Mech.* **617**, 1–10.

Newman, D. J. & Karniadakis, G. E. 1997 A direct numerical simulation study of flow past a freely vibrating cable. *J. Fluid Mech.* **344**, 95–136.

Niedermayer, T., Eckhardt, B. & Lenz, P. 2008 Synchronization, phase locking and metachronal wave formation in ciliary chains. *Chaos* **18**, 037128.

Osterman, N. & Vilfan, A. 2011 Finding the ciliary beating pattern with optimal efficiency. *Proc. Natl. Ac. Sci. USA* **108**, 15727–15732.

Paidoussis, M. P. 1998 *Fluid-Structure Interactions, Slender Structures and Axial Flows*, , vol. 1. Academic Press, London.

Paidoussis, M. P. 2004 *Fluid-Structure Interactions, Slender Structures and Axial Flows*, , vol. 2. Academic Press, London.

Paidoussis, M. P., Price, S. J. & de Langre, E. 2010 *Fluid-Structure Interactions*. Cambridge University Press.

Pak, O. S., Gao, W., Wang, J. & Lauga, E. 2011 High-speed propulsion of flexible nanowire motors: Theory and experiments. *Soft Matter* **7**, 8169–8181.

Parkinson, G. 1989 Phenomena and modeling of flow-induced vibrations of bluff bodies. *Prog. Aerospace Sci.* **26**, 169–224.

Paxton, W F, Kistler, K C, Olmeda, C C, Sen, A, Angelo, S K St, Cao, Y, Mallouk, T E, Lammert, P E & Crespi, V H 2004 Catalytic nanomotors: Autonomous movement of striped nanorods. *J. Am. Chem. Soc.* **126** (41), 13424–13431.

Pedley, T. J. & Kessler, J. O. 1992 Hydrodynamic phenomena in suspensions of swimming microorganisms. *Ann. Rev. Fluid Mech.* **24**, 313–358.

Peng, Z. & Zhu, Q. 2009 Energy harvesting through flow-induced oscillations of a foil. *Phys. Fluids* **21**, 123602.

Popescu, M. N., Dietrich, S., Tasinkevych, M. & Ralston, J. 2010 Phoretic motion of spheroidal particles due to self-generated solute gradients. *Eur. Phys. J. E* **31**, 351–367.

Pozrikidis, C. 1997 *Introduction to Theoretical and Computational Fluid Dynamics*. Oxford: Oxford Univ. Press.

Purcell, E. M. 1977 Life at low-Reynolds number. *Am. J. Phys.* **45**, 3–11.

Ristroph, L. & Zhang, J. 2008 Anomalous hydrodynamic drafting of interacting flapping flags. *Phys. Rev. Lett.* **101**, 194502.

Ruckenstein, E. 1981 Can phoretic motions be treated as interfacial tension gradient driven phenomena? *J. Colloid Interface Sci.* **83**, 77–81.

Sabass, B. & Seifert, U. 2012*a* Dynamics and efficiency of a self-propelled, diffusiophoretic swimmer. *J. Chem. Phys.* **136**, 064508.

Sabass, B. & Seifert, U. 2012*b* Nonlinear, electrocatalytic swimming in the presence of salt. *J. Chem. Phys.* **136** (21), 214507.

Saintillan, D. & Shelley, M. J. 2008 Instabilities and pattern formation in active particle suspensions: kinetic theory and continuum simulations. *Phys. Rev. Lett.* **100**, 178103.

Schouveiler, L. & Eloy, C. 2009 Coupled flutter of parallel plates. *Phys. Fluids* **21**, 081703.

Sharifi-Mood, N., Koplik, J. & Maldarelli, C. 2013 Diffusiophoretic self-propulsion of colloids driven by a surface reaction: the sub-micron particle regime for exponential and van der Waals interactions. *Phys. Fluids* **25**, 012001.

Shelley, M., Vandenberghe, N. & Zhang, J. 2005 Heavy flags undergo spontaneous oscillations in flowing water. *Phys. Rev. Lett.* **94**, 094302.

Shelley, M. J. & Zhang, J. 2011 Flapping and bending bodies interacting with fluid flows. *Ann. Rev. Fluid Mech.* **43**, 449–465.

Singh, K., Michelin, S. & de Langre, E. 2012*a* The effect of non-uniform damping on flutter in axial flow and energy harvesting strategies. *Proc. R. Soc. A* **468**, 3620–3635.

Singh, K., Michelin, S. & de Langre, E. 2012*b* Energy harvesting from axial fluid-elastic instabilities of a cylinder. *J. Fluids Struct.* **30**, 159–172.

Sleigh, M. A., Blake, J. R. & Liron, N. 1988 The propulsion of mucus by cilia. *Am. Rev. Resp. Dis.* **137**, 726–741.

Spagnolie, S. E. & Lauga, E. 2010*a* Jet propulsion without inertia. *Phys. Fluids* **22**, 081902.

Spagnolie, S. E. & Lauga, E. 2010*b* The optimal elastic flagellum. *Phys. Fluids* **22**, 031901.

Spagnolie, S. E. & Lauga, E. 2012 Hydrodynamics of self-propulsion near a boundary: predictions and accuracy of far-field approximations. *J. Fluid Mech.* **700**, 105–147.

Stone, H. A. & Samuel, A. D. T. 1996 Propulsion of microorganisms by surface distorsions. *Phys. Rev. Lett.* **77**, 4102.

Tam, D. & Hosoi, A. E. 2007 Optimal stroke patterns for purcell's three-link swimmer. *Phys. Rev. Lett.* **98** (6), 068105.

Tam, D. & Hosoi, A. E. 2011*a* Optimal feeding and swimming gaits of biflagellated organisms. *Proceedings of the National Academy of Sciences* **108** (3), 1001.

Tam, D. & Hosoi, A. E. 2011*b* Optimal kinematics and morphologies for spermatozoa. *Phys. Rev. E* **83**, 045303.

Tang, L. & Païdoussis, M. P. 2009 The coupled dynamics of two cantilevered flexible plates in axial flow. *J. Sound Vib.* **323**, 214–231.

Taylor, G.I. 1952 Analysis of the swimming of long and narrow animals. *Proc. Roy. Soc Lon. A* **214**, 158–183.

Techet, A. H., Allen, J. J. & Smits, A. J. 2002 Piezoelectric eels for energy harvesting in the ocean. In *Proceedings of the Twelfth International Offshore and Polar Engineering Conference*, pp. 713–718. Kitakyushu, Japan.

Thutupalli, S., Seemann, R. & Herminghaus, S. 2011 Swarming behavior of simple model squirmers. *New J. Phys.* **13**, 073021.

Tian, F.-B., Luo, H., Zhu, L., Liao, J. & Lu, X.-Y. 2011 An efficient immersed boundary-lattice boltzmann method for the hydrodynamic interactions of elastic filaments. *J. Comp. Phys.* **230**, 7266–7283.

Tierno, P., Guell, O., Sagues, F., Golestanian, R. & Pagonabarraga, I. 2010 Controlled propulsion in viscous fluids of magnetically actuated colloidal doublets. *Phys. Rev. E* **81**, 011402.

Vilfan, A. 2012 Optimal shapes of surface slip driven self-propelled microswimmers. *Phys. Rev. Lett.* **109**, 128105.

Vilfan, A. & Julicher, F. 2006 Hydrodynamic flow patterns and synchronization of beating cilia. *Phys. Rev. Lett.* **96**, 058102.

Violette, R., de Langre, E. & Sydlowski, J. 2007 Computation of vortex-induced vibrations of long structures using a wake oscillator model: Comparison with DNS and experiments. *Comp. Struct.* **85**, 1134–1141.

Violette, R., de Langre, E. & Sydlowski, J. 2010 A linear approach to vortex-induced vibrations and waves. *J. Fluids Struct.* **26**, 442–466.

Watanabe, Y., Isogai, K., Suzuki, S. & Sugihara, M. 2002*a* A theoretical study of paper flutter. *J. Fluids Struct.* **16**, 543–560.

Watanabe, Y., Suzuki, S., Sugihara, M. & Sueoka, Y. 2002*b* An experimental study of paper flutter. *J. Fluids Struct.* **16**, 529–542.

Westwood, A. 2004 Ocean power wave and tidal energy review. *Refocus* **5**, 50–55.

Williamson, C. H. K. & Brown, G. L. 1998 A series in $1/\mathrm{Re}^{1/2}$ to represent the Strouhal-Reynolds relationship of the cylinder wake. *J. Fluids Struct.* **12**, 1073–1085.

Williamson, C. H. K. & Govardhan, R. 2004 Vortex-induced vibrations. *Ann. Rev. Fluid Mech.* **36**, 413–455.

Williamson, C. H. K. & Roshko, A. 1988 Vortex formation in the wake of an oscillating cylinder. *J. Fluids Struct.* **2**, 355–381.

Yoshinaga, N., Nagai, K. H., Sumino, Y. & Kitahata, H. 2012 Drift instability in the motion of a fluid droplet with a chemically reactive surface driven by marangoni flow. *Phys. Rev. E* **86**, 016108.

Yoshitake, Y., Sueoka, A., Yamasaki, M., Sugimura, Y. & Ohishi, T. 2004 Quenching of vortex-induced vibrations of towering structure and generation of electricity using hula-hoops. *Journal of Sound and Vibration* **272** (1–2), 21 – 38.

Zhang, J., Childress, S., Libchaber, A. & Shelley, M. 2000 Flexible filaments in a flowing soap film as a model for one-dimensional flags in a two-dimensional wind. *Nature* **408**, 835–839.

Zhao, G. & Pumera, M. 2012 Macroscopic self-propelled objects. *Chem. Asian J.* **7** (9), 1994–2002.

Zhu, L. 2007 Viscous flow past a flexible fibre tethered at its center point: vortex shedding. *J. Fluid Mech.* **587**, 217–234.

Zhu, L. & Peskin, C. 2002 Simulation of flapping flexible filament in a flowing soap film by the immersed boundary method. *J. Comput. Phys.* **179**, 452–468.

Zhu, L. & Peskin, C. 2003 Interaction of two flapping filaments in a flowing soap film. *Phys. Fluids* **15**, 1954–1960.

Zhu, Q. 2012 Energy harvesting by a purely passive flapping foil in shear flows. *J. Fluids Struct.* **34**, 157–169.

Zhu, Q. & Peng, Z. 2009 Mode coupling and flow energy harvesting by a flapping foil. *Phys. Fluids* **21**, 033601.

Sébastien Michelin

Assistant Professor
Ingénieur en Chef des Mines

LadHyX – Ecole polytechnique
91128 Palaiseau, France
☎ (+33) 1 69 33 52 73
sebastien.michelin@ladhyx.polytechnique.fr
http://www.off-ladhyx.polytechnique.fr/people/michelin/

Research interests and projects

- High-Re fluid-solid interactions, stability analysis and nonlinear dynamics.
- Energy harvesting from fluid-solid instabilities.
- Biological locomotion.
- Optimization problems in fluid-solid interactions.
- Low-Re swimming and hydrodynamical interactions between swimming micro-organisms.
- Advection-diffusion in low-Re flows.
- Complex analysis, conformal mapping and potential flows.
- Vortex dynamics and stability analysis.

Education

2009 **PhD in Aerospace Engineering**, *University of California, San Diego*, La Jolla, CA, USA, *Falling, flapping, flying, swimming... : high-Re fluid-solid interactions with vortex shedding* PhD advisor : Pr. Stefan G. Llewellyn Smith.

2007 **M.S. in Aerospace Engineering**, *University of California, San Diego*, La Jolla, CA, USA.

2005 **Ingénieur du Corps des Mines**, *Ecole des Mines de Paris*, Paris, France.

2002 **Diplôme d'Ingénieur**, *Ecole polytechnique*, Palaiseau, France.

Academic Employment

2010–present **Assistant Professor**, *LadHyX, Département de Mécanique – Ecole polytechnique*, Palaiseau, France.

2009 **Post-doctoral Researcher**, *Mechanical and Aerospace Engineering – University of California, San Diego*, La Jolla, CA, USA.

2005–2009 **Graduate Student Researcher**, *Mechanical and Aerospace Engineering – University of California, San Diego*, La Jolla, CA, USA.

2003–2004 **Visiting Scientist**, *Scripps Institution of Oceanography*, La Jolla, CA, USA.

2002 **Research Intern**, *Département d'Aérodynamique Fondamentale et Expérimentale – ONERA*, Meudon, France.

Teaching Experience

2013–present **MEC432 – Fluid Mechanics**, *Petites Classes*, Ecole polytechnique, France.

2011–present **MEC581 – Projects in Mechanics**, Ecole polytechnique, France.

2010–present **MEC431 – Continuum Mechanics I**, *Petites Classes*, Ecole polytechnique, France.

2011–2012 **MEC561 – Fluid-Structure Interactions**, *Petites Classes*, Ecole polytechnique, France.

2012 **MS206 – Fluid-Structure Interactions**, *Petites Classes, substitution*, ENSTA ParisTech, France.

2009 **MAE107 – Computational Methods in Engineering**, *Instructor*, UCSD, CA, USA.

2006 **MAE210A – Graduate Level Fluid Mechanics**, *Teaching Assistant*, UCSD, CA, USA.

Grants

2011–2014 **Marie-Curie International Reintegration Grant**, *PI : S. Michelin*, 75,000€.

2012–2013 **LASIPS Grant**, *PI : O. Doaré*, 57,000€.

2013–2016 **ANR Young Investigator Grant (ANR JCJC)**, *PI : S. Michelin*, 228,000€.

Awards and Honors

2009 Summer Graduate Student Teaching Fellowship

2009 MAE Dissertation Fellowship
2008 MAE Outstanding Graduate Student Award
2005–2007 Jacobs School of Engineering Graduate Fellowship
2002–2005 Corps des Mines Fellowship
2002 Prix L. E. Rivot – French Academy of Sciences

Refereed Publications

19. **S. Michelin**, E. Lauga and D. Bartolo, 2013 : Spontaneous autophoretic motion of isotropic particles (under review)
18. X. Amandolese, **S. Michelin** and M. Choquel, 2013 : Low speed flutter and limit-cycle oscillations of a two-degree-of-freedom flat plate in a wind tunnel (under review)
17. C. Grouthier, **S. Michelin**, Y. Modarres-Sadeghi and E. de Langre : Self-similar vortex-induced vibrations of a hanging string, *J. Fluid Mech.*, (in press)
16. **S. Michelin** and E. Lauga, 2013 : Unsteady feeding and optimal strokes of model ciliates, *J. Fluid Mech.*, **715**, 1–31
15. **S. Michelin** and O. Doaré, 2013 : Energy harvesting efficiency of piezoelectric flags in axial flows, *J. Fluid Mech.*, **714**, 489–504
14. K. Singh, **S. Michelin** and E. de Langre, 2012 : Effect of damping on flutter in axial flow and energy-harvesting strategies, *Proc. Roy. Soc. A*, **468**, 3620–3635
13. K. Singh, **S. Michelin** and E. de Langre, 2012 : Energy harvesting from fluid-elastic instabilities of a cylinder, *J. Fluids Struct.*, **30**, 159–172
12. **S. Michelin** and E. Lauga, 2011 : Optimal feeding is optimal swimming for all Péclet numbers, *Phys. Fluids*, **23** (10), 101901
11. D. Lopez, **S. Michelin** and E. de Langre, 2011 : Flow-induced pruning of branched systems and brittle reconfiguration, *J. Theor. Biol.*, **284**, 117–124
10. O. Doaré and **S. Michelin**, 2011 : Piezoelectric energy harvesting from flutter instability : local/global linear stability and efficiency, *J. Fluids Struct.*, **27**, 1357–1375
9. **S. Michelin** and E. Lauga, 2010 : Efficiency optimization and symmetry-breaking in a model of ciliary locomotion, *Phys. Fluids*, **22** (11), 111901
8. **S. Michelin** and E. Lauga, 2010 : The long-time dynamics of two-hydrodynamically coupled swimming cells, *Bull. Math. Biol.*, **72**, 973–1005
7. **S. Michelin** and S. G. Llewellyn Smith, 2010 : Falling cards and flapping flags : understanding fluid-solid interactions using an unsteady point vortex model, *Theor. Comp. Fluid Dyn.*, **24**, 195–200
6. **S. Michelin** and S. G. Llewellyn Smith, 2009 : Linear stability analysis of coupled parallel flexible plates in an axial flow, *J. Fluids Struct.*, **25**, 1136–1157
5. **S. Michelin** and S. G. Llewellyn Smith, 2009 : Resonance and propulsion performance of a heaving flexible wing, *Phys. Fluids*, **21** (7), 071902
4. **S. Michelin** and S. G. Llewellyn Smith, 2009 : An unsteady point vortex method for coupled fluid-solid problems, *Theor. Comp. Fluid Dyn.*, **23**, 127–153
3. **S. Michelin**, S. G. Llewellyn Smith and B. J. Glover, 2008 : Vortex shedding model of a flapping flag, *J. Fluid Mech.*, **617**, 1–10
2. S. G. Llewellyn Smith, **S. Michelin** and D. G. Crowdy, 2008 : The dipolar field of rotating bodies in two dimensions *J. Fluid Mech.*, **607**, 109–118
1. D. Sipp, D. Fabre, **S. Michelin** and L. Jacquin, 2005 : Stability of a vortex with a heavy core, *J. Fluid Mech.*, **526**, 67–76

Conference proceedings

– K. Singh, **S. Michelin** and E. de Langre : Energy harvesting from axial flow-induced instabilities in slender structures. *Proceedings of the 10th International Conference on Flow-Induced Vibrations (and Flow-Induced Noise) – FIV 2012*, Dublin, Ireland, July 2012
– C. Grouthier, **S. Michelin** and E. de Langre : Optimal energy harvesting by Vortex-Induced Vibrations in Cables. *Proceedings of the 10th International Conference on Flow-Induced Vibrations (and Flow-Induced Noise) – FIV 2012*, Dublin, Ireland, July 2012

– **S. Michelin** and O. Doaré : Flow energy harvesting from piezoelectric flags. *Proceedings of the 10th International Conference on Flow-Induced Vibrations (and Flow-Induced Noise) – FIV 2012*, Dublin, Ireland, July 2012
– X. Amandolèse, **S. Michelin** and M. Choquel : Low-speed flutter and limit-cycle oscillations of a flat plate section in a wind tunnel. *Proceedings of the 10th International Conference on Flow-Induced Vibrations (and Flow-Induced Noise) – FIV 2012*, Dublin, Ireland, July 2012
– **S. Michelin**, K. Singh and E. de Langre : Flow energy harvesting by fluttering slender bodies in axial currents. *Proceedings of the ASME 2011 30th International Conference on Ocean, Offshore and Arctic Engineering OMAE2011*, Rotterdam, The Netherlands, June 2011

Other conference presentations

– **S. Michelin**, D. Bartolo & E. Lauga : Advective effects on the propulsion of phoretic micro-swimmers. *65th Annual Meeting of the American Physical Society – Division of Fluid Dynamics*, San Diego, CA, November 2012
– **S. Michelin**, K. Singh and E. de Langre : Energy harvesting using flapping flags in axial flows. *Fluid & Elasticity 2012*, La Jolla, CA, November 2012
– **S. Michelin** and E. Lauga : Swimming and feeding : optimal strokes of model ciliates. *Biological Flow : A Conference to Celebrate the 70th birtday of T. J. Pedley*, Cambridge, UK, April 2012
– **S. Michelin** and E. Lauga : Optimal feeding vs. optimal swimming of model ciliates. *64th Annual Meeting of the American Physical Society – Division of Fluid Dynamics*, Baltimore, MD, November 2011
– **S. Michelin** and E. Lauga : Optimal swimming of model ciliates. *63rd Annual Meeting of the American Physical Society – Division of Fluid Dynamics*, Long Beach, CA, November 2010
– **S. Michelin** and E. Lauga : Propulsion ciliée à bas Reynolds : Efficacité, optimisation et brisure de symétrie. *Self-propelled motions in fluids : Modeling, Analysis and Control*, Nancy, France, October 2010
– **S. Michelin** and E. Lauga : Efficiency optimization and symmetry-breaking in an envelope model of ciliary locomotion. *Individual and Collective Fluid Mechanics of Swimming Microorganisms*, Glasgow, Scotland, July 2010
– **S. Michelin** and S.G. Llewellyn Smith : Thrust production and vortex wake generated by flapping flexible wings. *BBVIV 6*, Capri, Italy, June 2010
– **S. Michelin** and S.G. Llewellyn Smith : Flapping of flexible sheets in high-Re flows and applications to locomotion. *Fluid & Elasticity 2009*, Carry-le-Rouet, France, June 2009.
– **S. Michelin** and S.G. Llewellyn Smith : Propulsive performance of a heaving flexible membrane. 3^{rd} *Southern California Symposium on Flow Physics*, La Jolla, CA, April 2009.
– **S. Michelin** and S.G. Llewellyn Smith : A vortex shedding model of a flapping membrane. *61st Annual Meeting of the American Physical Society – Division of Fluid Dynamics*, San Antonio, TX, November 2008.
– **S. Michelin** and S.G. Llewellyn Smith : Falling, flapping, flying, swimming,... : understanding fluid-solid interactions using an unsteady point vortex model. *IUTAM Symposium : 150 years of vortex dynamics*, Copenhagen, Denmark, October 2008
– **S. Michelin** and S.G. Llewellyn Smith : High-Re flows past flexible flapping profiles. 2^{nd} *Southern California Symposium on Flow Physics*, Santa Monica, CA, April 2008.
– **S. Michelin** and S.G. Llewellyn Smith : Flying, swimming, falling,... : fluid-solid interactions with vortex shedding. *60th Annual Meeting of the American Physical Society – Division of Fluid Dynamics*, Salt Lake City, UT, November 2007.
– **S. Michelin** and S.G. Llewellyn Smith : Application of point vortices model to Maxwell's problem. *Third European SCAT Workshop and Summerschool, "Vortices and Vortex Sheets : theorics, numerics and applications"*., Porquerolles, France, June 2007.
– **S. Michelin** and S.G. Llewellyn Smith : Application of a vortex shedding model to Maxwell's problem. *Southern California Symposium on Flow Physics*, Pasadena, CA, April 2007.
– **S. Michelin**, and S.G. Llewellyn Smith : Vortex Shedding and Maxwell's problem. *59th Annual Meeting of the American Physical Society – Division of Fluid Dynamics*, Tampa, FL, November 2006.

Seminars

2013 PCT Gulliver, ESPCI, Paris, France
2012 Institut Jean le Rond d'Alembert, UPMC, Paris, France
FLOW Center, KTH, Stockholm, Sweden
2011 PMMH, ESPCI, Paris, France
2010 LIMSI, Orsay, France

2008 LadHyX, Ecole polytechnique, Palaiseau, France
IMFT, Toulouse, France
IRPHE, Marseille, France
PMMH, ESPCI, Paris, France

2007 DAFE, ONERA, Meudon, France
Scripps Institution of Oceanography, La Jolla, CA, USA

2005 DAFE, ONERA Meudon, France

2004 Scripps Institution of Oceanography, La Jolla, CA, USA

Students and postdocs

Postdocs

Kiran Singh	Postdoc, LadHyX (2010–2012)
Gordon Taub	Postdoc, LadHyX (2013–2014)

PhD students

Diego Lopez	co-advised with E. de Langre, LadHyX (2009–2012) Title : *Modeling reconfiguration strategies in plants submitted to flow*
Clément Grouthier	co-advised with E. de Langre, LadHyX (2010–present)
Yifan Xia	LadHyX (2012–present)

Masters students

Witold Krasny	EPFL, LadHyX (2011–2012)
Yifan Xia	Ecole Centrale de Lyon, LadHyX (2012)

Undergraduate interns/projects

Maxime Choquel	co-advised with X. Amandolèse, LadHyX (2010–2011)
Pierre Pinta	co-advised with C. Baroud, LadHyX (2010–2011)
Juan Ruiz Ruiz	co-advised with C. Clanet, LadHyX (2012–2013)

Service

Administration

Deputy director of LadHyX (2013 – present)

Reviewer

Journal of Fluid Mechanics, Journal of Fluids and Structures, Physics of Fluids, Theoretical and Computational Fluid Dynamics, Engineering Structures, Experimental Mechanics, International Journal of Non-Linear Mechanics, Journal of the Royal Society – Interface, Archive of Applied Mechanics, Applied Mathematical Modelling, Proceedings of the Royal Society A, Transport in Porous Media.

Israel Science Foundation, Agence Nationale pour la Recherche, Fonds de la Recherche Scientifique – FNRS

Memberships

American Physical Society